

# On the small-scale dynamics of cloud edges

Von der Fakultät für Physik und Geowissenschaften  
der Universität Leipzig  
genehmigte

## DISSERTATION

zur Erlangung des akademischen Grades

Doctor rerum naturalium

(Dr. rer. nat.)

vorgelegt

von Diplom-Meteorologin Jeannine Ditas (geb. Katzwinkel)  
geboren am 29. August 1984 in Eisenhüttenstadt

Gutachter: Prof. Dr. Andreas Macke  
Prof. Dr. Siegfried Raasch

Tag der Verleihung 19. Mai 2014



*“There is still an incomplete physical understanding of many components of the climate system and their role in climate change. Key uncertainties include aspects of the roles played by clouds,...” (IPCC Report 2007)*





## **Bibliographische Beschreibung**

Katzwinkel, Jeannine

On the small-scale dynamics of cloud edges

Universität Leipzig, Dissertation

117 S.\*, 90 Lit.\*, 29 Abb., 2 Tab., Anlagen

### **Referat:**

Eine der größten Unsicherheiten in der Bestimmung des Klimawandels stellen Wolken dar. In ihnen finden zahlreiche Prozesse von Wolken- bis mm-Skala statt und interagieren untereinander sowie mit atmosphärischen Prozessen. Diese Komplexität und die benötigte hohe räumliche Auflösung zur Erforschung kleinskaliger Prozesse sind nur zwei Herausforderungen in der Wolkenforschung. Ein bislang unzureichend erforschter Prozess am Wolkenrand ist das Einmischen. Dieser beschreibt den turbulenten Transport von ungesättigter Umgebungsluft in die Wolke. Anschließendes Mischen führt zur Verdunstung von Tropfen und zu negativem Auftrieb am Wolkenrand. Man unterscheidet zwei Arten des Einmischens: Einmischen an der Wolkenoberkante und seitliches Einmischen. Ersteres ist vor allem an der Oberkante von stratiformen Wolken zu finden, wobei seitliches Einmischen vor allem bei Cumuluswolken eine Rolle spielt.

Diese Arbeit untersucht mit Hilfe von hochaufgelösten Messungen (cm-Skala) beide Arten des Einmischprozesses. Gemessen wurde mit der Hubschrauber Messplattform ACTOS (Airborne Cloud Turbulence Observation System). An der Oberkante einer Stratocumuluschicht führt scherungsinduziertes Einmischen zu einer turbulenten Inversionsschicht (TIL). Diese besteht aus wolkenfreier Luft und scheint aufgrund der Turbulenz mit der darunter liegenden Wolkenschicht gekoppelt zu sein. Je dicker die TIL ist, desto stärker wird die Turbulenz gedämpft. Auf diese Weise ist die TIL auf eine maximale Dicke beschränkt und direktes Mischen zwischen Wolkenoberkante und freier Atmosphäre wird gehemmt. Am Rand von flachen Cumuluswolken wird die "subsiding shell" durch scherungsbedingtes seitliches Einmischen initiiert. Ihre Entwicklung konnte anhand von detaillierten Messungen in kontinuierlich wachsenden Passatwindwolken untersucht werden. Das Wachstum der "subsiding" shell auf Kosten des Wolkenkerns und die gleichzeitige Zunahme der Abwindgeschwindigkeit in der Region stimmt quantitativ mit der Simulation einer idealisierten "subsiding shell" überein.

Diese einzigartigen Messungen an Wolkenrändern stellen einen bemerkenswerten Fortschritt in der Wolkenforschung dar, der die zukünftige Forschung beeinflussen wird.

---

\* 117 S. (Seitenzahl insgesamt)

90 Lit. (Anzahl der im Literaturverzeichnis ausgewiesenen Literaturangaben)



## **Bibliographic Description**

Katzwinkel, Jeannine

On the small-scale dynamics of cloud edges

University of Leipzig, Dissertation

117 pp.\*, 90 Ref.\*, 29 Fig., 2 Tab., Appendix

### **Abstract:**

Clouds are one of the major uncertainties in climate change predictions caused by their complex structure and dynamics. Numerous cloud processes are acting from cloud-scale down to mm-scale and interplay with each other as well as with atmospheric processes. This complexity on the one hand and the high spatial resolution required to analyse the small scale processes on the other hand cause difficulties in cloud research. One important and until now insufficiently understood process in cloud microphysics is the entrainment process. It defines the turbulent transport of sub-saturated environmental air into the cloud region. Subsequent mixing leads to the evaporation of cloud droplets resulting in negatively buoyant air at cloud edge. One distinguishes between two types of entrainment processes: cloud top and lateral entrainment. While the first type is mostly detected at the top of stratiform clouds, lateral entrainment plays an important role for the dynamics of cumulus clouds.

Within in this thesis, highly-resolved measurements with a resolution down to the centimeter scale performed with the helicopter-borne measurement payload ACTOS (Airborne Cloud Turbulence Observation System) are used to study both types of entrainment processes. Shear-induced cloud top entrainment leads to a turbulent inversion layer (TIL) atop of a stratocumulus layer consisting of clear air. The TIL seems to be coupled with the underlying cloud layer due to the turbulence intensity. With increasing thickness of the TIL the turbulence inside is damped monotonically leading to a maximum layer thickness and inhibiting direct mixing between cloud top and free troposphere. At the edges of shallow trade wind cumuli, shear-induced lateral entrainment generates a subsiding shell. Its evolution is analysed based on detailed measurements in continuously developing shallow cumuli. With the cloud evolution, the subsiding shell grows at the expense of the cloud core region and an increasing downdraft velocity is observed within this region. These observations are confirmed with the simulation of an idealised subsiding shell.

The results present unique observations at the edges of clouds and are an appreciable progress in cloud research which decisively influence future research.

---

\* 117 pp. (Number of pages)

90 Ref. (Number of references)



# Contents

<b>1</b>	<b>Introduction</b>	<b>3</b>
1.1	Clouds . . . . .	3
1.1.1	Stratocumulus . . . . .	5
1.1.2	Cumulus . . . . .	7
1.2	Motivation of this work . . . . .	8
<b>2</b>	<b>Turbulence and entrainment</b>	<b>11</b>
2.1	Turbulence . . . . .	11
2.1.1	Turbulent scales and the energy cascade . . . . .	12
2.1.2	Local isotropy . . . . .	15
2.1.3	Taylor hypothesis . . . . .	15
2.1.4	Energy dissipation rate . . . . .	16
2.1.5	Buoyancy . . . . .	17
2.1.6	Turbulent kinetic energy . . . . .	18
2.1.7	Gradient Richardson number . . . . .	20
2.1.8	Ozmidov and Corrsin scale . . . . .	21
2.2	Entrainment . . . . .	22
2.2.1	Cloud-top entrainment . . . . .	23
2.2.2	Lateral entrainment . . . . .	25
<b>3</b>	<b>Airborne Cloud Turbulence Observation System</b>	<b>29</b>
3.1	General overview . . . . .	29
3.2	Instrumentation . . . . .	31
3.2.1	Wind velocity measurements . . . . .	33
3.2.2	Temperature, humidity, and pressure measurements . . . . .	33
3.2.3	Aerosol and cloud droplet measurements . . . . .	34
3.2.4	Navigation . . . . .	35
3.3	Data post-processing . . . . .	36
3.3.1	Wind vector transformation . . . . .	36

3.3.2	Calibration of hot-wire data . . . . .	37
<b>4</b>	<b>Turbulent inversion layer above a marine stratocumulus cloud</b>	<b>39</b>
4.1	Campaign and Meteorology . . . . .	39
4.2	Weather conditions . . . . .	40
4.3	Results . . . . .	42
4.4	Conclusion . . . . .	46
<b>5</b>	<b>Subsiding shells at the edges of trade wind cumuli</b>	<b>55</b>
5.1	Campaign and Meteorology . . . . .	55
5.2	Weather conditions . . . . .	57
5.3	Results . . . . .	59
5.3.1	Concepts and statistical cloud analysis . . . . .	59
5.3.2	Characterisation of cloud edge . . . . .	64
5.3.3	Comparison with model results . . . . .	68
5.4	Summary and Discussion . . . . .	71
<b>6</b>	<b>Summary</b>	<b>75</b>
	<b>List of abbreviations</b>	<b>i</b>
	<b>List of Figures</b>	<b>i</b>
	<b>List of Tables</b>	<b>vii</b>
	<b>Bibliography</b>	<b>ix</b>

## Wolkenbildung

### *Stratus*

Wenn von dem stillen Wasserspiegel-Plan  
Ein Nebel hebt den flachen Teppich an,  
Der Mond, dem Wallen des Erscheins vereint,  
Als ein Gespenst Gespenster bildend scheint,  
Dann sind wir alle, das gestehn wir nur,  
Erquickt', erfreute Kinder, o Natur!  
Dann hebt sich wohl am Berge, sammelnd breit,  
An Streife Streifen, so umdüsterts weit  
Die Mittelhöhe, beidem gleich geneigt,  
Obs fallend wässert oder luftig steigt.

### *Cumulus*

Und wenn darauf zu höherer Atmosphäre  
Der tüchtige Gehalt berufen wäre,  
Steht Wolke hoch, zum herrlichsten geballt,  
Verkündet, festgebildet, Machtgewalt,  
Und, was ihr fürchtet und auch wohl erlebt,  
Wie's oben drohet, so es unten bebt.

### *Cirrus*

Doch immer höher steigt der edle Drang!  
Erlösung ist ein himmlisch leichter Zwang.  
Ein Aufgehäuftes, flockig löst sich auf,  
Wie Schäflein trippelnd, leicht gekämmt zuhauf.  
So fließt zuletzt, was unten leicht entstand,  
Dem Vater oben still in Schoß und Hand.

### *Nimbus*

Nun laßt auch niederwärts, durch Erdgewalt  
Herabgezogen, was sich hoch geballt,  
In Donnerwettern wütend sich ergehn,  
Heerscharen gleich entrollen und verwehn! -  
Der Erde tätig leidendes Geschick!  
Doch mit dem Bilde hebet euren Blick.-  
Die Rede geht herab, denn sie beschreibt;  
Der Geist will aufwärts, wo er ewig bleibt.





# 1 Introduction

## 1.1 Clouds

Goethe's poem from 1821 is only one example of painters and poets' fascination with clouds. Indeed, clouds have been the inspiration for numerous works of art and are simultaneously elements of intensive research activities. In his poem, Goethe poetically describes four cloud types, which were first defined within the scientific cloud classification by Howard (1803). Howard's classification scheme is still applied in modern meteorology, even though it was already written at a time when scientists assumed that clouds consist of bubbles. This assumption was present until Assmann performed comprehensive microscopical studies of cloud droplets in 1884. Clouds were only observed at ground level for a long time, until Jacques Alexandre César Charles (1746–1823) conducted the first instrumented manned balloon flight measuring temperature and pressure of the atmosphere in 1783. However, in-situ cloud measurements were not performed until 1903, when Wigand realised the first comprehensive study of the in-cloud shape of ice crystals and graupel particles using an instrumented manned balloon. Hence, cloud research is a relative young science, which has experienced an abrupt and accelerated increase since 1940 caused by necessary funding, personnel support, and particularly technological development, e.g. computers, radars and satellites becoming available for scientists.

However, clouds were still indicated in the Intergovernmental Panel on Climate Change Report 2007 (IPCC Report) as “a major source of uncertainty in the simulations of climate changes” (Solomon et al., 2007). This great uncertainty is due to the complexity of processes acting within clouds on the one hand, and the interaction of these cloud processes among themselves and with atmospheric processes over a wide range of spatial and temporal scales on the other. The atmospheric motion (macroscale motion, e.g., fronts, pressure systems, atmospheric stability down to microscale motion, e.g., droplet collision, entrainment) influences the structure and dynamics of cloud patterns which range in size from hundreds of kilometers for

large synoptic-scale cloud patterns down to  $< 1$  kilometer for individual clouds. But clouds also influence the atmospheric motion. They are responsible for up to 30% of the Earth's albedo (Solomon et al., 2007). Moreover, deep-convective clouds influence the general circulation (e.g., Hadley –, monsoon circulation). Hence, clouds play an important role in the radiation and energy balance of the atmosphere and are most relevant for climate. But the changing conditions within the atmosphere caused by the anthropogenic climate change also affects the clouds. Presently, no explicit statement can be given on how clouds react on the increase of anthropogenic aerosol emission and atmospheric temperature and how the cloud feedbacks influence the climate in response (Heintzenberg and Charlson, 2009). Therefore, the detailed understanding of the complex cloud processes in particular in terms of a climate change is a very important task in research activities.

On global average, clouds produce a net cooling affect on the climate (Heintzenberg and Charlson, 2009). But the impact on the atmospheric radiative budget depends strongly on the cloud type. General circulation models (GCM) indicate that low-level marine clouds provide the greatest contribution to the spread in climate sensitivity. An increase of 15 – 20% in the amount of low-level clouds is presumed to counteract a doubling of  $\text{CO}_2$  (Slingo, 1990). Thereby, the predominant cloud types in the marine boundary layer are stratocumulus and shallow trade wind cumulus. The first type features a large fractional overage and a strong negative net cloud radiative forcing, while shallow cumuli have a small cloud fraction and a weak negative net cloud radiative forcing, but they occur over a much larger area of the ocean (Heintzenberg and Charlson, 2009). Both cloud types are characterised by a weak dynamical forcing, which is the reason why small changes in boundary layer properties and dynamical forcing have strong influence on their cloud cover. These slight changes in cloud cover and also in cloud height and cloud emissivity can exert a stronger influence on the Earth's radiative budget than equivalent changes in greenhouse gases (Heintzenberg and Charlson, 2009). Therefore, the understanding of the impact of boundary layer clouds on climate depends on the detailed understanding of the cloud processes acting from cloud-scale down to mm-scale.

The most important small-scale process at cloud edge is the transport of warm, sub-saturated environmental air into the cloud region, called “entrainment process”. Subsequent mixing with cloudy air influences the cloud structure and dynamics. The analysis of both processes is challenging because the most aircraft observations are performed with a true airspeed of about  $100 \text{ m s}^{-1}$  which enables only a spatial resolution down to the meter scale. One possibility to analyse the small-scale processes is the slow-moving platform “ACTOS” developed at the Leibniz Institute for

Tropospheric Research (Siebert et al., 2006a). The helicopter-borne measurement platform operates with a low true airspeed of  $20 \text{ m s}^{-1}$  and combined with a high sampling frequency, measurements with a spatial resolution down to the centimeter scale are enabled. Within this thesis, these highly-resolved measurements are used to study the impact of both types of entrainment processes, cloud-top and lateral entrainment, on the small-scale structure of clouds. Both types are dominant in different cloud types. While cloud-top entrainment mainly influences the structure of stratocumulus clouds, lateral entrainment is mostly present at the edges of cumulus clouds. The appearance and characteristics of both cloud types are briefly introduced in the following Sections.

### 1.1.1 Stratocumulus

#### General aspects

In the international cloud atlas of the World Meteorological Organisation (WMO) a stratocumulus cloud is described as a “grey or whitish, or both grey and whitish, patch, sheet or layer of cloud which almost always has dark parts, composed of tessellations, rounded masses, rolls, etc., which are non-fibrous (except for virga) and which may or may not be merged; most of the regularly arranged small elements have an apparent width of more than five degrees” (World Meteorological Organization, 1975). Such cloud decks can be found over large areas of the world and especially over the colder oceans where they can cover thousands of square kilometers. In the annual mean, stratocumulus clouds cover 23% of the Earth’s surface (Wood, 2012). Some regions are frequently covered by this cloud type (e.g., coast of California and Mexico, coast of Peru and Chile, coast of north- and southwestern Africa), whereas the occurrence at other regions depends on seasonal characteristics. This temporary occurrence is caused by the fact that the formation and maintenance of stratocumulus clouds depend on two conditions: i) a stable stratification in the free troposphere which suppresses deep convection and leads to the formation of a shallow layered cloud topped by a strong inversion and ii) a continuing moisture supply from the surface to counteract diluting processes (Driedonks and Duynkerke, 1989).

Stratocumulus clouds, which are mostly located at top of the well-mixed boundary layer, have a large impact on the Earth’s albedo. The reflection of the incoming solar radiation is increased by 40 – 60% compared to the cloudless case. This large impact is not compensated in any significant way by the divergences of the longwave

radiative fluxes due to a stratocumulus cloud deck which leads consequently to a large net radiative cooling of such clouds. These influences on the Earth's radiative energy budget also lead to an impact on the turbulent structure of the boundary layer. Additionally, the impact of stratocumulus cloud decks on heat and moisture influences local weather conditions (Driedonks and Duynkerke, 1989). Hence, stratocumulus cloud decks play an important role in the atmospheric energy budget and on climate. Therefore, a realistic reproduction of the extensive stratocumulus decks in models is very crucial for the understanding of its impact on climate and climate change.

### Physical processes

This section will take a closer look at individual processes acting within and at the edges of a stratocumulus cloud. A schematic picture of this layer topping a well-mixed boundary layer is presented in Fig. 1.1, whereby the grey region marks the stratocumulus cloud deck.

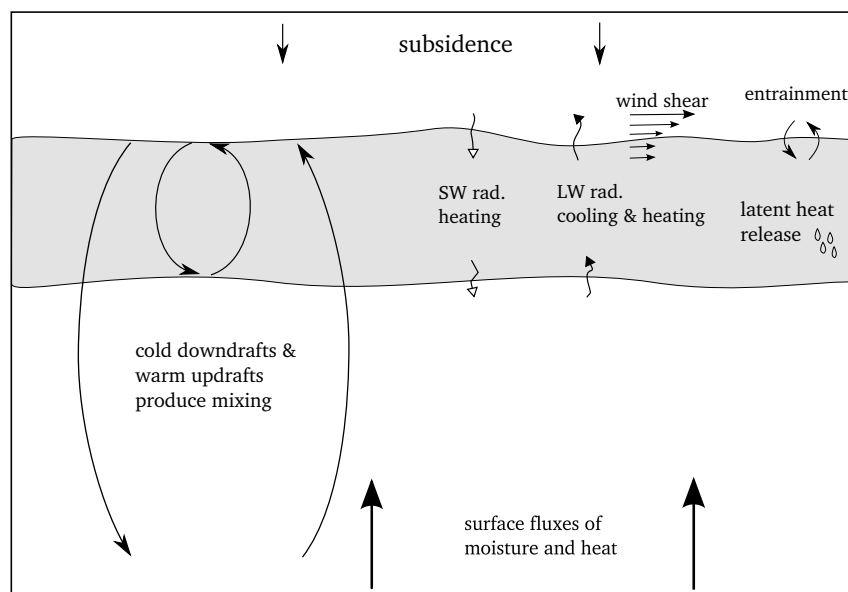


Figure 1.1: Overview of physical processes occurring within and at the edge of a stratocumulus cloud. Thereby, *SW* and *LW* denote the short- and longwave radiation fluxes.

The structure and dynamics of a stratocumulus layer is strongly influenced by the surface fluxes of moisture and heat. Droplet formation by condensation leads to the release of latent heat which is a source for buoyancy production and turbulence. If

the buoyancy of the resulting rising air parcels is large enough, they overshoot the inversion layer and initiate cloud-top entrainment. So, potentially warm, dry, and sub-saturated free-tropospheric air is transported into the cloud layer from above (Bennetts et al., 1986; Driedonks and Duynkerke, 1989). A detailed introduction of cloud-top entrainment is given in Section 2.2.1. Further mechanisms which could initiate cloud-top entrainment are radiative cooling at cloud top on the one hand, initiated by the larger upward-directed outgoing longwave radiation flux compared to the downward flux. On the other hand, the absorption of 15% of the solar incoming radiation leads to a warming extending deep into the cloud layer (Bennetts et al., 1986; Driedonks and Duynkerke, 1989). Both processes can produce convective turbulence (denoted by the whirls of arrows in Fig. 1.1) and could cause a destabilisation of the cloud and the whole boundary layer. Additionally, the combination of both processes can decouple the cloud layer from the underlying boundary layer and cut off the cloud deck from the surface flux which would lead to the dissolution of the cloud deck (Driedonks and Duynkerke, 1989). Furthermore, large-scale subsidence could also lead to the dissolution process of the cloud deck through advection of the inversion layer. The structure, especially of the cloud top, can be further influenced by wind shear. The latter acts as a further mechanical source for turbulence but its precise role for cloud-top entrainment process is discussed controversially (Wang et al., 2012).

## 1.1.2 Cumulus

### General aspects

Cumulus clouds are described in the International cloud atlas of the WMO as “detached clouds, generally dense and with sharp outlines, developing vertically in the form of rising mounds, domes or towers, of which the bulging upper part often resembles a cauliflower. The sunlit parts of these clouds are mostly brilliant white; their base is relatively dark and nearly horizontal. Sometimes Cumulus is ragged” (World Meteorological Organization, 1975). The vertical extension of these clouds can be very different. Shallow cumuli have mostly a cloud top height lower than 2 km while the top of cumulus clouds with a large vertical extent can reach a top-height of 10 km. Just as the vertical extent the cloud lifetime covers a huge range from minutes to several hours. But all cumulus clouds are characterised by a relatively small horizontal diameter compared to their respective vertical extent, i.e.,  $< 2$  km

for shallow cumuli to  $\approx 5$  km for the largest ones. This causes the weaker net cloud radiative forcing compared to a stratocumulus layer. Koren et al. (2008) pointed out that these clouds with an area smaller than  $1 \text{ km}^2$  cause the largest contribution to the total cloud reflectance. Combined with the large amount of cumulus clouds over wide areas of the planet, an explanation is given for the large feedback of cumulus clouds on climate.

The dynamics of cumulus clouds are very complex and until now not completely understood in detail. Dynamical processes over the full range of the turbulent energy cascade influence the cloud evolution and its lifetime, and can lead to the formation of heavy rainfalls within less than one hour, as for instance in the trade wind region (Langmuir, 1948). Furthermore, cumulus clouds have an impact on the vertical transport of heat, moisture, aerosol, and momentum, and on the radiative transfer between the well-mixed boundary layer and the free troposphere (Siebesma et al., 2003). Hence, cumulus clouds play an important role for the moisture and energy balance within the troposphere.

## Physical processes

Cumulus clouds develop due to the achievement of the lifting condensation level of a rising thermal. At this level, the water vapour within an air parcel starts to condensate which leads to further positive buoyancy due to the release of latent heat. The positive buoyancy of the air parcel can be enhanced at the level of free convection. Possible mechanisms limiting the cloud growth are on the one hand an inversion layer, where the surrounding air is much warmer suppressing a further ascent, or mixing processes, which lead to a dilution of the cloud top on the other hand. A sketch of a cumulus cloud is given in Fig. 1.2.

A cumulus cloud is characterised by a strong updraft which can be found in the cloud core. These updrafts are compensated by downdrafts in the near environment of the cloud. The resulting horizontal wind shear at cloud edge leads to lateral entrainment which influences the dynamics and evolution of cumulus clouds. A detailed introduction of lateral entrainment is given in Section 2.2.2. At cloud top, further processes are the solar radiative heating and longwave radiative cooling, although the impact of these two processes is much smaller than in the case of stratocumulus clouds. Nevertheless, both processes could initiate cloud-top entrainment which influences primary the structure and dynamics of the cloud top region.

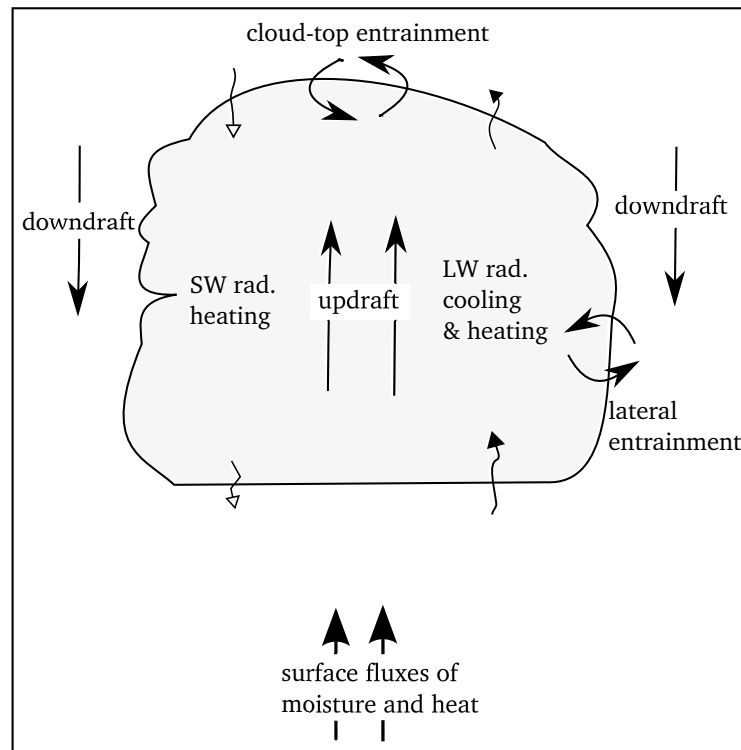


Figure 1.2: Overview of physical processes occurring within and at the edge of a cumulus cloud.

## 1.2 Motivation of this work

This thesis deals with the investigation of the impact of entrainment on the structure and dynamics of clouds. The entrainment process belongs to the processes in cloud research which are assumed to play an important role for cloud dynamics but their analysis is not straightforward. Although, within the last decades the measurement technique was enhanced in terms of instrumentation (e.g., increased sampling frequency), data analysis, and measurement possibilities (aircraft, remote sensing, satellite), there are still a lot of open questions concerning cloud physics, especially cloud microphysics, e.g.,:

- How do turbulent processes such as entrainment and subsequent mixing influence the evolution of clouds?
- How does vertical wind shear above a stratocumulus layer influence the structure and dynamics of the underlying cloud?
- Which processes cause the ability of warm cumulus clouds to develop rain

within less than thirty minutes after their formation?

These questions define the scope of this thesis. Based on measurements with a spatial resolution down to cm-scale the turbulent structure at top of a stratocumulus cloud deck and at the edges of shallow cumuli will be analysed. Therefore, measurements were performed within two different measurement campaigns. The first one was performed in the north of Germany over the Baltic Sea in 2007 and addressed the impact of shear-induced cloud-top entrainment on the dynamics of a stratocumulus cloud. The second campaign was conducted in the trade wind region near Barbados in November 2010 and April 2011 performing measurements at the edges of shallow trade wind cumuli to analyse lateral entrainment.

This thesis is structured as follows: Chapter 2 presents a general introduction to turbulent motion and entrainment while Chapter 3 introduces the measurement payload ACTOS, presents the measurement technique of individual instruments, and describes the data post-processing. The following two Chapters deal with the two measurement campaigns including a brief introduction of the campaign followed by the data analysis and results. Thereby, Chapter 4 is addressed to cloud-top entrainment at top of a stratocumulus, while Chapter 5 presents the analysis concerning lateral entrainment at the edges of shallow cumuli. The thesis finishes with a summary of the results.



## 2 Turbulence and entrainment

Turbulence is a common feature within the majority of flows observed in the atmosphere. Pictures as wads of smoke of a chimney, swirls in a river or the diffusion of coffee and milk within a Latte Macchiato are well-known. The development of turbulence in a flow is triggered by small instabilities producing turbulent kinetic energy. Turbulence enables fast mixing between different air masses in the atmosphere and the transport of heat, moisture, and momentum in the boundary layer. Hence, turbulence plays a major role in many atmospheric processes but the details of turbulence on different processes are often not fully understood yet. One example is the impact of turbulent mixing at cloud edge on cloud dynamics and structure. Within the following Chapter, basic aspects of turbulence are presented. Afterwards, the turbulent entrainment process at cloud edges is introduced.\*

### 2.1 Turbulence

A picture of a turbulent flow behind two identical cylinders is shown in Fig. 2.1 which demonstrates the complex and randomness structure of a turbulent flow. In general, the structure of such flows depends on the flow pattern as well as initial and boundary conditions. In contrast, the structure of a laminar flow is characterised by a mean velocity without fluctuations and no change in time. The character of a flow is defined by the Reynolds number  $Re$ . This non-dimensional number was introduced by Osborne Reynolds in 1883 (Reynolds, 1883) and represents the relation between inertial and viscous forces. The calculation is based on the mean velocity of the flow  $\bar{U}$ , the typical flow dimension  $\mathcal{L}$  and the kinematic viscosity of the fluid  $\nu$ :  $Re = \frac{\bar{U}\mathcal{L}}{\nu}$ . The Reynolds number of a laminar flow is characterised by comparably low values indicating high viscous forces. For example, within the Reynold's pipe-

---

\*Please note that some parts of the following Chapter are taken from Katzwinkel et al. (2012) and Katzwinkel et al. (2013) without further notice.

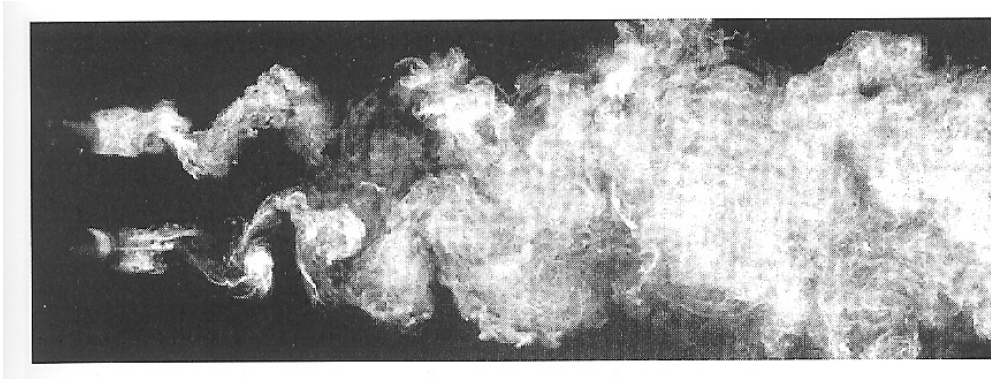


Figure 2.1: Example of a turbulent flow behind two identical cylinders. The picture is taken from Frisch and Kolmogorov (1995).

flow experiment the flow is laminar for  $Re < 2300$  while the flow is turbulent for  $Re > 4000$  (Pope, 2000). The Reynolds numbers in between characterise the gradual transition from a laminar to a turbulent flow. It is assumed that this transition is triggered by small instabilities producing the turbulent kinetic energy (Tennekes and Lumley, 1972; Davidson, 2004). The development and maintenance of turbulence depends on the receipt of energy from the mean flow due to its dissipating character. Without obtaining energy from the mean flow turbulence decays rapidly due to viscosity,  $Re$  decreases and the flow is getting laminar. Within the atmosphere, there are two main sources of energy: shear in the flow and buoyancy, whereby the latter can be influenced by radiative or evaporative cooling and solar heating. For a more-detailed description of the individual sources of energy the reader is referred to section 2.2.

### 2.1.1 Turbulent scales and the energy cascade

The previous section dealt with the appearance and development of turbulent flows while the following Chapter will give a closer look on the structure of a turbulent flow. In general, a turbulent flow can be described by eddies of different sizes. A precise definition of an eddy is not straightforward but Pope (2000) described an eddy as “a turbulent motion which is localised within a region of size  $l$ , that is moderately coherent over this region”. The largest eddy size  $l_0$  in a turbulent flow is comparable to the typical flow dimension  $\mathcal{L}$  and these eddies have a characteristic velocity  $u_0 \equiv u(l_0)$ , a timescale  $\tau(l_0) \equiv l_0/u_0$  and a Reynolds number  $Re \equiv u_0 l_0/\nu$ . Vortex stretching (lengthening of eddies) causes the unstable structure of the largest

eddies which leads to a break-up process whereby the large eddies break into smaller ones. Thereby, the energy which they received from the mean flow is transported to the yet smaller eddy sizes. The break-up process continues up to a sufficiently small Reynolds number  $Re(l) = u(l)l/\nu$  where the eddy motion is stable and the kinematic energy of the eddies dissipates by molecular viscosity. The rate of energy which is first transported constantly to yet smaller eddies and dissipates at the smallest scales can be estimated with  $\varepsilon \sim \frac{\sigma_w^3}{l_0}$ , where  $\sigma_w$  denotes the standard deviation of the vertical wind velocity. The smallest eddy scales are defined by Kolmogorov and its length scale  $\eta$ , velocity  $v_\eta$  and timescale  $\tau_\eta$  are calculated as follows (Kolmogorov, 1941):

$$\eta = (\nu^3/\varepsilon)^{1/4}, \quad v_\eta = (\nu\varepsilon)^{1/4}, \quad \tau_\eta = (\nu/\varepsilon)^{1/2}. \quad (2.1)$$

The energy dissipation rate  $\varepsilon$  is determined by the transfer of energy during the first break-up process (Pope, 2000). The whole break-up process and the transport of energy to successively smaller and smaller eddies is called the energy cascade (Pope, 2000; Frisch and Kolmogorov, 1995). Figure 2.2 shows a schematic picture of the energy cascade including the separation into the three ranges (after Frisch and Kolmogorov, 1995). The first part is the energy-containing range, where the largest eddy sizes obtain their energy from the mean flow. Within this range the eddies are anisotropic and unaffected by molecular viscosity. The next part is the inertial range, where the energy is transported from one eddy size to the yet smaller one. In this subrange, the eddies are isotropic and molecular viscosity plays a minor role. The last part is the dissipation range, where the eddy motion is stable and molecular viscosity leads to the dissipation of the eddies. These subranges are separated theoretically at different length scales (Pope, 2000). The energy-containing range and the inertial range are separated by a length scale approximately  $l_{EI} \approx 1/6l_0$  and the inertial range and dissipation range are separated by a length scale approximately  $l_{DI} = 60\nu$ . With increasing  $Re$  the difference between largest and smallest eddy scales widens leading to a larger inertial range (Tennekes and Lumley, 1972).

The distribution of the turbulent kinetic energy  $E$  among the different eddy sizes is given for homogeneous turbulence by the energy spectrum function. The bulk of energy is located within the larger scales which transport the most part of heat and momentum (Tennekes and Lumley, 1972). Within the inertial range, the amount of

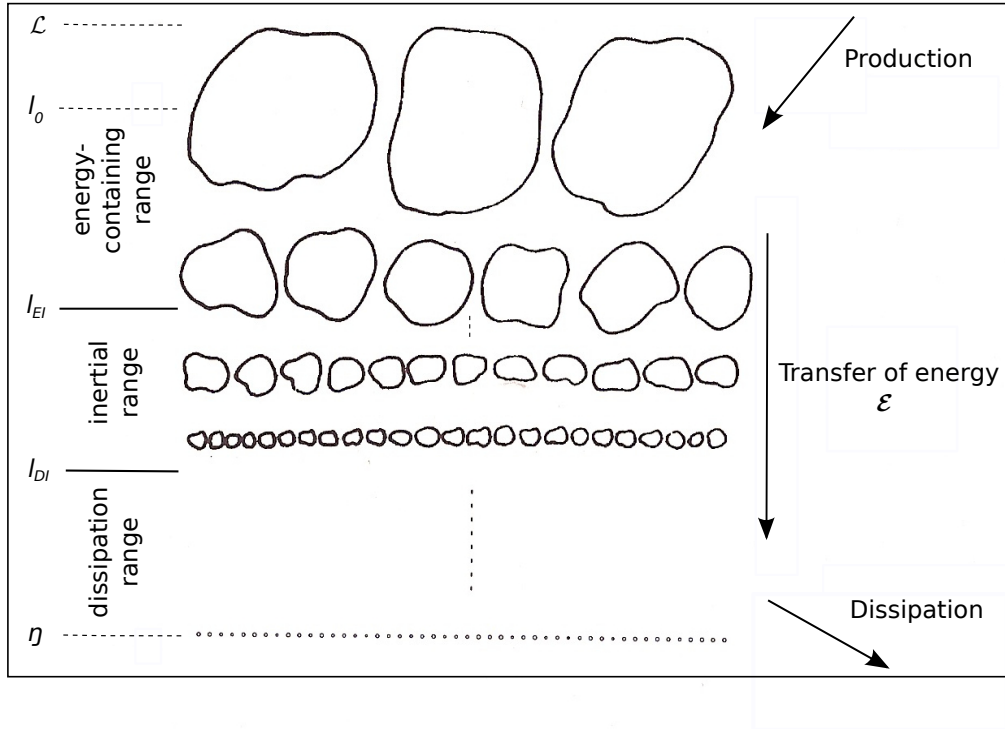


Figure 2.2: Energy cascade with the largest and smallest scales of eddies  $l_o$  and  $\eta$  modified picture based on Frisch, 1995

energy decreases with decreasing eddy size constantly concerning the Kolmogorov  $-5/3$  spectrum. This behaviour results from the second similarity hypothesis of Kolmogorov that describes the universal form of the statistics of the eddy motions only determined by  $\varepsilon$  within this range. Hence, the energy spectrum function can be given in the form:  $E(\kappa) = C \varepsilon^{2/3} \kappa^{-5/3}$  (where  $\kappa$  denotes the wave length and  $C$  is a universal constant) (Pope, 2000). Within the dissipation range, the bulk of dissipation is located. Hence, the balance of turbulent kinetic energy is given by production and dissipation.

Atmospheric stratification can damp turbulence due to shear or buoyancy, respectively. Both processes lead to the deformation and distortion of eddies which consume kinetic energy from the turbulent flow and lead to damping of turbulence. The smallest eddy scales which are affected by shear or respective buoyancy can be estimated based on the Corrsin and Ozmidov scale (Smyth and Moum, 2000). In general, the damping effect of turbulence by stratification can be quantified with help of the Richardson number  $Ri$ . It is defined by the relation of energy production compared to the loss of energy due to stratification. Within the energy balance equation, this lost of turbulent kinetic energy is considered with the buoyancy term (Brucker and Sarkar, 2007). The following sections will give brief introductions of

assumptions in turbulence theory and turbulent parameters.

## 2.1.2 Local isotropy

A basic requirement for the turbulence theory of Kolmogorov is the assumption of the local isotropic structure of a turbulent flow within the inertial range. Isotropy means independence of statistical properties on rotation, translation, and reflection of the coordinate axes (Wyngaard, 2010). An isotropic flow is characterised by a ratio of 4/3 concerning the lateral and longitudinal components of the one-dimensional kinetic energy spectrum. This ratio results from the calculation of the velocity correlation tensor of two points separated by the distance  $\mathbf{r}$ . Using the tensor one can calculate a relation between lateral and longitudinal velocity correlation functions. Combined with the fact that the energy spectrum function  $E$  is twice the Fourier transform of the velocity correlation, it results in a relation between lateral and longitudinal components of  $E$ :  $E_{33}(\kappa_1) = E_{22}(\kappa_1) = \frac{1}{2}(E_{11}(\kappa_1) - \kappa_1 \frac{dE_{11}(\kappa_1)}{d\kappa_1})$ , where  $i = j = 3$  and  $i = j = 2$  denote the lateral components,  $i = j = 1$  denotes the longitudinal component and  $\kappa_1$  denotes the longitudinal component of the wavenumber vector. Finally, using the kinetic energy spectrum function within the inertial subrange:  $E(\kappa) = C \varepsilon^{2/3} \kappa^{-5/3}$  yields  $\frac{E_{33}}{E_{11}} = \frac{E_{22}}{E_{11}} = \frac{4}{3}$ . A detailed derivation can be found in the textbooks of Batchelor (1953); Pope (2000); Wyngaard (2010).

Within this work, the local isotropy of a velocity field is analysed with  $\sigma_w^2/\sigma_u^2$ , where  $w$  denotes the vertical wind velocity and  $u$  the longitudinal component of the horizontal wind velocity. If the variances are considered as local parameter, where they do not represent the entire layer and contributions from larger structures are filtered out, then the variance equals the integrated energy spectrum function and the 4/3 ratio is also valid for the variances.

## 2.1.3 Taylor hypothesis

In turbulence theory most theoretical derivations (e.g., local isotropy) are based on the assumption of a spatial separation between two points of distance  $\mathbf{r}$ . But, measurements in the atmosphere are usually performed using an ultra sonic or a hot-wire anemometer, which measure the velocity at one point at different time. The time-series measurements can be transformed into a spatial-distance relation-

ship using Taylor's hypothesis of frozen turbulence (Biltoft, 2001). This hypothesis assumes that in the case of approximately stationary and homogeneous turbulence with a low intensity, the turbulent field is advected with the mean flow and does not change over the measurement time scale. Hence, Taylor pointed out that if the turbulent fluctuations  $u'$  are small compared to the mean flow velocity  $\bar{U}$ ,  $\frac{u'}{\bar{U}} \ll 1$ , then  $x = \bar{U}t$  where  $x$  denotes the space and  $t$  the time coordinate (Garratt, 1994).

### 2.1.4 Energy dissipation rate

The energy dissipation rate  $\varepsilon$  denotes the amount of energy which is transported between the different eddy scales, and it represents a measure of turbulence intensity. Within this work, the calculation is based on two different methods: i) direct method and ii) the second-order structure function. The first method is based on the direct definition of  $\varepsilon$  (Onley et al., 1996):

$$\bar{\varepsilon} \equiv \nu \overline{\left(\frac{\partial u_i}{\partial x_j}\right)^2}. \quad (2.2)$$

With the assumption of local isotropy only one velocity gradient can be considered, and based on the validity of Taylor's hypothesis the spatial gradient can be changed in temporal increments of the wind velocity  $\partial_t U$ . Hence, the calculation of  $\varepsilon$  is given by:

$$\bar{\varepsilon}_\tau \equiv \frac{15\nu}{\bar{U}_\tau} \overline{(\partial_t U)^2}_\tau, \quad (2.3)$$

where  $U$  denote the horizontal wind velocity and  $\bar{\cdot}_\tau$  denotes the average of the respective parameter over the integration time  $\tau$ . This direct method requires a spatial resolution on the order of 10 times the Kolmogorov length scale ( $\sim 1$  cm) which is a challenge for atmospheric observations.

The second method is based on the use of the second-order structure function  $S^{(2)}(t')$  which is calculated based on the difference in velocity between two points  $\mathbf{x} + r$  and  $\mathbf{x}$ . The spatial differences are transformed into temporal differences by assuming the Taylor hypothesis, leading to the second-order structure function as follows:

$$S^{(2)}(t') \equiv \overline{(u(t) - u(t + t'))^2}_\tau \simeq 2\bar{\varepsilon}_\tau^{2/3} (t'\bar{u}_\tau)^{2/3}, \quad (2.4)$$

where  $t'$  represents the time lag and  $u$  denotes the longitudinal component of the wind velocity. Re-arranging of eq. 2.4 leads to the calculation of  $\varepsilon$  as follows:

$$\bar{\varepsilon}_\tau \simeq \frac{(0.5 \overline{(S^{(2)}(t'))}_\tau)^{3/2}}{(t' \bar{u}_\tau)}. \quad (2.5)$$

Further information are described in Siebert et al. (2006b) and references therein.

## 2.1.5 Buoyancy

Buoyancy  $B$  describes the impulse of an air parcel to move up or down according to the density difference between the air parcel and its environment:

$$B = -g \frac{\rho - \rho_0}{\rho_0}, \quad (2.6)$$

where  $\rho$  denotes the density of the air parcel and  $\rho_0$  denotes the environmental density.

Within the atmosphere, the density can hardly be measured. Therefore, the density difference can be transformed into a temperature difference using the logarithmic derivation of the state equation  $p = \rho R_l T$ :  $\frac{\Delta p}{p} \approx \frac{\Delta \rho}{\rho} + \frac{\Delta T}{T}$ . Thereby, it is assumed that  $\frac{\Delta p}{p_0} \ll \frac{\Delta \rho}{\rho_0}$  and  $\frac{\Delta T}{T_0} \approx \frac{\Delta \Theta}{\Theta_0}$ , where  $\Theta$  denotes the potential temperature. The latter defines the temperature of an air parcel which is transported dry-adiabatically to a reference level  $p_0$ , mostly used 1000 hPa. The calculation is given by:

$$\Theta = (T + 273.15) \left( \frac{p_0}{p} \right)^{\frac{R_l}{c_p}}, \quad (2.7)$$

where  $T$  denotes the temperature,  $R_l$  marks the gas constant of air, and  $c_p$  denotes the specific heat capacity at a constant air pressure.

The calculation of the buoyancy is based on the virtual potential temperature of a moist air parcel which is the theoretical potential temperature of a dry air parcel with the same density as the moist air parcel at same pressure. Its calculation is based on the liquid water and water vapour mixing ratios:

$$\Theta_v = \Theta(1 + 0.61q_v - q_l) \quad (2.8)$$

where the water vapour mixing ratio  $q_v = \frac{0.622e}{(p-e)}$ , where  $p$  denotes the atmospheric pressure and  $e$  the water vapour partial pressure calculated with the Magnus approximation (Lawrence, 2005), and the liquid water mixing ratio  $q_l = \frac{LWC}{\rho}$ , where  $LWC$  denotes the liquid water content and  $\rho$  the density of air. Under cloudy conditions, the virtual potential temperature is not a conserved variable due to its dependence on  $q_l$ .

Hence, the calculation of  $B$  changes to (Heus and Jonker, 2008; Etling, 2008):

$$B = g \frac{\Theta_v - \bar{\Theta}_{v_0}}{\bar{\Theta}_{v_0}}, \quad (2.9)$$

whereby the bar denotes the mean value of the respective parameter.

### 2.1.6 Turbulent kinetic energy

The evolution of small-scale turbulence with time can be calculated using the balance equation for turbulent kinetic energy (e.g., Brucker and Sarkar, 2007; Etling, 2008). It is composed of the production term  $P$ , buoyancy term  $B$ , transport term  $\frac{\partial T_i}{\partial x_i}$  (where  $T$  is the identifier for “transport” of turbulent kinetic energy) and dissipation term  $\varepsilon$ :

$$\frac{dE}{dt} = P + B - \frac{\partial T_i}{\partial x_i} - \varepsilon. \quad (2.10)$$

The production of turbulent kinetic energy results from the deformation of the mean velocity flow due to, e.g., shear. This is given by:

$$P \equiv -\langle u'_i u'_j \rangle \frac{\partial u_i}{\partial x_j}, \quad (2.11)$$



where  $\langle u'_i u'_j \rangle$  describes the turbulent momentum flux which can be approximated using the gradient of  $u_i$  and the turbulent diffusion coefficient for momentum  $K_m$ :  $\langle u'_i u'_j \rangle = -K_m \frac{\partial u_i}{\partial x_j}$  (Etling, 2008). Considering only the vertical transport of momentum ( $\frac{\partial u}{\partial z}$ ) and approximating this gradient further by differences  $\Delta U$  and  $\Delta z$ , the calculation of the production term is given by:

$$P = K_m \left( \frac{\Delta U}{\Delta z} \right)^2. \quad (2.12)$$

Within the further analysis, the mean observed turbulent diffusion coefficient of  $K_m = 0.2 \text{ m}^2 \text{ s}^{-1}$  is used.

The buoyancy term describes the amount of energy originating from the vertical transport of temperature fluctuations within the atmosphere. It can either enhance the turbulent kinetic energy or damp it. The calculation bases on the turbulent heat flux  $\langle w' \Theta' \rangle$ :

$$B = \frac{g}{\Theta} \langle w' \Theta' \rangle \quad (2.13)$$

and its impact depends on the leading sign. To explain the impact of the buoyancy term on the energy budget in detail, first the flux is approximated using the gradient and the turbulent diffusion coefficient for heat  $K_h$  ( $\langle w' \Theta' \rangle = -K_h \frac{\partial \bar{\Theta}}{\partial z}$ ). Thereby,  $K_h$  can be replaced by the Prandtl number  $Pr$  multiplied by  $K_m$  leading to the calculation of the Buoyancy term as follows:

$$B = -K_m Pr \frac{g}{\Theta} \frac{\partial \bar{\Theta}}{\partial z}, \quad (2.14)$$

The impact of the buoyancy term on the energy budget is given by  $\frac{\partial \Theta}{\partial z}$ . In the case of  $\frac{\partial \Theta}{\partial z} < 0$ , the stratification is unstable (light warm air is located below the heavy cold air) which leads to an enhancement of turbulence. Otherwise for  $\frac{\partial \Theta}{\partial z} > 0$  the potentially warmer air is located above the heavy cold air (stable stratification)

leading to a decrease of the turbulent kinetic energy due to the loss of energy by vertical motion of the air parcels (Etling, 2008).

For the consideration of vertical mixing effects the use of conserved variables for moist adiabatic processes is useful. Such a conserved variable is the liquid-water potential temperature  $\Theta_l$ . It describes the potential temperature of an air parcel within which all liquid water is evaporated. The calculation is as follows (Betts, 1973):

$$\Theta_l = \Theta - (q_l L_v \Theta) / (c_p T) \quad (2.15)$$

where  $L_v$  denotes the latent heat of vaporisation. Combined with the approximation of gradients by differences ( $\Delta\Theta_l$  and  $\Delta z$ ), the final equation for the buoyancy term is given by:

$$B = -K_m Pr \frac{g}{\Theta_l} \frac{\Delta\Theta_l}{\Delta z}, \quad (2.16)$$

whereby the Prandtl number is assumed with the typical value  $Pr \approx 1$ .

The dissipation term of Eq. 2.10 consumes turbulent kinetic energy leading to a decay of turbulence.

Within this work, the calculation of the transport term is neglected, mainly because we are unable to make any reliable estimate of its contribution.

Finally, the balance equation of the turbulent kinetic energy used within this work is given by:

$$\frac{dE}{dt} = K_m \left[ \left( \frac{\Delta U}{\Delta z} \right)^2 - Pr \frac{g}{\Theta_l} \frac{\Delta\Theta_l}{\Delta z} \right] - \varepsilon. \quad (2.17)$$

### 2.1.7 Gradient Richardson number

Within the atmosphere, the development or evolution of turbulent kinetic energy depends on the amount of energy production/reduction due to buoyancy relative to the energy production due to shear. This relation is given by the buoyancy term and

the production term of the balance equation and is called flux Richardson number  $Ri$  named after the physicist and mathematician L.F. Richardson:

$$Ri = \frac{g}{\Theta} \frac{\langle w'\Theta' \rangle}{\langle w'u' \rangle \frac{\partial u}{\partial z}}. \quad (2.18)$$

Here, the fluxes are also approximated using the gradients which lead to the gradient Richardson number. A further approximation of the gradients by differences leads to the calculation of  $Ri$  in the following way:

$$Ri = \frac{g}{\Theta_l} \frac{\frac{d\Theta_l}{dz}}{\left(\frac{dU}{dz}\right)^2}. \quad (2.19)$$

The evolution of the turbulent flow depends on the specific values  $Ri$ . In the case of  $Ri > 1$ , more energy is lost by buoyancy than produced by shear. Consequently, the turbulence within the flow is strongly damped. If  $Ri = 1$ , the intensity of turbulence stays constant because the same amount of energy is produced by shear as lost by buoyancy. Turbulence would increase in the case of  $Ri < 1$ , because the production of energy due to shear is larger than the loss of energy by buoyancy. An endless increase is prevented by the energy dissipation, hence turbulence is referred to be fully developed within this range. Thereby, for  $Ri < 0.25$  the flow is fully turbulent while in the range of  $0.25 < Ri < 1$  the turbulence becomes more and more intermittent. In the case of  $Ri < 0$ , turbulence is enhanced due to both terms caused by the positive impact of the buoyancy term on the energy budget (Kondo et al., 1978; Etling, 2008).

### 2.1.8 Ozmidov and Corrsin scale

For theoretical calculations the structure of an eddy is assumed to have a spherical structure. So, the diameter of the largest eddies is defined by the parameter  $l_0$ . But the spherical structure of eddies can be influenced by atmospheric processes as shear and buoyancy which lead to deformation and distortion. If this is the case, the eddies definitely have a “squashed” velocity structure, i.e., the velocity variance is significantly reduced in the vertical dimension compared to horizontal dimensions. Such processes would lead to a loss of turbulent kinetic energy and cause a damping of turbulence. The degree of damping of turbulence depends on the scales of eddies

which are influenced by shear and buoyancy. An estimation for the smallest scale which is affected is given by the Ozmidov and Corrsin scales.

The Ozmidov scale  $l_o$  represents the scale above which buoyancy strongly influences the energetics. The calculation is based on the energy dissipation rate and the ambient buoyancy frequency  $N_f$  ( $N_f = \sqrt{\frac{g}{\Theta} \frac{\partial \Theta}{\partial z}}$ , also known as Brunt-Vaisala frequency):  $l_o = \sqrt{\frac{\varepsilon}{N_f^3}}$  (Smyth and Moum, 2000).

The Corrsin scale  $l_c$  represents the scale above which shear acts to distort eddies. Its calculation is based on the energy dissipation rate and the background shear  $S$  ( $S = \frac{du}{dz}$  at top of a stratocumulus or  $S = \frac{dw}{dx}$  at the edge of shallow cumuli, respectively):  $l_c = \sqrt{\frac{\varepsilon}{S^3}}$  (Smyth and Moum, 2000).

## 2.2 Entrainment

Entrainment plays an important role for dynamics and evolution of clouds. This was already pointed out in the mid 1950's by Stommel (1947) and Squires and Warner (1957). Entrainment defines the turbulent transport of dry, sub-saturated environmental air into the cloud region. Thereby, one distinguishes between two types of entrainment processes: i) cloud-top entrainment which is characterised by penetrative downdrafts into the cloud region from above and ii) lateral entrainment leading to the transport of sub-saturated environmental air into the cloud region from the side. The first kind is mostly detected at top of stratiform clouds, while lateral entrainment is a major characterisation of cumulus clouds. Turbulence at top of a stratocumulus cloud is thought to be generated through thermodynamic destabilisation, for example due to radiative cooling and possible buoyancy reversal (e.g., Deardorff, 1980; Mellado, 2010), or through wind shear and the resulting Kelvin-Helmholtz instability (e.g., Wang et al., 2008). At the edge of cumulus clouds also wind shear and the resulting evaporative cooling effect are thought to be the major sources for turbulence and lateral entrainment (Heus and Jonker, 2008).

The instability due to radiative cooling is caused by the difference of longwave radiative transfer at cloud top. The radiation temperature of the cloud region is higher compared to the radiation temperature of the free troposphere above leading to a lower downward longwave radiative flux than the upward outgoing one. Consequently, the cloud top radiates thermal energy and cools spatially. Due to the inhomogeneity of the cloud top, some regions are more affected by radiative cooling compared to neighboring which leads to stronger descents of the air parcels in these

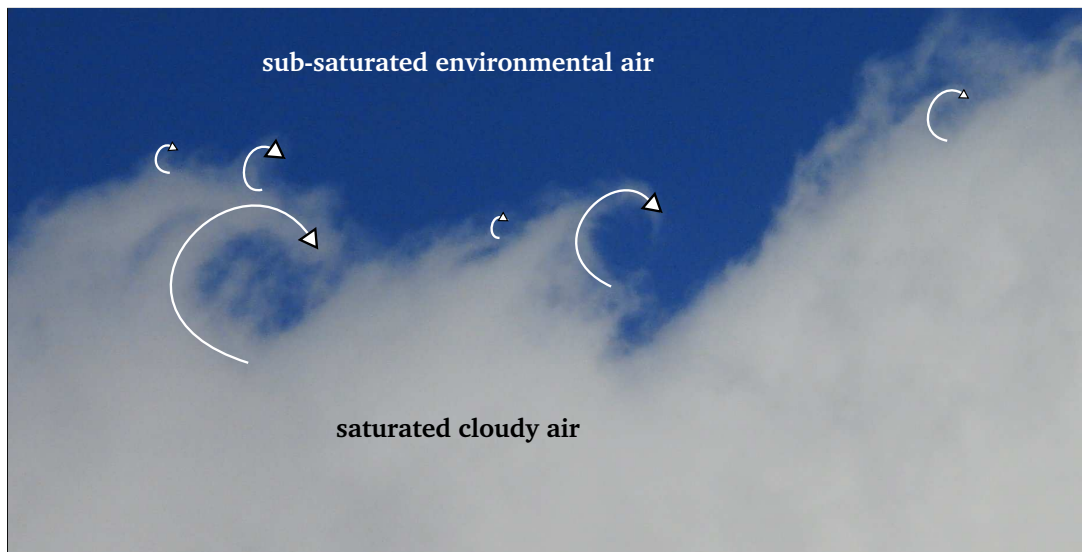


Figure 2.3: The picture shows the turbulent structure at cloud edge, whereby the white arrows illustrate eddies of different size.

regions.

Wind shear describes the variation of the flow in terms of speed and/or direction. Large-scale wind shear initiates the generation of turbulence through the deformation and distortion of air parcels resulting in a rotational movement.

A photo of a cloud edge illustrating the turbulent eddy structure is shown in Fig. 2.3. The sub-saturated environmental air located above the cloud region is transported into the cloud region by turbulent eddies of different size (marked with the white arrows in Fig. 2.3). The subsequent mixing with moist, saturated cloudy air leads to the evaporation of cloud droplets resulting in a cooling effect and the subsidence of air parcels. Thereby, the mixing time influences the kind of mixing within the cloud region. A fast mixing process leads to nearly similar fields of water vapour and temperature for all droplets which experience nearly the same saturation. Consequently, the droplet size distribution is shifted towards smaller diameters without a change in number concentration. This type of mixing is called homogeneous. If the mixing process proceeds slowly, the mixing type is called inhomogeneous. In this case, a fraction of droplets evaporates completely while a neighbouring droplet fraction remains unaffected. Consequently, the droplet size distribution remains constant but the number concentration will decrease (Lehmann et al., 2009). Hence, entrainment influences the fine-scale turbulent and microphysical structure of clouds.

### 2.2.1 Cloud-top entrainment

Cloud-top entrainment is a characteristic of stratocumulus as well as of cumulus clouds. In here, the focus is on entrainment at top of a stratocumulus layer. Such layers are located at top of the well-mixed boundary layer which is often strongly decoupled from the overlying free troposphere. The interface is typically characterised by sharp, vertical gradients in absolute humidity, potential temperature, aerosol concentration, and often horizontal wind velocity. Compared to the free troposphere, the boundary layer tends to be potentially colder and humid, with rather distinct dynamical and pollution properties. This is illustrated schematically in Fig. 2.4. The temperature inversion acts to suppress mixing but the small amount of turbulence that forms results in an important connection between the boundary layer and the troposphere, and the following entrainment is critical to cloud layer evolution (e.g., Stevens, 2002).

Formation of turbulence and evolution of turbulent mixing in a stable stratified environment are problems of broad geophysical interest and have been widely explored. Generally speaking, in flows with constant shear and density gradients the growth of turbulent kinetic energy is inhibited by buoyancy forces for Richardson numbers greater than approximately 0.1 (Peltier and Caulfield, 2003). For flows with spatially localised shear and stratification, such as often exists at stratocumulus cloud top, the Ozmidov length scale is expected to decrease with time as mixing progresses (Smyth and Moum, 2000). Such layers have been observed to grow to an asymptotic thickness as the shear contribution to the turbulent kinetic energy budget decays more rapidly than the buoyancy contribution of opposite sign (Brucker and Sarkar, 2007; Smyth and Moum, 2000). This interplay of destabilising shear and stabilising buoyancy is made further complex when the interface is bounded on one side by a cloud layer, leading to radiative and evaporative energy fluxes that tend to alter the energy budget and, therefore, the rate of turbulent mixing.

What is the nature of the cloud-top environment? Lenschow et al. (2000) showed through an analysis of DYCOMS (Dynamics and Chemistry of the Marine Stratocumulus; Lenschow et al. (1988)) data that the cloud/clear air transition is very sharp, but also that the interface is “leaky”, leading to a mixture of boundary layer and free-tropospheric air just above cloud top. In these studies there was very little vertical shear and we may ask, therefore, to what extent the leakiness depends on shear. Rogers and Telford (1986) observed one case with appreciable vertical

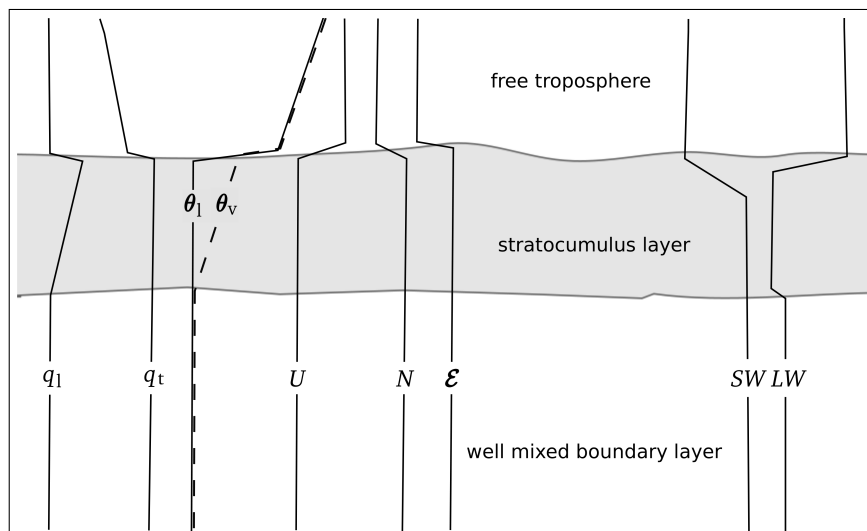


Figure 2.4: Stratification of a cloud-topped well-mixed boundary layer and the overlying free troposphere: vertical profiles of total water mixing ratio  $q_t$ , liquid water mixing ratio  $q_l$ , liquid potential temperature  $\Theta_l$ , virtual potential temperature  $\Theta_v$ , horizontal wind velocity  $U$ , number concentration of interstitial aerosol  $N$ , energy dissipation rate  $\varepsilon$ , net shortwave  $SW$  and net longwave  $LW$  radiation fluxes.

shear in which a clearly defined, 10 to 15 m–thick, transition layer formed between cloud top and the inversion. They argued that the layer acts as a buffer against entrainment instability: direct mixing between cloud and free troposphere would support the instability, but mixing across the entire transition layer is damped. Large eddy simulations (LES) demonstrate that this conditioned layer is almost always present above stratocumulus cloud tops and that its maintenance is related to ‘local’ shear effects due to convective eddies (Moeng et al., 2005). High spatial resolution measurements have provided further characterisation of what has been termed the “entrainment interface layer”, consisting of filaments of clear and cloudy air over a wide range of sizes down to the instrument resolution of 10 cm (Gerber et al., 2005; Haman et al., 2007). Based on those measurements it was suggested that after multiple mixing events the entrainment interface layer becomes as buoyant as the air at cloud top (Gerber et al., 2005). de Roode and Wang (2007) provide further observational evidence from FIRE I and refer to the process as detrainment, through which diluted, but still saturated air forms a local environment at the cloud boundary. The dependence of the interface layer on shear was highlighted in the LES studies of Wang et al. (2008), who observed that the layer thickness increases with shear intensity, and noted that the inversion layer tends to evolve to a constant

bulk Richardson number of approximately 0.3.

### 2.2.2 Lateral entrainment

Lateral entrainment is a common feature at the edges of cumulus clouds. Followed by subsequent mixing between sub-saturated environmental and cloudy air, it leads to the development of a thin “subsiding shell” at cloud edge. A first indication of this shell was given by laboratory experiments performed by Woodward (1959) which indicated a cumulus cloud as a thermal characterised by a body of updrafts surrounded by a shell of downdrafts. This picture was further clarified by aircraft and radar studies of small, maritime cumuli by Jonas (1990) and Knight and Miller (1998). Jonas (1990) further pointed out that the presence of the subsiding shell increases the entrainment instability at cloud edge by transporting cloud-top air to lower levels of the cloud. Tracer experiments performed by Stith (1992) confirm such transport and showed the lateral entrainment of these tracer parcels at lower levels. Hence, not only sub-saturated environmental air is entrained into the cloud core region at one level diluting the rising air parcel within the cloud core region. Also cloud-top air or detrained cloud air from different levels can be entrained into the cloud core region (Abma et al., 2013). This complex picture is illustrated in Fig. 2.5 in the upper part although the entrainment process takes place at all levels of the cloud.

The first assumption of Jonas (1990) referred to a mechanical forcing behind the downdrafts within the subsiding shell, but this was refuted by aircraft observations performed by Rodts et al. (2003). They observed a conspicuous dip in the virtual potential temperature profile and no dip in the total water mixing ratio profile at cloud edge, providing evidence for evaporative cooling as the driving mechanism of the subsiding shell. These findings are illustrated in the lower part of Fig. 2.5 where  $w$ ,  $B$ , and  $\Theta_v$  show a dip at cloud edge and  $q_t$  just changes from environmental to cloud value. The observations of Rodts et al. (2003) were compared with large eddy simulations by Heus and Jonker (2008) and the numerical calculation of the individual terms of the vertical momentum equation confirmed the assumption that buoyancy is the dominant force in the subsiding shell. Heus and Jonker (2008) discussed further that the transport of cloud-top air down to lower levels within the subsiding shell refreshes the air at cloud edge which influences the lateral mixing process and could create a stronger subsiding shell. The same effect can also be generated by an increase in aerosol particle number concentration which seems to



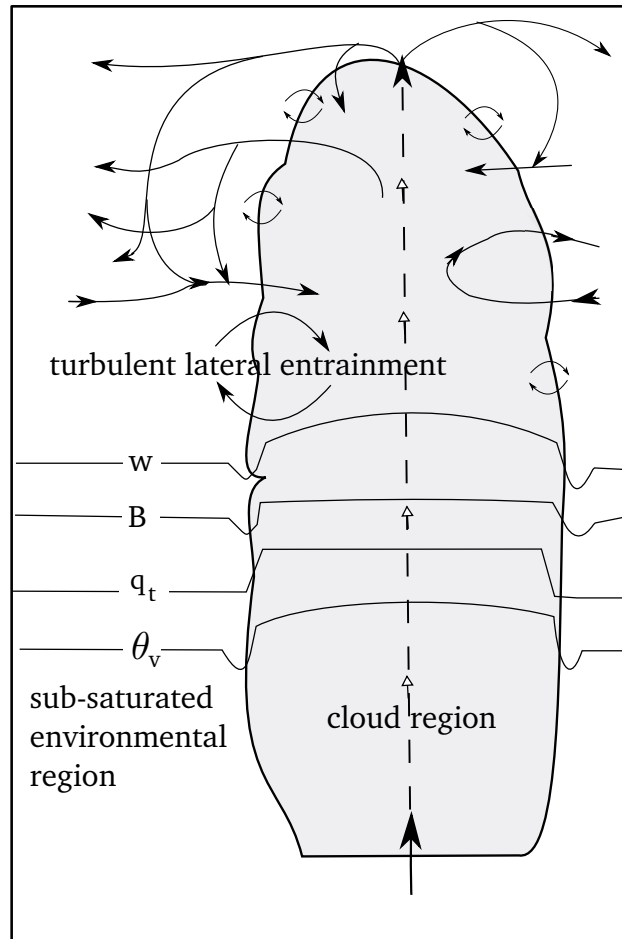


Figure 2.5: Schematic picture of a few aspects of cumulus dynamics and a horizontal cross section of mean parameters such as total water mixing ratio  $q_t$ , liquid-water potential temperature  $\Theta_l$ , vertical wind velocity  $w$  and buoyancy  $B$  within the environmental and cloudy region.

enhance the evaporative cooling rate at cloud edge, leading to enhanced negatively buoyant air at cloud edge (Small et al., 2009). The important role of the subsiding shell for cloud dynamics is further indicated by the increased turbulence intensity within the shell (Siebert et al., 2006b) and the different air properties between subsiding shell and far-environment in terms of humidity and buoyancy (Jonker et al., 2008). The latter has influences on the mixing process at cloud edge in terms of inhomogeneous and homogeneous mixing (Gerber et al., 2008b) influencing further the cloud microphysics.

Detailed analysis of the shell properties, however, has been challenging because the horizontal extent of a typical shell is comparable to or less than the resolution of LES

cloud models or of aircraft data. Two detailed studies of the structure of cumulus clouds are given by Wang et al. (2009) and Wang and Geerts (2010). The first one analysed the dynamics of the cloud margin with a thickness of 10% of the cloud diameter which is characterised by descending and relatively cold air. The second study characterised three main facts of the cloud edge: negative buoyancy, cold anomaly, and local subsidence. Nevertheless, they were not able to resolve the small-scale fluctuations due to a spatial resolution of 10 m and 5 m, respectively. Also, LES do not resolve the smallest scales leading to an underestimation of the subsiding shell by LES compared to observations (Heus et al., 2009). Abma et al. (2013) addressed these LES limitations by performing the first fully resolved computational study of the fine-scale structure of turbulent mixing and the formation of a subsiding shell. The time evolution of a small portion of an idealised subsiding shell was analysed based on direct numerical simulations (DNS). The results show that during the lateral entrainment and mixing process, the thickness of the subsiding shell grows quadratically and the downdrafts increase linear with time. Coupling to large scales remains an open aspect of this problem, however. This indicates that the quantification of the lateral entrainment process is not trivial.

With the closure of this Chapter the basic ideas of turbulence and entrainment are formulated which are essential for the understanding of the following analysis. The next Chapter deals with the basics concerning measurement technique and experimental set-up.

# 3 Airborne Cloud Turbulence Observation System

For the analysis of the numerous above mentioned meteorological problems, highly-resolved in-situ measurements are necessary. Within this thesis, the fine-scale measurements in the cloudy boundary layer are performed with the helicopter-borne measurement payload ACTOS (Airborne Cloud Turbulence Observation System). The combination of a low true airspeed and a high sampling frequency enables a spatial resolution down to cm-scale. High-resolution measurements are performed for meteorological standard parameters (e.g. temperature, humidity, and pressure), turbulence, and microphysical properties of clouds (e.g., liquid water content, droplet size and number distribution). The following Chapter is aimed to introduce the measurement payload starting with a general overview which is followed by brief descriptions of the individual measurement techniques and the data post-processing.

## 3.1 General overview

The airborne measurement payload ACTOS for fine-scale measurements has a long-lived development. The platform was designed to measure meteorological standard parameters (temperature, wind vector, humidity and pressure), microphysical properties (liquid water content, number concentration of interstitial aerosol), and payload position and attitude. This first version of ACTOS had a length of 4 m and a total weight of 140 kg with a frame made of aluminium. First tests were performed in April 2000 followed by a first field campaign at the German North Sea, Meldorfer Bight, in September and October 2000. The first version of ACTOS was carried 25 m below a tethered balloon called MAPS-Y. Detailed information concerning the first version of ACTOS and the first measurement campaign are given in Siebert et al. (2003). Since then, the payload was subject to continuous improvements and

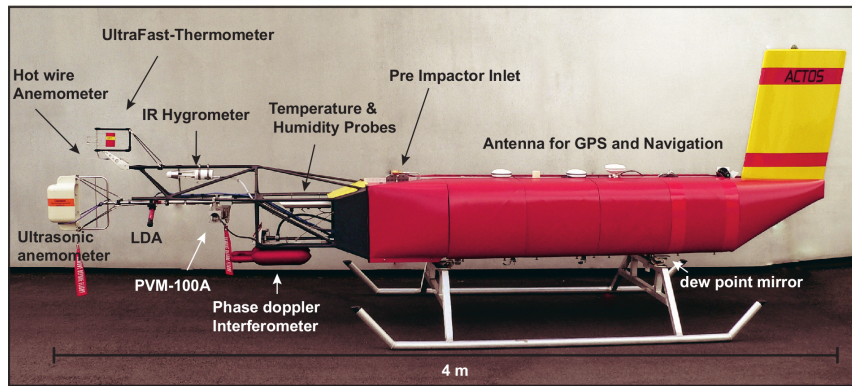


Figure 3.1: General overview of the current version of ACTOS with its instrumentation.

changes concerning the instrumentation. Additionally, the carrying system changed from the tethered balloon to a helicopter with the advantage of an increased flight height and flexibility and an increased external load. A picture of the current version of ACTOS and its instrumentation is given in Fig. 3.1. The length of the payload is  $\approx 4\text{ m}$  but the total weight including instruments is increased to the maximum of 200 kg. The weight of the frame is reduced using carbon fibre and aluminium. Most of the instruments are located in the frontal part (left side of Fig. 3.1): thermodynamic sensors (temperature and humidity probes, infrared hygrometer, ultrasonic anemometer), sensors with a high sampling frequency (hot-wire anemometer, Ultra-Fast Thermometer (UFT)), and microphysical sensors (Particle Volume Monitor (PVM-100A), Phase-Doppler Interferometer (PDI), Laser Doppler Anemometer (LDA)). These instruments are spatially collocated within a few tens of cm. The body includes further instruments (e.g., scanning mobility particle sizer for aerosol measurements), the power supply, and the data acquisition system. Additionally, the navigation system and the GPS are located in the middle part. The tail in the back keeps ACTOS in a stable flight direction.

The current payload is located on a 140 m-long rope below the helicopter. It operates with a true air speed ( $TAS$ ) of  $20\text{ m s}^{-1}$  and has a climbing rate of  $2\text{ m s}^{-1}$ . The minimum  $TAS$  is a compromise between a stable flight condition of the helicopter and maximum resolution of the measurements. At that rate, the measurements are not influenced by the rotor downwash. A schematic picture of the deflection of the rotor downwash is shown in Fig. 3.2, which is taken from Siebert et al. (2006a). During the flight, the instruments are energised by rechargeable batteries and the data acquisition system records the data in real time. The payload works autonomously

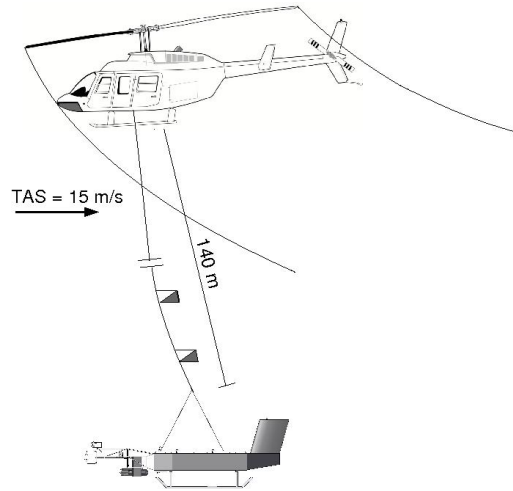


Figure 3.2: A schematic picture of helicopter and ACTOS during a flight situation. The rotor downwash is deflected backwards by a true air speed of 15 – 20  $\text{m s}^{-1}$ . The figure is taken from Siebert et al. (2006a)

and only standard parameters are transmitted on-line to the helicopter where they are monitored by a scientist. Measurements could be performed up to a height of 3 km. All measurements are limited in relation to the visual flight rules for the helicopter. One consequence of the flight-safety regulations is that the helicopter has to stay outside of the cloud while ACTOS performs measurements in the first  $\simeq 100$  m below cloud top. For further informations concerning ACTOS the reader is referred to Siebert et al. (2006a).

## 3.2 Instrumentation

This section deals with a brief description of the functionality and performance of the instruments which are necessary for the analysis of this work. At first all measurements are summarised in Tab. 3.1 which gives the sensor type, the measured variables, and the manufacturer. A comprehensive description of most of the measurement equipment can be found in Siebert et al. (2003).

Sensor	Parameter	manufacturer
Ultra sonic anemometer	$u, T_v$	Gill Instruments, Lymington, UK
Hot-wire anemometer, mini CTA	$U$	Dantec Dynamics A/S, Skovlunde, Denmark
Ultra-fast thermometer, type 55P11	$T$	Dantec Dynamics A/S, Skovlunde, Denmark
Dewpoint Hygrometer, type TP3-ST	$T, T_d$	Meteolabor AG, Switzerland
LiCor 7500	$a$	LI-COR corporation, Lincoln, Nebraska USA
BAROCAP Barometer, type PTB220	$p$	Vaisala, Helsinki, Finland
Condensation particle counter, model 3762A	$N$	TSI Inc., St. Paul, MN, USA
Particle volume monitor, type PVM-100A	$LWC, PSA$	Gerber Scientific, INC., USA
Phase Doppler Interferometer	$N_d, D_d, v_d$	Artium Technologies Inc., Sunnyvale, CA, USA
NAVIGATION		
IMU, type INAV-1700	$\Phi, \Upsilon, \Psi, \Omega, U_P$	IMAR Navigation GmbH, St. Ingbert, Germany
GPS, type VectorPro	$\Phi, \Upsilon, \Psi, \Omega, U_P$	CSI Wireless, INC., Calgary, Canada
Acra KAM-500	data acquisition	Acra Control (now Curtiss Wright), Parsippany; NJ, USA

Table 3.1: Summary of the instruments included in the following analysis.

### 3.2.1 Wind velocity measurements

An ultra-sonic anemometer Solent HS (hereafter called “sonic”) is used to measure the three-dimensional wind vector and the virtual temperature. The measurement bases on the time-of-flight principle. Therefore, the system consist of six transducers orientated on three axes whereby in each case two transducers act as pair. Each of these two is emitter as well as detector for short ( $< 1$  ms-long) ultrasound pulses. The pulses are emitted in a moving medium and the times of flight of these pulses in each direction are measured. The measurement of the sonic temperature utilise the dependence of the sonic speed on temperature. The measurements were performed with a sampling frequency of 100 Hz whereby the measurement resolution are  $\Delta\bar{u} = 0.01 \text{ m s}^{-1}$  and  $\Delta\bar{T} = 0.01 \text{ K}$ . Further information concerning the composition and functionality are given by GILL Instruments (2004) and Siebert and Muschinski (2001). The sonic measurements are corrected for attitude and platform velocity and the wind vector is transformed into an Earth-fixed system (Siebert et al., 2006b). A short description of the correction is given in section 3.3.

A one-component hot-wire anemometer measures the horizontal wind velocity  $U$ . It consists of a thin tungsten wire ( $5 \mu\text{m}$ ) from Dantec Dynamics A/S which is plated with platinum. The measurement bases on a constant wire temperature, whereby the convective heat transfer between the flow and the wire is measured. The measurement technique and adequate sensors are described by the manual of Dantec Dynamics A/S (2012) and Wendisch and Brenguier (2013). The sampling frequency of the hot-wire anemometer is 2192 Hz. The influence of droplet impactions on the thin wire under cloudy conditions has to be considered by applying a despiking algorithm described in Siebert et al. (2007). After using this algorithm, a non-overlapping block average over 5 samples is applied within this analysis which leads to a final sampling frequency of 438 Hz. In the post-processing, the hot wire data are calibrated with the sonic data. The despiking and calibration algorithm are described in section 3.3.

### 3.2.2 Temperature, humidity, and pressure measurements

Beside the virtual temperature measurements of the sonic, highly-resolved temperature measurements are performed with an Ultra-Fast Thermometer (hereafter called “UFT”). The UFT is a modified version of the instrument described in Haman et al.

(1997). The measurement bases on the resistance of a thin wire from Dantec Dynamics A/S with a diameter of  $2.5\ \mu\text{m}$  with a resistance of about  $12\ \Omega$ . In front of this wire a shaped rod is mounted which protects the wire from cloud droplet impaction. A wind vane behind the sensing wire fixes the position upwind. The whole system is rotatable and can change its position with respect to the local instantaneous flow.

The dew point temperature  $T_d$  is measured with a dew point mirror consisting of a mirror plane, which is cooled electrically down to the condensation point of water vapour. The detection of this point bases on the decreased optical reflectivity of the mirror due to the condensed water vapour on the plane. The corresponding dew point temperature is measured with a thermocouple, while a second thermocouple measures the air temperature. The dew point mirror has a time resolution of 1 s. Further information are given by the manual of Meteolabor AG (2010).

The absolute humidity  $a$  is measured with a LiCor 7500 (manual of LI-COR, Inc., 2009). It is an absolute, non-dispersive open-path gas analyser and bases on the infrared absorption of water vapour and  $\text{CO}_2$  molecules according to the Lambert-Beer law. Infrared radiation is emitted on one side of the 12.5 cm-long pathway and the reduced radiation is detected with a lead selenide detector on the other side. The measurements were performed with a sampling frequency of 20 Hz. The measurement of the amount of  $\text{CO}_2$  was not object of this work.

The static pressure  $p$  is measured with a Vaisala BAROCAP Barometer PTB220 (manual of Vaisala, 1999). The measurement bases on a silicon capacitive absolute pressure sensor with an absolute accuracy of  $\pm 0.3\ \text{hPa}$  at  $20^\circ\text{C}$  and a resolution of 1 Pa (e.g., a vertical displacement of 10 cm can be resolved). The measurements were performed with a sampling frequency of 100 Hz.

### 3.2.3 Aerosol and cloud droplet measurements

The number of interstitial aerosol  $N$  is measured with a condensation particle counter (CPC, model 3762, TSI Inc.). The sensor consists of 3 main parts: (1) saturator, (2) condenser, and (3) optics. Through the pre-impactor inlet the sub-micrometer particles are transported to a heated saturator block where the aerosol is saturated



with respect to a working fluid. Afterwards, the particles are led through a cooled condenser tube where the sub-micrometer particles are coated with a condensable vapor (n-butyl alcohol) to grow by condensation to an optically detectable size (e.g.,  $10\ \mu\text{m}$  in diameter). These droplets are detected individually by the optics and following electronics post-process the signal. Afterwards, the data are converted into the number concentration using the sample flow rate. The used CPC measures particles with a diameter of  $> 6\ \text{nm}$ . For further informations the reader is referred to the manual of TSI Inc. (2000).

The liquid water content  $LWC$ , particle surface area ( $PSA$ ), and the effective droplet radius ( $r_{eff}$ ) of cloud droplets are measured with a particle volume monitor, PVM-100A (Gerber et al., 1994). On one side of a pathway a laser-diode light source (with a wavelength of  $780\ \text{nm}$ ) is located and the optics and detectors are located on the other side. The sampling tube is faced into the wind direction and is passed-by the laser beam. The droplet ensemble that passes the sampling volume of  $1.25\ \text{cm}^3$  scatter the laser light into the near-forward direction and a lens focuses this scattered light on a transmission filter and corresponding sensors. One signal is proportional to  $LWC$  and the other one is proportional to the  $PSA$  and  $r_{eff}$  which is given by  $r_{eff} \sim \frac{3}{\rho_w} \frac{LWC}{PSA}$  (Gerber et al., 2008a).

The Phase Doppler Interferometer (PDI, Artium Technologies Inc.) measures the size and velocity of the cloud droplets. Thereby, a laser beam is splitted into two beams which cross each other under a known angle. The intersection area forms the probe area. If a droplet passes this probe area, it scatters the laser light which is detected by three spatially separated detectors. The phase shift between two of these signals is inversely proportional to the droplet diameter. Afterwards, the droplet number concentration, liquid water content and droplet size distribution can be estimated. The most striking advantage is that the instrument does not rely on the intensity of the scattered light to determine droplet size, but the wavelength of the scattered light. The droplet velocity is measured based on the Doppler frequency. Further information is given in Chuang et al. (2008).

### 3.2.4 Navigation

In addition to the atmospheric measurements on ACTOS, the velocity components, attitude, and position of the payload itself are measured. These measurements

are necessary to translate the measured wind vector from the platform coordinate system into an Earth-fixed system (see Chapter 3.3). The position, velocity, and attitude are measured with two different systems: i) a dGPS (differential global positioning system, Vector Pro by CSI Wireless, Inc., Calgary, Canada) and, ii) an inertial navigation system (iNAV by iMAR Navigation GmbH, St. Ingbert, Germany). The “strap-down” inertial navigation system (see Wendisch and Brenguier (2013) for a general overview of airborne navigation issues) provides attitude angles, angular rates, and payload velocity components. The system mainly consists of three orthogonally-fixed fibre-optical gyros and accelerometers with an output rate of 10 Hz. To minimize drift effects of the inertial sensors, these readings are combined with long-term stable dGPS data in particular platform velocity and yaw angle. This combination is performed in real-time by a navigation computer.

During the flight, all data are collected in real-time with an airborne data acquisition unit type KAM-500 (Acra Control Ltd., Dublin, Ireland). The data is stored on-board on a compact flash card and partially transmitted to the helicopter for monitoring.

### 3.3 Data post-processing

#### 3.3.1 Wind vector transformation

The three-dimensional wind vector as measured by the sonic refers to a payload fixed coordinate system. Therefore, the wind vector has to be transferred into an earth-fixed system (east, north, up) by applying an Euler transformation. The transformation is performed using the method described in Edson et al. (1998) where the wind vector in the Earth-fixed System ( $\vec{u}_e = (u_e, v_e, w_e)$ ) can be calculated as:

$$\vec{u}_e = \mathbf{C}_p^e \vec{u}_s + \vec{\Omega} \times \mathbf{C}_p^e \vec{M} + \vec{u}_P. \quad (3.1)$$

Here,  $\vec{u}_s = (u_s, v_s, w_s)$  denotes the velocity vector measured with the sonic in platform coordinates which is transformed to earth coordinates using the rotation matrix  $\mathbf{C}_p^e = \mathbf{R}_z(\Psi) \cdot \mathbf{R}_y(\Upsilon) \cdot \mathbf{R}_x(\Phi)$  where  $\mathbf{R}$  denotes the three basic rotation matrices around the axes x, y, z. The second term in Eq. 3.1 includes the angular velocity

vector  $\vec{\Omega}$  and the position vector  $\vec{M}$  of the anemometer with respect to the navigation unit (here, the anemometer is located 2 m in front of the navigation unit). With the third term, the translational velocity vector of the platform with respect to the Earth-fixed system  $\vec{u}_P = (u_P, v_P, w_P)$  is considered.

### 3.3.2 Calibration of hot-wire data

The hot-wire data have to be corrected concerning the droplet impactions and to be calibrated. The impact of a droplet on the thin wire leads to a sharp increase of the signal due to evaporation of the droplet on the wire. Such increase has a duration of  $\approx 5$  samples corresponding to 0.5 ms (sampling frequency = 2192 Hz, see hot-wire description above). To detect such sharp increases within the signal the forward differences are calculated. If these differences are larger than a certain threshold, the data point is replaced by the value of the running median which is calculated parallel and which does not include the droplet signal. Averaging over 5 values leads to the final sampling frequency of 438 Hz.

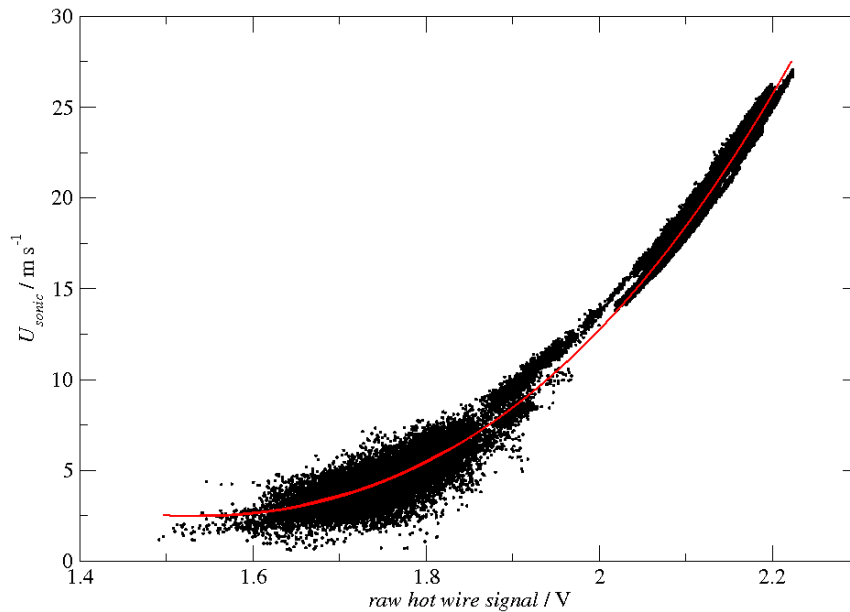


Figure 3.3: Calibration of the hot wire data using the sonic data. The black dots denote the measured values and the red line marks the fitted curve.

After despiking, the data are calibrated by means of the sonic data. The one-component hot-wire only measures the horizontal wind velocity, therefore the hot-

wire data are plotted with the horizontal wind velocity of the sonic ( $U = \sqrt{u^2 + v^2}$ ) (Fig. 3.3). The curve is fitted by a polynomial of third order.

# 4 Turbulent inversion layer above a marine stratocumulus cloud

The impact of cloud-top entrainment and subsequent mixing of potential warm and dry free-tropospheric air with potential cool and moist cloudy air on the fine-scale structure of a stratocumulus layer is analysed. High-resolution measurements at top of a stratocumulus layer above the Baltic Sea show a turbulent mixing layer (TIL) above the cloud. This layer is driven by shear-induced cloud-top entrainment and seems to be actively coupled with the cloud layer. After the presentation of the measurement campaign and the weather conditions during the observation period, the different layers around cloud top including the TIL are analysed and the consequences for the entrainment process are discussed.\*

## 4.1 Campaign and Meteorology

The observations of the turbulent and thermodynamic structure of a stratocumulus-cloud-topped marine boundary layer were performed in October 2007 above the Baltic Sea. The measurement site was located in the North of Germany above the Kiel Bay which is illustrated in Fig. 4.1. Logistical aspects and the infrastructure at the airport of Kiel were the main reasons for this measurement site, although it is not such a typical region for stratocumulus development as for example the west coast of South Africa or South and North America (where appreciable campaigns took place, e.g., DYCOMS II (Stevens et al., 2003)). However, the North-Atlantic lows which move within the westward flow transporting cool and moist air towards the southwest region of the Baltic Sea (Feistel et al., 2008; Rheinheimer and Nehring, 1996) and the local land-sea wind circulation cause a maritime influence on the weather conditions.

---

\*Please note that some parts of the following chapter including Fig. 4.4 to 4.9 are taken from Katzwinkel et al. (2012) without further notice.

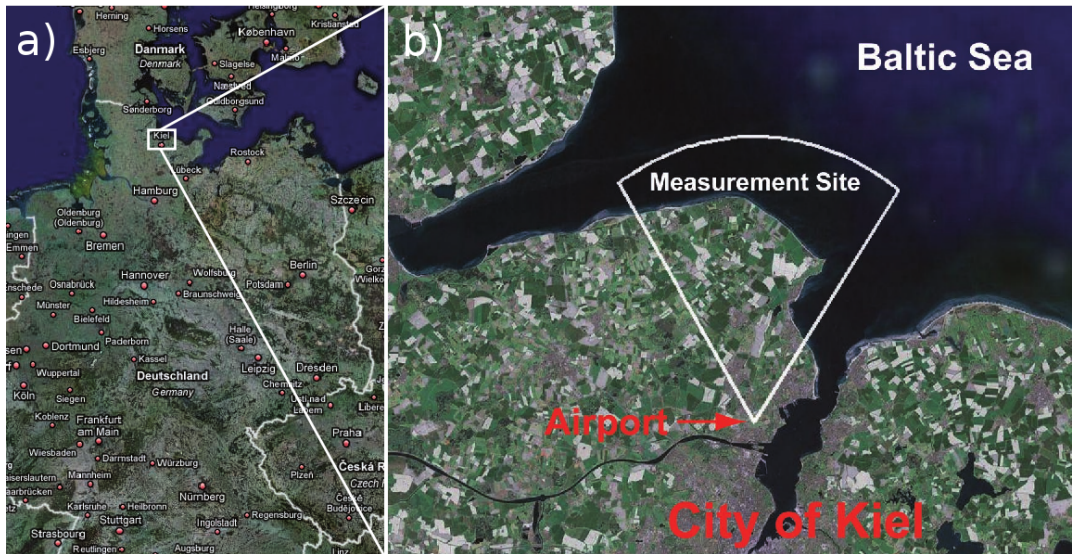


Figure 4.1: Measurement site: a) Location of Kiel in the north of Germany and b) detailed view of Kiel with the airport and the measurement site above the Baltic Sea.

A typical aspect of the local wind circulation is the development of a sea front which leads to the change of wind direction and velocity and additionally to the change from more continental to maritime weather conditions (Feistel et al., 2008). As a consequence of an intensive local circulation, the typical sea cloudiness consisting of a broad stratocumulus with occasional precipitation develops. Such cloud conditions were present on the measurement day and are described in the next section.

## 4.2 Weather conditions

The local weather conditions during the analysed measurement flight on 8th October, 2007 which was performed between 0930 and 1100 UTC are presented in the following. Selected conditions during the profile measurements above the Sea are plotted in Fig. 4.2. A well-mixed boundary layer is observed with height-independent mean potential temperature of  $\Theta = 285 \text{ K}$  and a mean absolute humidity  $a = 5 \text{ g m}^{-3}$  slightly decreasing with height up to a temperature inversion at a height of 1.3 km. The horizontal wind velocity  $U$  shows high variability between  $5 - 20 \text{ m s}^{-1}$  in the lower part of the boundary layer up to  $\approx 750 \text{ m}$  while the part above is characterised by  $U \approx 6 \text{ m s}^{-1}$ . Around the inversion layer at  $\approx 1300 \text{ m}$  height,  $U$  shows an increase to  $11 \text{ m s}^{-1}$ . The wind direction shows high fluctuation between south-southeast and

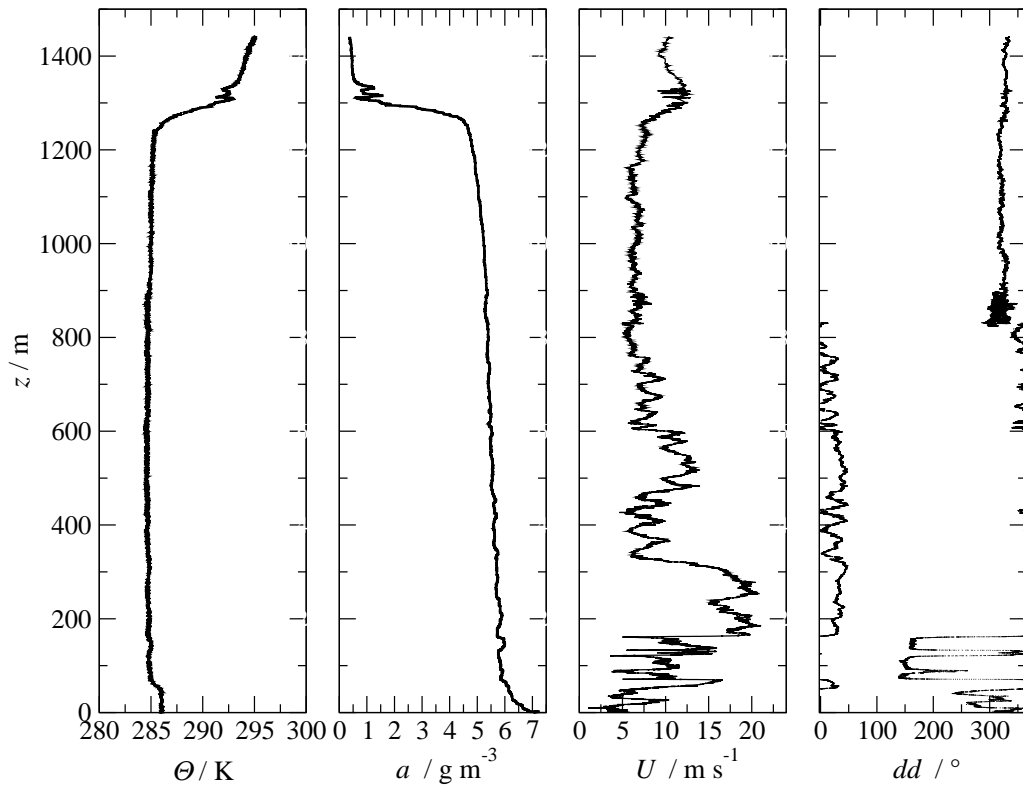


Figure 4.2: Stratification of the atmospheric boundary layer and the lowest free troposphere above the Baltic Sea near Kiel in the north of Germany on October 8th, 2007.

north below 180 m, above this height the wind changes more and more to northerly direction with constant directions from north above 750 m height.

On the measurement day, the well-mixed marine boundary layer was topped by a broad stratocumulus layer. A view from the helicopter on the top of such a cloud layer is presented in Fig. 4.3 which shows the homogeneous and flat cloud structure. Based on meteorological information from the airport, the coverage of the lowest clouds was 7/8 and the cloud base was located at heights between 900 – 1100 m during the observation period. On this day, the 200 to 300 m–thick stratocumulus layer was topped by a temperature inversion with a vertical extension of about 50 m. The following analysis refers to measurements at heights between 1.1 and 1.4 km including the upper part of the stratocumulus layer, the TIL, and the lowest part of the free troposphere. The thermodynamic and turbulent structure of these layers is analysed based on six “dolphin-like” profiles around cloud top with a vertical peak-to-peak amplitude of approximately 300 m. Thereby, ACTOS was dipped into the cloud from above, while the helicopter has to stay outside due to the visual flight



Figure 4.3: Photograph of the stratocumulus layer above the Baltic Sea on 8th October, 2007.

restrictions.

### 4.3 Results

The analysis of the cloud top region and the TIL starts with the time series of selected parameters of the single measurement flight presented in Fig. 4.4. The sampling strategy is illustrated by means of the measurement height ( $z$ ) shown in panel a), the cloud is indicated by the  $LWC$  in panel b),  $\Theta_l$  and  $a$  are shown in panel c), and  $U$  and  $N$  are presented in panel d).

The cloud layer is characterised by a maximum  $LWC \approx 0.4 \text{ g m}^{-3}$ , a mean  $\Theta_l \approx 285 \text{ K}$  and  $a \approx 5 \text{ g m}^{-3}$ . The aerosol particle number concentration  $N$  inside the cloud layer fluctuates between  $500 \text{ cm}^{-3}$  and  $900 \text{ cm}^{-3}$ . The free troposphere above the cloud is characterised by  $\Theta_l \approx 293 \text{ K}$ ,  $a \approx 0.7 \text{ g m}^{-3}$  and a nearly constant  $N \approx 150 \text{ cm}^{-3}$ . In between, the shaded regions marks periods when the TIL was passed, which is characterised by a strong wind shear where  $U$  increases from  $6 \text{ m s}^{-1}$  inside the cloud layer to  $11 \text{ m s}^{-1}$  in the free atmosphere and all other parameters gradually change from their in-cloud values to the free-tropospheric ones. In total, the TIL was passed six times during the flight, marked by the Roman numbers at top of the shaded areas.

Figure 4.5 shows a more-detailed view of the turbulent and thermodynamic prop-



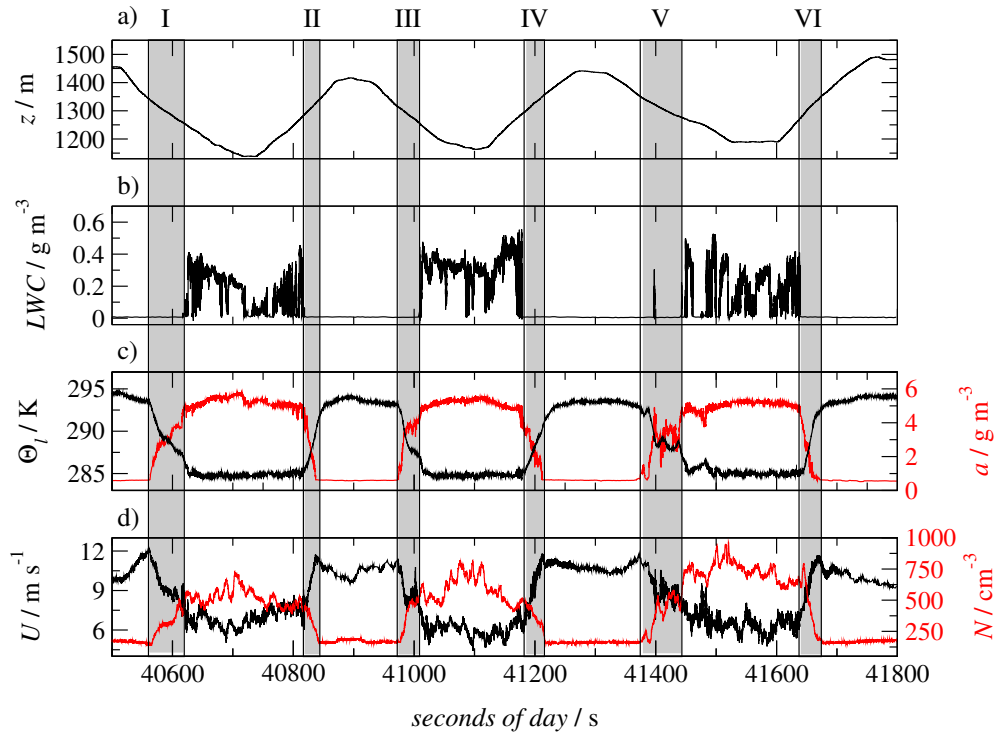


Figure 4.4: Time series of six subsequent profiles at the top of a marine stratocumulus layer. The following data are shown: a) height ( $z$ ), b) liquid water content ( $LWC$ ), c) liquid water potential temperature ( $\Theta_l$ ) in black and absolute humidity ( $a$ ) in red, d) horizontal wind velocity ( $U$ ) in black and number concentration of interstitial aerosol ( $N$ ) in red. The mean true airspeed of ACTOS was  $14 \text{ m s}^{-1}$ . The grey boxes mark the respective turbulent inversion layer (TIL) of each profile.

erties for one penetration through the TIL (transit IV in Fig. 4.4). The first four panels (Fig. 4.5 a, b, c, and d) display  $LWC$ ,  $\Theta_l$ ,  $a$ ,  $U$ , and  $N$ . In the following three panels (Fig. 4.5 e, f, and g) the turbulence is characterised by means of  $Ri$ ,  $\bar{\epsilon}_\tau$ , and  $\sigma_w^2/\sigma_u^2$ . For the calculation of these parameters the reader is referred to sections 2.1.7, 2.1.4 and 2.1.2, respectively. In practice, the gradient Richardson number  $Ri$  is calculated from differences in  $U$  and  $\Theta$  over a height difference of 5 m, and then smoothed with a 25 m vertical running average. Additionally, within Fig. 4.5 e, the critical value of  $Ri_c = 1$  is marked with a vertical black line. Here, the energy dissipation rate is calculated with an integration time of  $\tau = 1 \text{ s}$  which corresponds to 100 samples. The last panel (Fig. 4.5 g) presents the ratio of  $\sigma_w^2/\sigma_u^2$  as a measure of local isotropy of the velocity field. Each value is estimated from a subrecord of

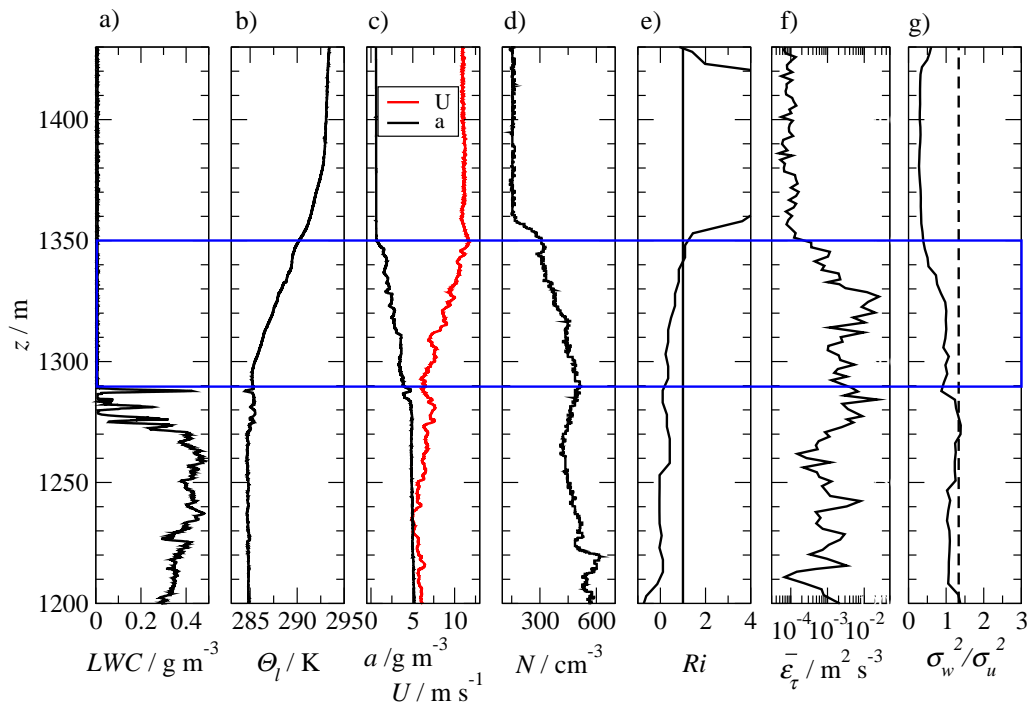


Figure 4.5: Vertical profiles of: a) liquid water content ( $LWC$ ), b) liquid water potential temperature ( $\Theta_l$ ), c) absolute humidity ( $a$ ) in black and horizontal wind velocity ( $U$ ) in red, d) number concentration of interstitial aerosol ( $N$ ), e) gradient Richardson number ( $Ri$ ), with  $Ri = 1$  marked with the vertical black line, f) local energy dissipation rate ( $\bar{\varepsilon}_\tau$ ) and g) local isotropy ( $\sigma_w^2/\sigma_u^2$ ), with  $\sigma_w^2/\sigma_u^2 = 4/3$  marked with the vertical dotted line. The horizontal blue lines denote the turbulent inversion layer (TIL), as defined by the level at which  $Ri = 1$ . For this example the inversion layer extends somewhat higher than the interfacial layer. The profile corresponds to transit IV in Fig. 4.4.

100 samples similar to the length as for  $\bar{\varepsilon}_\tau$ . It has to be pointed out that the lower integration limit is determined by the length of the subrecord and, therefore,  $\sigma_u^2$  and  $\sigma_w^2$  do not represent the entire layer and contributions from larger structures are filtered out. Here, the value is used in a qualitative way to distinguish between the different conditions in the cloud and the TIL. Observations in the atmosphere reveal ratios for isotropic flows in the range of 1 to 4/3 (Biltoft, 2001). Therefore, the value  $\sigma_w^2/\sigma_u^2 = 4/3$  is marked with the dashed line in Fig. 4.5 g.

The vertical profiles in Fig. 4.5 illustrate the remarkably linear transition from boundary-layer to free-tropospheric values of  $a$ ,  $U$ , and  $N$ . The blue horizontal lines in Fig. 4.5 denote the TIL, as defined primarily through the wind shear, and

to a lesser extent through the absolute humidity. Interestingly, in this profile the inversion layer ( $\Theta_l$ ) actually extends slightly higher into the troposphere than the TIL (as is the case with four of the other six profiles shown in Fig. 4.4). Panels e and f show that the TIL is characterised by  $Ri$  slightly less than 1, and approximately constant  $\bar{\epsilon}_\tau$  at about the same levels as in the underlying cloud layer. A difference between the cloud layer and the TIL is clearly seen in the local isotropy ratio shown in panel g). While inside the cloud layer the turbulence tends to be isotropic, the ratio decreases significantly below one inside the TIL representing anisotropy and increasingly two-dimensional turbulence. It should be noted that this departure from isotropy casts some doubt on the precise estimates of  $\bar{\epsilon}_\tau$  because the connection to the second-order structure function (described in section 2.1.4) assumes homogeneous, isotropic turbulence (Siebert et al., 2010).

In order to get a more generalised picture of the cloud top and the TIL, the thermodynamic and turbulent properties are averaged over the six profiles. To accomplish the averaging the height was normalised according to the following two definitions:  $z_{norm} = 0$  denotes the cloud top characterised by  $LWC < 0.01 \text{ g m}^{-3}$  and  $z_{norm} = 1$  marks the top of the TIL (characterised by  $\frac{dU}{dz} \approx 0$ ). The averaged profiles are shown in Fig. 4.6 and display a qualitatively similar structure as the single profiles. The black lines represent the mean values and the dotted lines denote the maximum and minimum values of each parameter.

All averaged variables are nearly constant with height within the measured regions above and below the TIL, i.e., inside the cloud and in the free troposphere. In between lies the well-defined TIL, which covers nearly the whole inversion layer and acts as a turbulent entrainment region between the two bounding thermodynamic and dynamic regimes. Specifically, variables  $\Theta_l$ ,  $a$ ,  $U$ , and  $N$  change nearly linearly across the TIL from in-cloud to free-tropospheric values. At the same time,  $\bar{\epsilon}_\tau$  is essentially uniform across the cloud and the inversion layer, suggesting that the two regimes are strongly coupled dynamically:  $\bar{\epsilon}_\tau$  of  $\sim 10^{-3} \text{ m}^2 \text{ s}^{-3}$  is observed both in the cloud and in the TIL and decreases by nearly one order of magnitude at the top of the TIL. This is consistent with the Richardson number, which is below unity for the cloud and TIL and sharply increases at the boundary between the TIL and the free troposphere. However, the small-scale structure of the turbulence in the cloud and the TIL differs significantly in terms of isotropy. Due to the strong stratification inside the TIL, the turbulence tends to become more anisotropic and two-dimensional, which is typical for stably stratified flows (Mauritsen et al., 2007).

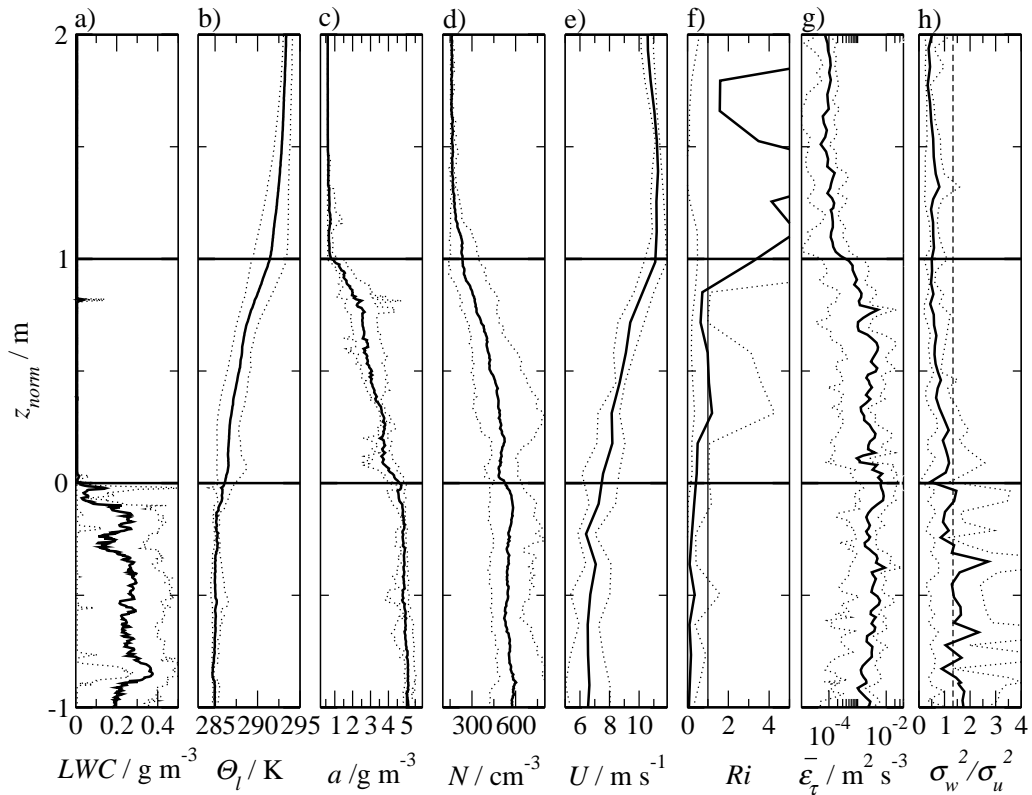


Figure 4.6: Mean profiles averaged over six individual soundings. Before averaging, the height was normalised with  $z_{norm} = 0$  denotes the height of cloud top and  $z_{norm} = 1$  marks the height of disappearance of the horizontal wind shear. The black lines represent the averaged values and the dotted lines mark the minimum and maximum values for the six profiles. Displayed are: a) liquid water content ( $LWC$ ), b) liquid water potential temperature ( $\Theta_l$ ), c) absolute humidity ( $a$ ), d) number concentration of interstitial aerosol ( $N$ ), e) horizontal wind velocity ( $U$ ), f) gradient Richardson number ( $Ri$ ), g) local energy dissipation rate ( $\bar{\epsilon}_\tau$ ) and h) local isotropy, with  $\sigma_w^2/\sigma_u^2 = 4/3$  marked with the vertical dotted line.

## 4.4 Conclusion

The porpoise-dive sampling strategy is often used in aircraft studies of marine stratocumulus cloud tops. For example, during the DYCOMS-II experiment (e.g., Haman et al., 2007) a similar approach led to the estimate of an entrainment interface layer of 0 – 70 m–thickness, based on high-resolution  $LWC$  and temperature measurements. It is important to recognise, however, that the ACTOS profiles should be interpreted somewhat differently because of the relative flight speeds.

The true airspeed of the C-130 aircraft is about  $100 \text{ m s}^{-1}$  with a climbing rate of about  $2 \text{ m s}^{-1}$ . Consequently, the aspect ratio of vertical to horizontal flight path is about 1:50 compared to 1:7 for the ACTOS flights. Therefore, the slant path taken through the turbulent inversion layer with the C-130 is much more influenced by large scale horizontal variability and the measurements tend to represent an averaged picture of the cloud top, even for single profiles. In contrast, in the ACTOS sampling scenario the slant path is considerably less than the depth of the boundary layer ( $\approx 1300 \text{ m}$ ), yielding an approximate ‘vertical profile’ by avoiding averaging over many boundary-layer scales.

The consistent picture of the TIL emerges in spite of significant variability observed in the layer thickness. The observed thickness  $\Delta z_{sub}$  of the TIL ranges from 37 to 85 m, between the nearly constant free-tropospheric and in-cloud values for liquid water potential temperature,  $\Theta_{l,top} = 293 \text{ K}$  and  $\Theta_{l,cloud} = 285 \text{ K}$ , and horizontal wind speed  $U_{top} = 11 \text{ m s}^{-1}$  and  $U_{cloud} = 6 \text{ m s}^{-1}$ . It follows that  $\Delta z_{sub}$  directly determines the wind shear ( $\frac{dU}{dz}$ ), atmospheric stability ( $\frac{d\Theta_l}{dz}$ ), and, therefore,  $Ri$ . This dependency is demonstrated in Fig. 4.7 where the two gradients and  $Ri$  are shown to be approximately linear functions of  $\Delta z_{sub}$  (the gradients decreasing and  $Ri$  increasing).

The dependency of  $Ri$  on the square of the wind shear and linearly on temperature gradient (Eq. 2.19) directly leads to the question whether one can estimate a maximum thickness of the TIL: With increasing thickness of the TIL, all gradients decrease and the wind-shear driven turbulence will decrease more rapidly than the decreasing temperature gradient allows turbulence to develop. A maximum thickness  $\Delta z_{max}$  should be reached when  $Ri$  exceeds the critical value of  $Ri_c \approx 1$ . Approximating gradients with finite differences, Eq. 2.19 gives

$$\Delta z_{max} \leq Ri_c \frac{\bar{\Theta}_l}{g} \frac{(\Delta U)^2}{\Delta \Theta_l}, \quad (4.1)$$

where  $\bar{\Theta}_l$  represents the mean value in the TIL and  $\Delta U = U_{top} - U_{cloud}$  and  $\Delta \Theta_l = \Theta_{l,top} - \Theta_{l,cloud}$ . With the measurement results of  $\bar{\Theta}_l = 289 \text{ K}$ ,  $\Delta U = 5 \text{ m s}^{-1}$ , and  $\Delta \Theta_l = 8 \text{ K}$  and an assumed  $Ri_c = 1$ , a maximum thickness of  $\Delta z_{max} \approx 90 \text{ m}$  is estimated. This estimate is consistent with the observed maximum of  $\Delta z_{sub} = 85 \text{ m}$  (profile I in Fig. 4.4).

The corresponding picture of the TIL is illustrated in Fig. 4.8. Figure 4.8a shows the idealised initial situation without the TIL and, therefore, infinite gradients of  $U$

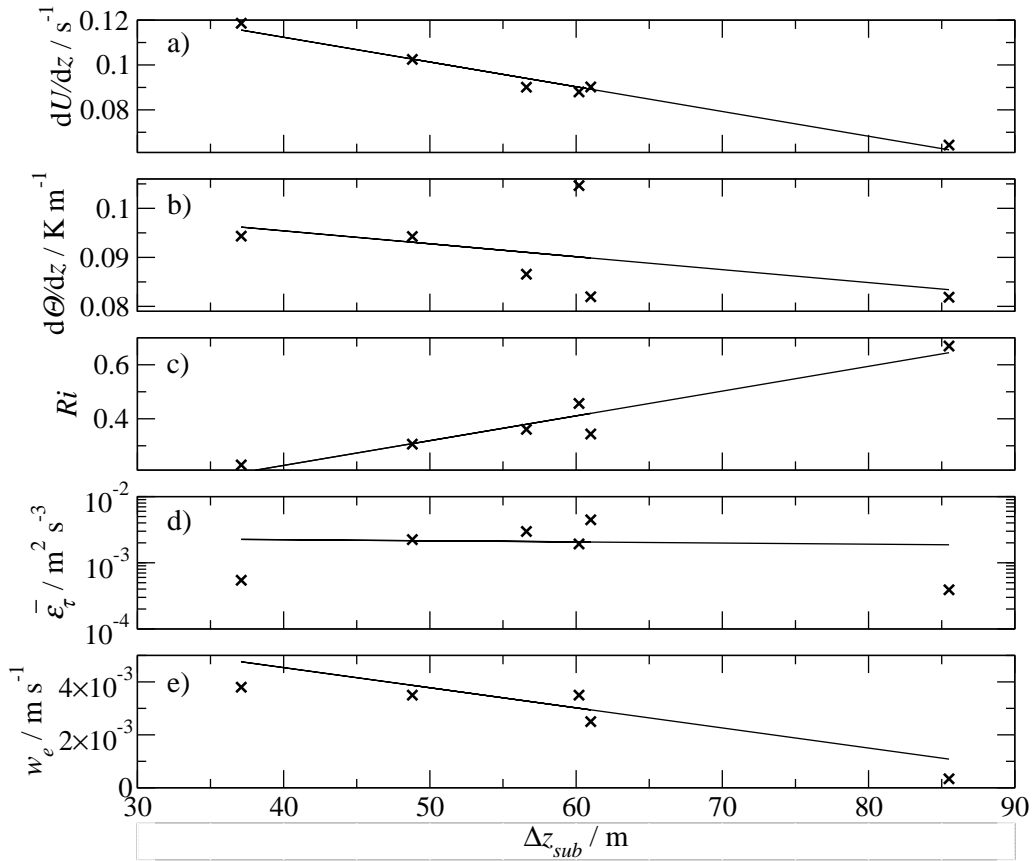


Figure 4.7: Impact of thickness ( $\Delta z_{sub}$ ) of the turbulent inversion layer on its turbulent properties. Dependencies are calculated for: a) horizontal wind shear ( $\frac{dU}{dz}$ ), b) atmospheric stability ( $\frac{d\Theta}{dz}$ ), c) gradient Richardson number ( $Ri$ ), d) averaged local energy dissipation rate ( $\bar{\varepsilon}_\tau$ ) and e) entrainment velocity ( $w_e$ ).

and  $\Theta_t$  at cloud top (*Sc top*) whereas Fig. 4.8b shows the situation after the TIL has developed and the gradients are finite. The layer is assumed to thicken until the critical  $Ri$  is achieved and further turbulent growth of the layer ceases due to decreasing shear. The picture is similar to the classical turbulent mixing layer, but in our situation the fluid below the shear zone is turbulent and that above the shear zone is very weakly turbulent or quiescent. It could be considered the cloud-top analogue of the idealised, spatially-localised shear layer discussed by Smyth and Moum (2000), for which “any initial stratification, however weak, will eventually prevail over the shear and damp the turbulence”. The analogy is not perfect, however, because one half of the layer is constantly turbulent, and we speculate that this is the reason for the continuity of the energy dissipation rate between the cloud layer and the turbulent inversion layer (e.g., see Figs. 4.5 and 4.6). Furthermore, these

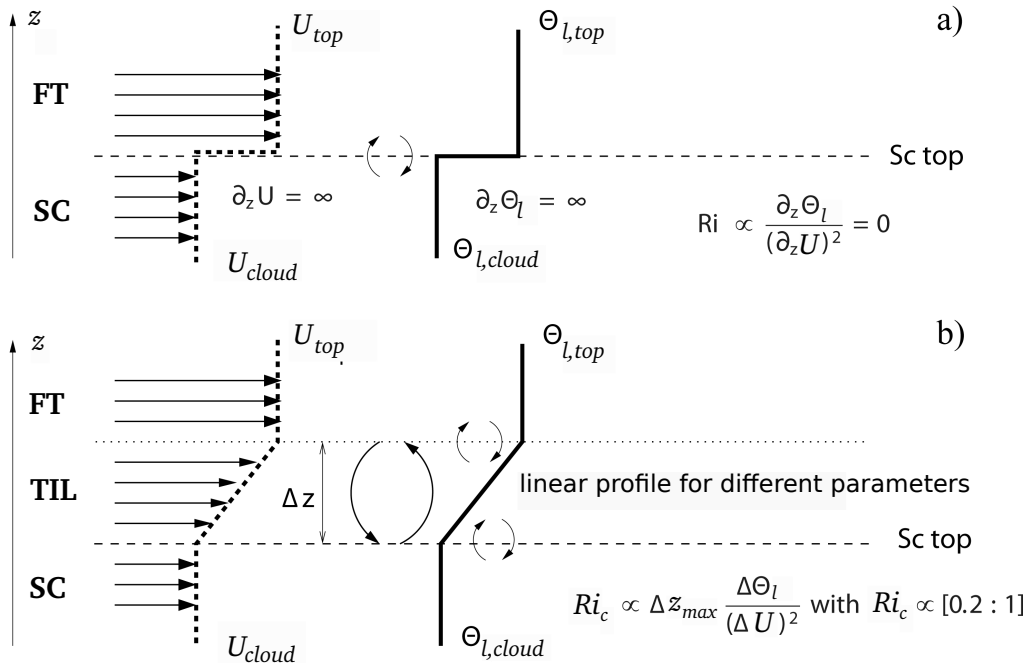


Figure 4.8: Schematic illustration of the development of the cloud top due to entrainment. a) Initial situation: between cloud layer (characterised by  $U_{cloud}$  and  $\Theta_{l,cloud}$ ) and free troposphere (characterised by  $U_{top}$  and  $\Theta_{l,top}$ ) an infinite inversion is located at  $Sc\ top$ . b) Entrainment processes lead to the generation of a turbulent inversion layer within the inversion layer with a maximal thickness of  $\Delta z_{max}$ , which is determined by  $\Delta\Theta_l$ ,  $\Delta U$ , and the gradient Richardson number (see text for more details).

observations and the conceptual picture outlined in Fig. 4.8 are consistent with the LES studies of Brucker and Sarkar (2007) for a turbulent, stratified clear-air mixing layer and of Wang et al. (2008) for a stratocumulus top with strong shear, who both showed monotonic layer growth until  $Ri \approx 0.3$ .

At least semi-quantitatively, the TIL evolution can be further analysed by considering the terms of the balance equation for turbulent kinetic energy (e.g., Brucker and Sarkar, 2007) as mentioned in section 2.1.6. The negligence of the transport term is supported with the logic that there is no strong vertical gradient of  $\bar{\varepsilon}_\tau$  observed. Figure 4.9 shows the magnitude of the production ( $P$ ) and buoyancy ( $B$ ) terms as well as the difference  $P - B$  and the observed mean  $\bar{\varepsilon}_\tau$ . For small  $\Delta z_{sub}$  the energy production due to shear dominates over the suppressing buoyancy, but with increasing  $\Delta z_{sub}$  the rate of increase of turbulent kinetic energy  $dE/dt$  is gradually

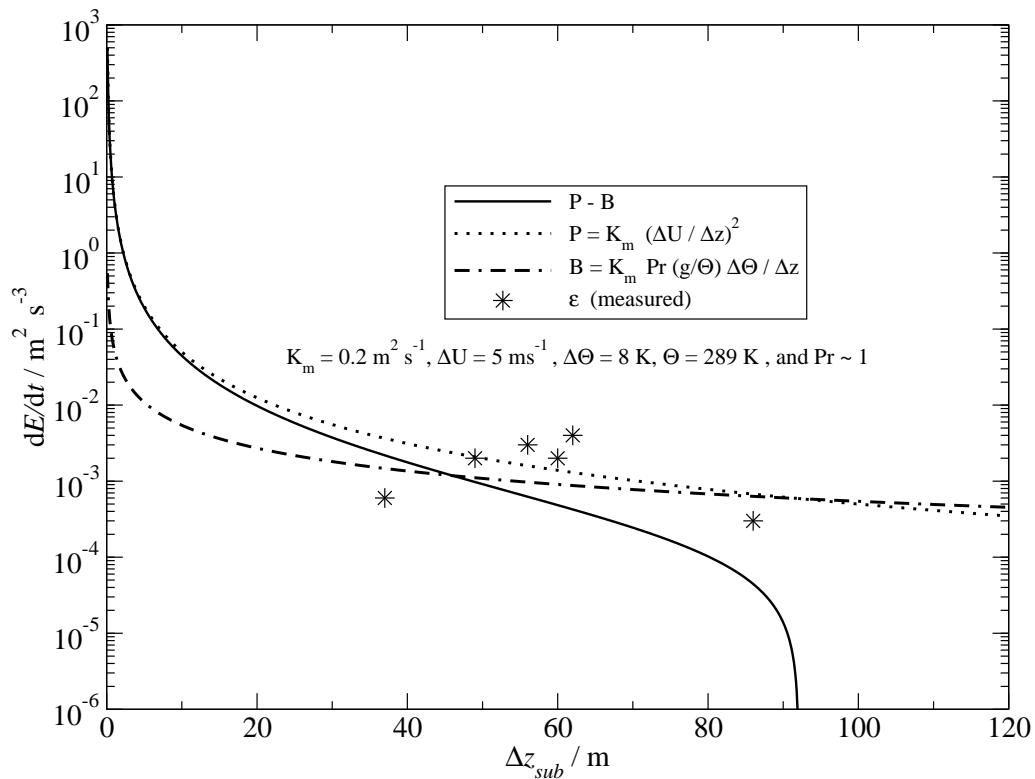


Figure 4.9: Different terms of the turbulent kinetic energy balance equation.  $P$  is the production due to shear,  $B$  is the buoyancy term, and  $\varepsilon$  are observed energy dissipation rates as a function of TIL thickness  $\Delta z_{sub}$ . The values  $K_m$ ,  $\Delta U$ ,  $\Delta\Theta$ , and mean  $\Theta$  are taken from observations and Prandtl number  $Pr \approx 1$  is assumed.

decreasing until a critical value of  $\Delta z$  is reached, beyond which  $P - B$  becomes negative and turbulent kinetic energy is destroyed. Since  $\varepsilon$  is positive definite this is the maximum thickness to which the TIL can develop. For our observations this critical thickness is about 90 m, which corresponds well with the value estimated with the Richardson criterion and the maximum observed thickness (see previous paragraphs).

The influence of stratification on turbulence can be further elucidated by considering relative magnitudes of the large-eddy scale  $l_e$ , the Corrsin scale  $l_c$ , and the Ozmidov scale  $l_o$  (Smyth and Moum, 2000). We find that these length scales are all on the order of 1 m (ranging from approximately 1 to 4 m) and that they do not change significantly or show any clear trend over the measured range of  $\Delta z_{sub}$ . Even within the scatter, however, it is observed that  $l_e > l_o > l_c$ , confirming that the largest



turbulent eddies are strongly influenced by buoyancy, as was initially indicated by the anisotropy in the large-scale velocity fluctuations (e.g., Figs. 4.5 and 4.6). But because  $l_e$  and  $l_o$  are of the same order of magnitude the majority of the turbulent cascade is likely not strongly influenced by buoyancy effects. This is quantified by the ratio between the Ozmidov scale and the Kolmogorov scale ( $l_K = (\nu^3/\varepsilon)^{1/4}$ ) to give a buoyancy Reynolds number ( $Re_B = (l_o/l_K)^{4/3} = \bar{\varepsilon}_\tau/(\nu N^2)$ ), of  $4500 < Re_B < 65000$ . Such values are well beyond the critical value of  $Re_B = 20$  indicated by Smyth and Moum (2000) and indicate a large range of eddy scales unaffected by buoyancy and viscous-dissipation damping effects. Even so, it should be noted that  $l_e \ll \Delta z_{sub}$ , and therefore, the TIL is not thoroughly mixed by eddies of the same scale as the layer thickness, as might be the case for the underlying boundary layer, for example. This may account for the remarkably smooth, linear profiles observed even in instantaneous realisations of the TIL, as shown in Fig. 4.5.

The nearly linear profiles of mean  $\Theta_l$ ,  $a$ ,  $U$ , and  $N$  inside the TIL, e.g., as shown in Figs. 4.5 and 4.6, are consistent with the assumption of constant turbulent diffusion coefficients  $K_m$  and  $K_h$  (for mass and heat, respectively). Therefore, a mean  $K_m$  can be calculated using the mixing-length formulation suggested by Hanna (1968):  $K_m = 0.3 \sigma_w l = 0.3 \sigma_w^4 \bar{\varepsilon}^{-1}$  with the typical large eddy length scale  $l_e = \sigma_w^3/\bar{\varepsilon}$ . For each profile,  $\bar{\varepsilon}_\tau$  is averaged over the TIL to estimate  $\bar{\varepsilon}$ . The standard deviation  $\sigma_w$  has been estimated from individually detrended segments of the profile with an integration length of 6 s each. The length has been chosen to interpret structures with a dimension up to about 12 m as turbulent fluctuations assuming a climbing rate of  $2 \text{ m s}^{-1}$ . Sensitivity tests with different integration lengths lead to a typical uncertainty for  $\sigma_w$  of about 10 %; for one profile a maximum value of 25 % was estimated. The range of the estimated  $l_e$  is 2 to 5 m resulting in a range for  $K_m$  of 0.1 to  $0.3 \text{ m}^2 \text{ s}^{-1}$  for the six profiles.

Using  $K_m$  the entrainment flux can be approximated with the temperature gradient assuming  $K_m \approx K_h$  (e.g., Prandtl number  $\text{Pr} \approx 1$ ):

$\langle w'\Theta' \rangle = -K_h(\partial\Theta/\partial z) = -K_h(\Delta\Theta/\Delta z_{sub})$ . Afterwards, the entrainment velocity can be calculated as  $w_e = (-\langle w'\Theta' \rangle)/\Delta\Theta = K_h/\Delta z_{sub}$ . The resulting entrainment velocities range from about 1 to  $5 \times 10^{-3} \text{ m s}^{-1}$ , comparable for example to the values determined by Faloon et al. (2005) for the stratocumulus-topped marine boundary layer. The dependence of  $\bar{\varepsilon}_\tau$  and  $w_e$  on  $\Delta z_{sub}$  are shown in the two bottom panels of Fig. 4.7. Interestingly, the  $\bar{\varepsilon}$  averaged over the TIL does not show a clear trend with  $\Delta z_{sub}$ . The estimated  $w_e$ , however, hints at a decrease with  $\Delta z_{sub}$ , which is consis-

tent with the LES results of Wang et al. (2008). The decrease can be understood by noting that the entrainment velocity scales as  $w_e \sim \sigma_w(l_e/\Delta z_{sub})$ , and that  $l_e$  and  $\sigma_w$  are observed to be rather constant for the measured profiles. At least in the case of  $l_e$ , the lack of variability is likely due to its consistent collapse to be of the same order as  $l_o$ . If this is the case, it suggests that the ratio  $l_e/\Delta z_{sub}$ , already small, continues to decrease as the TIL thickens and that there is a minimum  $w_e$  corresponding to the maximum layer thickness  $\Delta z_{max}$  (i.e., when the critical Richardson number is reached). Therefore, we can speculate that although the cloud interface is leaky, to use the language of Lenschow et al. (2000), the leakiness decreases as the TIL develops. Furthermore, because  $l_e/\Delta z_{sub} \ll 1$  we can qualitatively state that it likely grows through nibbling rather than engulfment. This effective elimination of direct communication between the cloud layer and the free troposphere may be the cause of the buffer against entrainment instability suggested by Rogers and Telford (1986).

Although, further high-resolution measurements at top of stratocumulus layer performed with a similar flight strategy are necessary, we assume that this large-scale, shear-dominated situation contrasts with the picture of local-scale shear resulting from large-scale convective eddies (e.g., Sullivan et al., 1998; Kurowski et al., 2009). We can speculate that the large-scale convective eddies, in this case are not so important in generating the shear, but possibly in driving vertical undulations that lead to variations in the TIL thickness. For example, one might envision pulsating bursts of turbulence and entrainment as the boundary layer ‘squeezes’ the TIL and therefore sharpens the wind shear gradient. This sharpening would lead, in turn, to a local reduction in  $Ri$ , analogous to that observed by Kurowski et al. (2009) in the weak shear scenario. In this view, while the mean vertical shear of horizontal wind velocity is a property of the large-scale synoptic flow, the local thickness of the TIL itself is still coupled to boundary-layer dynamics, as is the local entrainment rate through its dependence on TIL thickness. One possible indication of such squeezing effect could be the cloud top of profile II in Fig. 4.4 at a height of 1286 m, while the cloud top of the neighbouring profiles is located at a height of 1254 m. Furthermore, the thickness of the TIL of profile II is  $\Delta z_{sub} = 37$  m, while the neighbouring TIL thickness are 85 m respectively 60 m. Clearly, more evidence would be necessary to support or refute this concept. For example, a consistent correlation between cloud top height and TIL thickness could be indicative of a squeezing effect. Robust characterisation of such a correlation would require measurements in an area with large scale homogeneity, coupled with measurements of dynamics within the lower bound-

---

ary layer. Additionally, properties of the TIL, when it is present, are relevant to the evolution of marine stratocumulus through the entrainment process. The TIL exists as a result of shear-induced entrainment of sub-saturated and potentially warmer free-tropospheric air. With increasing thickness of the TIL the air adjacent to the cloud top is increasingly cool and humid, so that local mixing events are less extreme in their thermodynamic properties as illustrated by the arrows indicating the eddies in Fig. 4.8. Thus, we can suppose that the microphysical response to cloud-top entrainment will transition from inhomogeneous to more homogeneous mixing as the mixed air becomes increasingly ‘pre-humidified’ (Lehmann et al., 2009).



# 5 Subsiding shells at the edges of trade wind cumuli

Within the CARRIBA (Clouds, Aerosol, Radiation and tuRbulence in the tRade wInd regime over BAbarδος) campaign, high-resolution measurements of shallow cumulus clouds were performed in the trade wind region. The analysis is aimed to study the impact of lateral entrainment on the fine-scale structure of cloud edge where shear-driven transport of sub-saturated air into the cloud region leads to the development of a subsiding shell. Adjacent to the turbulent and buoyant subsiding shell, a non-turbulent, non-buoyant “secondary shell” with a slight downdraft is observed. In the trade wind region, continuous development of shallow cumuli over the day allows for an analysis of the properties of both shells as a function of different cloud evolution stages. The chapter starts with a brief description of the measurement campaign and the meteorological conditions in the trade wind region, followed by the measurement results.\*

## 5.1 Campaign and Meteorology

The characterisation of the fine-scale structure at the edge of shallow cumuli is based on measurements performed in the framework of the CARRIBA campaign. The campaign took place in the trade wind regime over Barbados in November 2010 and April 2011. Here, only a brief summary of details which are important for the cloud edge analysis is provided. For a more-detailed description of the CARRIBA project the reader is referred to Siebert et al. (2013).

Barbados is the eastern-most Caribbean island (Fig. 5.1a), located at  $13^{\circ} 10' N$  and

---

\*Please note that some parts of the following chapter including Fig. 5.5 to 5.10 and Tab. 5.1 are taken from Katzwinkel et al. (2013) without further notice.



formed. Due to visual flight regulations, the helicopter had to remain above the clouds while ACTOS performed horizontal flight legs within the upper part of the cloud region. Therefore, all cloud measurements were performed 50 – 100 m below cloud top.

## 5.2 Weather conditions

The quite homogeneous meteorological conditions within the trade wind region present during both campaigns are shown in Fig. 5.2. For every flight day, the potential temperature, mixing ratio, horizontal wind velocity and wind direction are averaged within the marine sub-cloud layer (SCL) and plotted over the day of year (doy). During both campaigns,  $\Theta$  shows only small fluctuations, around 301 K during the November campaign and around 299 K during April 2011. The mixing ratio has lower values during the April campaign than in November but shows also quite small fluctuations for the individual campaigns ( $\bar{q} = 17 \text{ g kg}^{-1}$  during November and  $\bar{q} = 15 \text{ g kg}^{-1}$  during April). The horizontal wind velocity within the SCL fluctu-

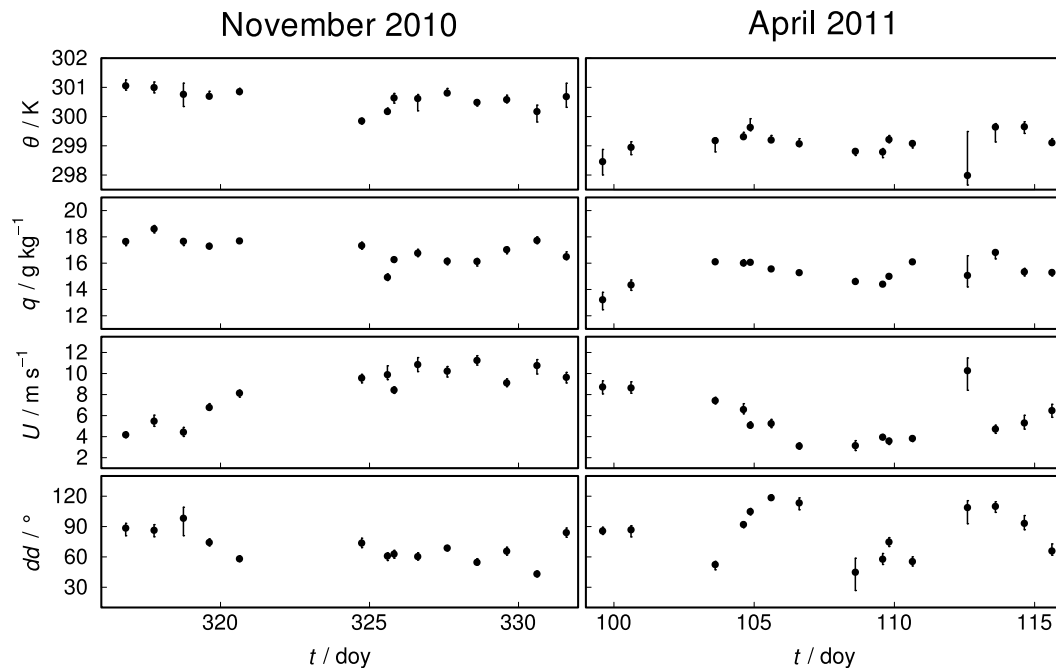


Figure 5.2: Mean meteorological parameters of the marine sub-cloud layer shown for all flights performed during both campaigns. The vertical lines denote the 25th percentile of the data.

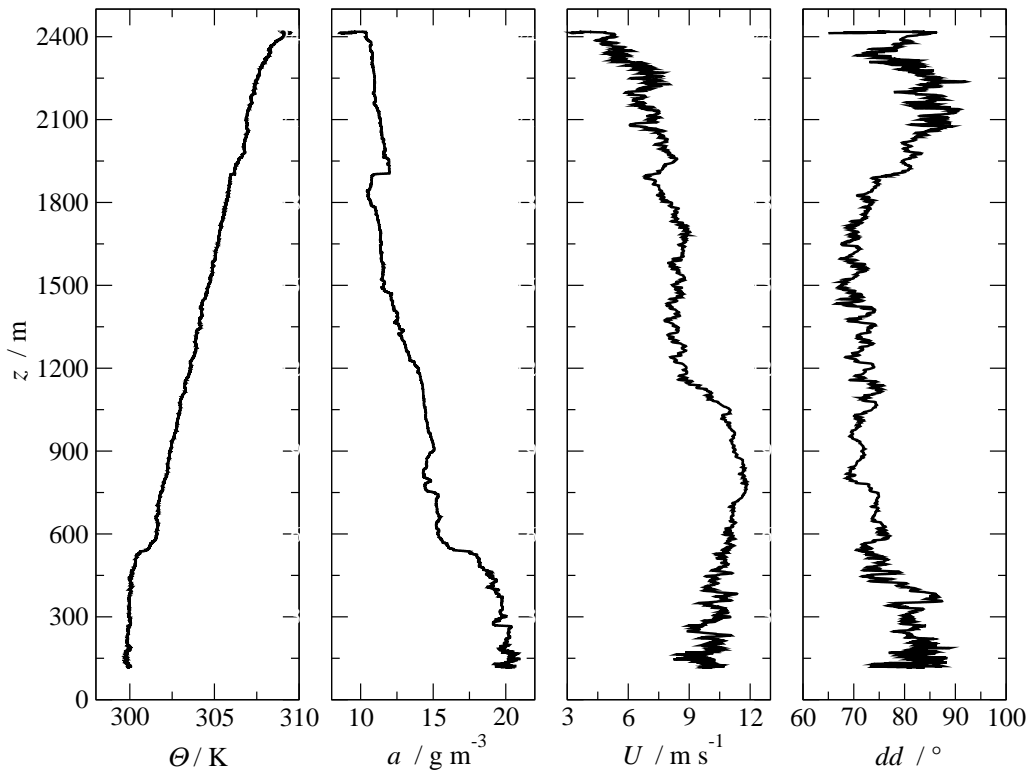


Figure 5.3: Profiles of potential temperature ( $\Theta$ ), absolute humidity ( $a$ ), horizontal wind speed ( $U$ ) and wind direction ( $dd$ ) obtained during the ascent of ACTOS performed on November 20, 2010 starting at 1650 UTC.

ates between  $4 - 12 \text{ m s}^{-1}$  for both campaigns with a direction fluctuating between northeast and southeast.

The vertical stratification within the trade wind region is exemplary illustrated for one ascent in the beginning of the ACTOS flight performed on 20 November, 2010 at 1650 UTC (Fig. 5.3). The well-mixed SCL had a typical thickness of about 500 m and is characterised by  $\Theta = 300 \text{ K}$ ,  $a = 20 \text{ g m}^{-3}$  with a slight decrease to the top of the SCL and  $U = 10 \text{ m s}^{-1}$  coming from east-northeast. Above the thin transition layer at 500 m height characterised by an increase of  $\Theta$  and a decrease of  $a$ , the conditionally unstable cloud layer is characterised by a slight linear increase of  $\Theta$  and a nearly linear decrease of  $a$ . The estimated lapse rate of  $0.5 \text{ K}/100 \text{ m}$  for  $\Theta$  is similar to the observed lapse rate during the BOMEX (Barbados Oceanographic and Meteorological Experiment) campaign (Siebesma et al., 2003). The horizontal wind velocity decreases from  $U \approx 10 \text{ m s}^{-1}$  to  $U \approx 7 \text{ m s}^{-1}$  at a height of 1100 m while the wind direction is constant east-northeast for all heights.

At this day, the shallow cumuli developed near the thin transition layer with a





Figure 5.4: Example of the shallow trade wind cumuli over Barbados. Picture is taken during a research flight along the east coast of Barbados on November 21, 2010.

cloud-base height of 700 m. Generally during both campaigns, the cloud base varied between 300 m and 900 m. Typically, in the trade wind region cumuli of different evolution stages can be found close to each other. Frequently, actively growing clouds were observed adjacent to dissolving ones. This is caused by the continuous development of shallow cumuli over the day based on quite homogeneous conditions in terms of sea surface temperature and mesoscale dynamics. An example of a cloud situation over the island recorded during one flight in November 21, 2010 is shown in Fig. 5.4. In the middle of the picture, dissolving or just developing cumuli are visible, while in front of the picture and on the right side well-developed cumuli are located. The following analysis bases on measurements in such different cloud evolution stages.

## 5.3 Results

### 5.3.1 Concepts and statistical cloud analysis

The analysis of the fine-scale structure of the edges of shallow cumuli starts with the basis for a statistical analysis of the high-resolution measurements within numerous trade-wind cumulus clouds. Based on the observed thermodynamic and

microphysical properties, as well as the turbulent and mean velocity profiles, quantitative criteria are identified for defining the cloud core, cloud shell, and cloud-free environment. Furthermore, because the trade wind environment allows clouds to be sampled at all stages of development, the statistical analysis suggests a natural definition of three evolutionary stages: actively growing, decelerating, and dissolving clouds. For the purpose of a statistical analysis, the following conditions are defined for selecting individual clouds. First, small cloud fragments are excluded from the analysis. This means that the diameter of the cloud and  $LWC$  in the cloud core region have to be larger than 50 m and  $0.2 \text{ g m}^{-3}$ , respectively. Second, two neighbouring clouds have to be sufficiently well-separated from each other so as to define a clear cloud-free environment between subsequent clouds. Therefore, the distance to the next cloud has to be larger than 100 m. 217 cloud cases fulfil these criteria.

For the definition of the different cloud regions the following parameters are used:  $LWC$ , vertical wind velocity  $w$ , buoyancy  $B$ , and local energy dissipation rate  $\varepsilon$ . For the calculation of  $B$  and  $\varepsilon_\tau$ , the reader is referred to sections 2.1.5 and 2.1.4. For  $\varepsilon$  the results of both calculation methods are used within this section, whereby the direct method is calculated using a moving window with a width of 100 samples corresponding to  $\tau \simeq 0.23 \text{ s}$ . Using the hot-wire data, the final smoothed time series of  $\bar{\varepsilon}_\tau$  has a resolution of about 5 cm. The method using the second-order structure function is applied to non-overlapping sub-records of  $\tau = 1 \text{ s}$  getting a resolution of 20 m.

In Figure 5.5 the different cloud regions are illustrated with a specific example taken from a single cloud penetration on November 24, 2010. In this work, we define the cloud core region as the region with  $LWC$  larger than  $0.2 \text{ g m}^{-3}$ . For the specific example in Fig. 5.5, this region is characterised by nearly constant values of  $a = 17 \text{ g m}^{-3}$  and  $T = 21 \text{ }^\circ\text{C}$ ,  $w > 0$  with peak values of up to  $2.5 \text{ m s}^{-1}$ ,  $B > 0$  with an average of about  $0.01 \text{ m s}^{-2}$ , and  $\bar{\varepsilon}_\tau \approx 10^{-3} \text{ m}^2 \text{ s}^{-3}$ . The liquid-water potential temperature  $\Theta_l$  shows a mean value of 289 K. In the cloud-free environment,  $\bar{\varepsilon}_\tau$  and  $a$  decrease to  $10^{-4} \text{ m}^2 \text{ s}^{-3}$  and  $14.5 \text{ g m}^{-3}$ , respectively,  $T$  shows similar values as inside the cloud core region,  $w$  and  $B$  fluctuate around zero and  $\Theta_l = 302 \text{ K}$ .

The cloud edges are marked in Fig. 5.5 by the grey regions located between the cloud-free environment and the cloud core region, adjacent to both sides. These regions are characterised by  $LWC < 0.1 \text{ g m}^{-3}$  with a high variability, illustrating

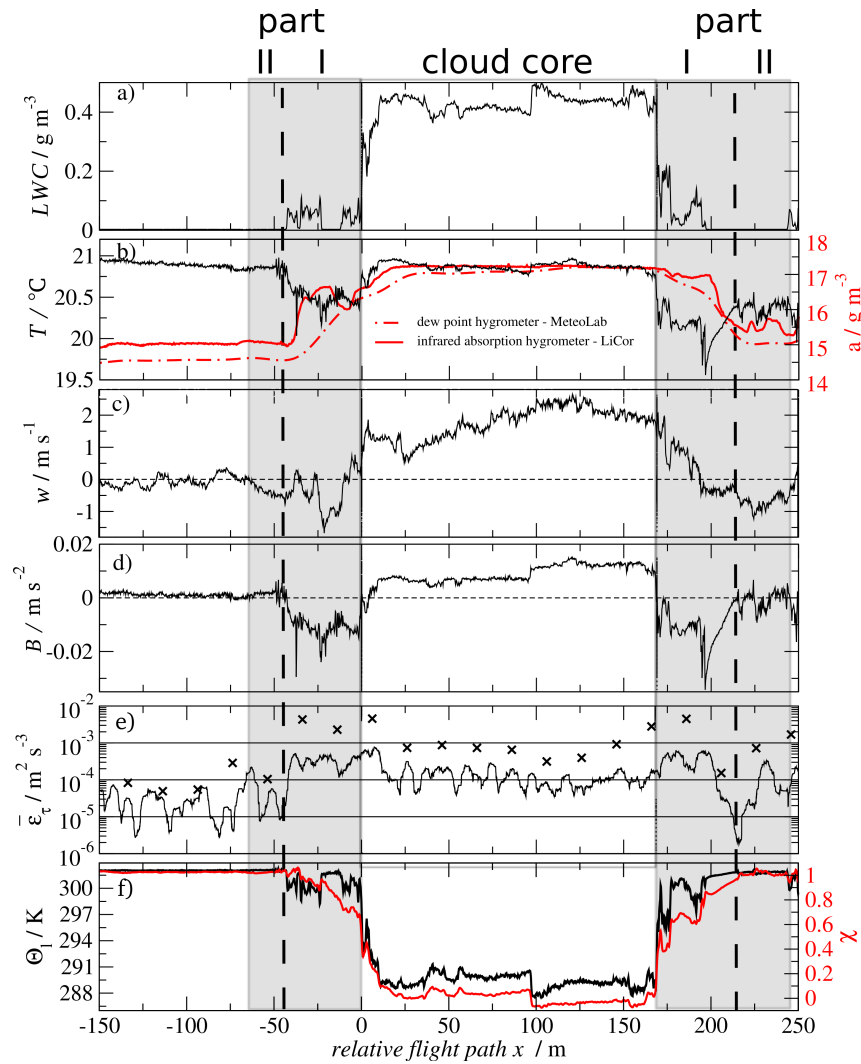


Figure 5.5: A single cloud penetration: a)  $LWC$ , b) temperature ( $T$ ) and absolute humidity ( $a$ ) (whereby the red line denotes measurements with the infrared-absorption hygrometer LiCor and the broken red line marks measurements performed with the dew point hygrometer), c) vertical wind velocity ( $w$ ), d) buoyancy ( $B$ ), e) energy dissipation rate ( $\bar{\epsilon}_\tau$ ) where the black line denotes the direct method and the crosses mark the absolute values calculated based on  $S^{(2)}(t')$  and f) liquid-water potential temperature ( $\Theta_l$ ) and mixing fraction ( $\chi$ ). The white region between the two grey regions marks the cloud core and the two grey regions denote the edges of the cloud. The vertical black dashed line divides the cloud edge into part I, the subsiding shell and part II, the secondary shell.

the eddy-like structure of the cloud edge. A closer look shows that inside this region  $\bar{\epsilon}_\tau$  increases from environmental values to values even higher than in the cloud core

region (black line in Fig. 5.5e). At the same point,  $B$  starts to decrease. Based on these observations, the cloud edge is further divided into two parts (indicated by the vertical dashed black lines). The first part (part I), adjacent to the cloud core region, is characterised by reduced values of  $T$ ,  $w < 0$ ,  $B < 0$  and values of  $\bar{\varepsilon}_\tau \approx 10^{-2} \text{ m}^2 \text{ s}^{-3}$ , again higher compared with the cloud core region. Additionally, the absolute humidity  $a$  increases from environmental values to nearly cloud values within this region. It should be noted, however, that the humidity measurements do not allow a detailed look at the fluctuations due to the significantly reduced spatial resolution. The dew point hygrometer (dotted red line) measures only with a spatial resolution of 20 m and the LiCor (straight red line) was used as a closed system to reduce the cloud droplet impactation. To analyze the humidity fluctuations in this region highly-resolved measurements such as with a Lyman-alpha absorption hygrometer (Zuber and Witt, 1987) would be necessary. The turbulent and humid region at cloud edge is the above-mentioned subsiding shell (Heus and Jonker, 2008). Between the subsiding shell and the environment a second shell is observed, here denoted as part II. This region is characterised by temperature and humidity comparable to the environmental values, a slight downdraft with  $B \approx 0$  and a comparably small  $\bar{\varepsilon}_\tau$ .

The origin of the air within parts I and II of the shell can be investigated by using the liquid-water potential temperature and the total water content. The secondary shell consists mostly of environmental air, which can be seen in Fig. 5.5f by the values of  $\Theta_l$  and mixing fraction  $\chi$  that are similar to the environment values. Here,

$$\chi = (q_t - \bar{q}_{t_c}) / (\bar{q}_{t_e} - \bar{q}_{t_c}), \quad (5.1)$$

where the subscripts “c” and “e” denote the cloud and environmental values, respectively, and the overbar denotes the average value in the corresponding regime. Thereby,  $\chi = 1$  characterises an air parcel consisting of environmental air and  $\chi = 0$  indicates pure cloud air within an air parcel. Hence, the air inside the subsiding shell is a mixture of environmental and cloud air as indicated by the mean value of  $\Theta_l = 299 \text{ K}$  within the shell and the nearly linear decrease of  $\chi$  towards the cloud core region with a minimum value of 0.7. Although, it has been previously assumed that lateral mixing is the leading mechanism for the development of the subsiding shell (Heus and Jonker, 2008), no definite statement about the mixing process can be made based on the data presented here. Evidence for this assumption could be

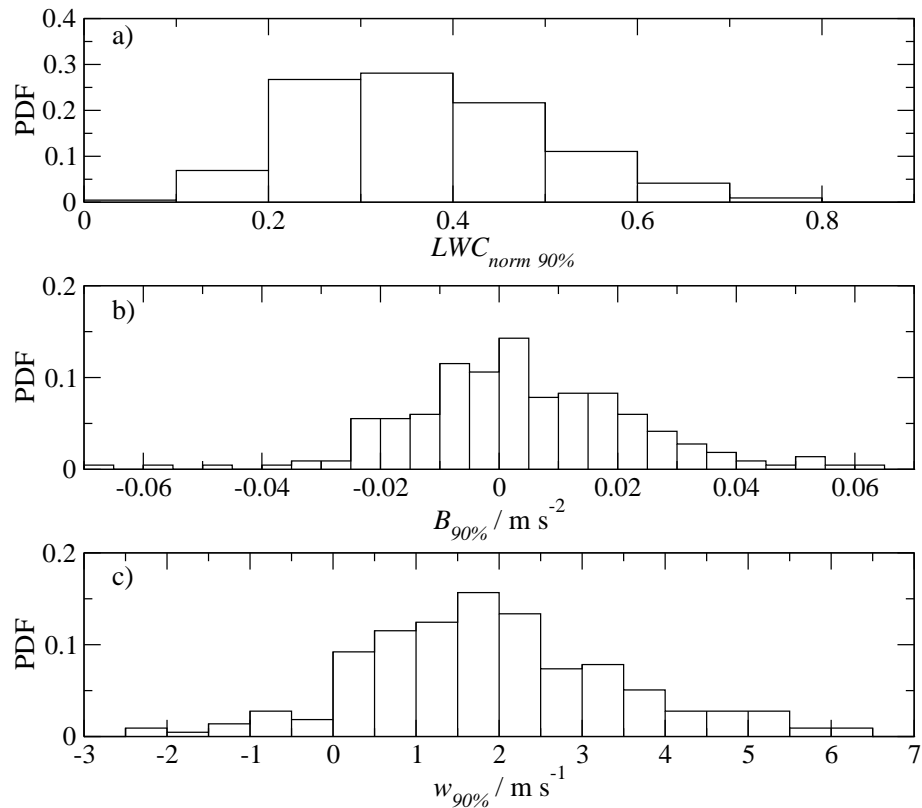


Figure 5.6: The variability of all 217 selected clouds is represented by the probability density functions (PDFs) of the 90th percentile of: a) normalised liquid water content ( $LWC_{norm\ 90\%}$ ), b) buoyancy ( $B_{90\%}$ ), and c) vertical wind velocity ( $w_{90\%}$ ) inside the cloud core region.

the calculated mixing temperature of  $\Theta_{lm} = \chi\Theta_{le} + (1 - \chi)\Theta_{lc} = 289.1\text{ K}$ , which is nearly the same as the observed mean value within the shell. But the mean value of  $\Theta_l$  could also be interpreted as being a result of mixing of cloud air with clear air from above indicated by an estimated lapse rate of  $0.5\text{ K}/100\text{ m}$  for  $\Theta_l$  under cloud-free conditions. In either case, the turbulent mixing of these two air masses leads to an evaporative cooling effect resulting in negatively buoyant air at cloud edge.

Based on the observed properties of continuously developing cumulus clouds in the trade wind region, the selected clouds are divided into three different stages of evolution: a) actively growing, b) decelerated, and c) dissolving clouds. The division is based on the calculation of the 90th percentile of  $B$  ( $B_{90\%}$ ) and  $w$  ( $w_{90\%}$ ) inside the cloud core region of each of the selected clouds. The actively growing clouds are characterised by an updraft and a positive  $B_{90\%}$  ( $w_{90\%} > 0$  and  $B_{90\%} > 0$ ).

In the decelerated phase, the updraft is still observed, while the buoyancy shows negative values inside the cloud core region ( $w_{90\%} > 0$  and  $B_{90\%} < 0$ ). Dissolving clouds are characterised by a downdraft and negative  $B_{90\%}$  inside the cloud core region ( $w_{90\%} < 0$  and  $B_{90\%} < 0$ ). Figure 5.6 shows the probability density functions (PDF) of these parameters including the 90th percentile of the normalised  $LWC$  (normalised with the calculated adiabatic value) ( $LWC_{norm\ 90\%}$ ). In Fig. 5.6a, the distribution of  $LWC_{norm\ 90\%}$  varies in a broad range between 0.1 and 0.8 times the adiabatic-calculated value. The PDF of  $B_{90\%}$  shows positive values, indicating actively growing clouds, and also negative values inside the cloud core region (Fig. 5.6b). Figure 5.6c shows the PDF of  $w_{90\%}$  representing a majority of clouds with an updraft inside the cloud core region. But a few clouds with downdrafts inside the cloud core region are measured, indicating dissolving clouds.

### 5.3.2 Characterisation of cloud edge

In the following, the analysis of the edges – in particular the subsiding and secondary shells (see Fig. 5.5) – of 217 shallow cumulus clouds is presented. Only edges sampled while entering the cloud have been considered to minimise any possible influence of wetting of the temperature probe.

The characterisation of the subsiding shell is based on three main parameters. One parameter is the thickness of the subsiding shell whose calculation is based on the definition by Abma et al. (2013):

$$\delta = \frac{1}{B_{10\%}} \int_{X|_{B_0}}^{X|_{w_0}} B \, dx, \quad (5.2)$$

where  $X|_{B_0}$  and  $X|_{w_0}$  denote the two boundaries of the subsiding shell:  $X|_{B_0}$  characterised by the increase of  $\bar{\varepsilon}_\tau$  from environmental to even higher values compared to the in-cloud values and the decrease of  $B$ , respectively and  $X|_{w_0}$  characterised by the change of  $w$  from downdraft to updraft or the change of  $B$  from negative to positive, respectively. Here, the integral is normalised with the 10th percentile of the buoyancy calculated within the integration limits. The use of the 10th percentile instead of the minimum values as described by Abma et al. (2013) is simply a result of the dependency of the measured minimum value on the measurement resolution. The second and third parameters for characterising the subsiding shell are the 10th

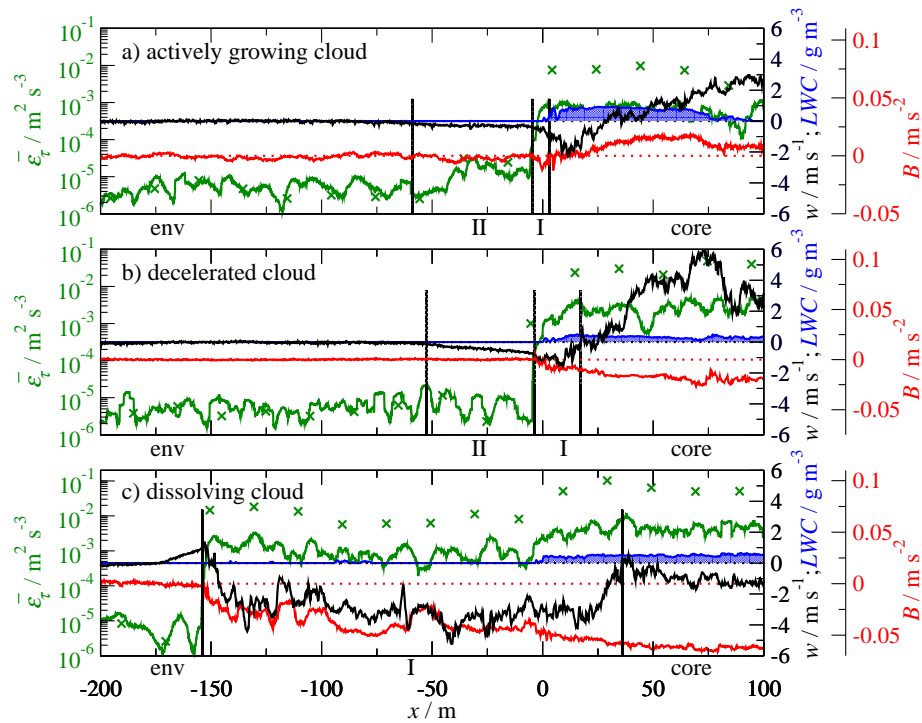


Figure 5.7: Examples of cloud edges for each of the three stages of evolution of the trade wind cumuli: a) actively growing cloud with  $w_{90\%} > 0$  and  $B_{90\%} > 0$ , b) decelerated cloud with  $w_{90\%} > 0$  and  $B_{90\%} < 0$ , and c) dissolving cloud with  $w_{90\%} < 0$  and  $B_{90\%} < 0$ . In all plots, the color code is the same: blue regions mark the liquid water content ( $LWC$ ), black lines denote the vertical wind velocity ( $w$ ), green and red lines mark the energy dissipation rate ( $\bar{\epsilon}_\tau$ ) and the buoyancy ( $B$ ), respectively. The entrance of the cloud core region ( $CE$ ) is denoted by  $x = 0$  m, indicated by  $LWC > 0.2 \text{ g m}^{-3}$ .

percentile of buoyancy, and the 10th percentile of the vertical wind velocity ( $w_{10\%}$ ) calculated also within the integration limits.

Figure 5.7 shows examples of cloud edges for each of the cloud evolution stages, for which the criteria were defined in section 5.3.1. These clouds were measured on November 14, 2010, and April 14 and 16, 2011. The  $x$ -axis shows the distance relative to the entrance of the cloud core region ( $CE$ ). For all cases, 200 m in front of the cloud core region and 100 m of the cloud core region itself are shown. The different regions are marked with vertical black lines and a corresponding identifier (e.g., env as environment). The thickness of the subsiding shell clearly differs in Fig. 5.7

depending on the stages of evolution. In the case of the actively growing cloud,  $\delta$  is about 7 m with  $w_{10\%} = -1.7 \text{ m s}^{-1}$  and  $B_{10\%} = -0.008 \text{ m s}^{-2}$ . Additionally, the secondary shell is apparent with a thickness of 60 m. The decelerated cloud shows a distinct subsiding shell with a broader thickness of about 20 m and a downdraft of  $w_{10\%} = -1.5 \text{ m s}^{-1}$  and  $B_{10\%} = -0.01 \text{ m s}^{-2}$ . Additionally, a smaller thickness of 45 m is observed for the secondary shell. In the case of the dissolving cloud an intense downdraft inside the subsiding shell of  $w_{10\%} = -3.8 \text{ m s}^{-1}$  and  $B_{10\%} = -0.06 \text{ m s}^{-2}$  is observed. The thickness of this shell increases to nearly 170 m, and no secondary shell is observed.

Figure 5.8 shows the PDFs of the characteristic parameters ( $w_{10\%}$ ,  $B_{10\%}$  and  $\delta$ ) of the subsiding shells. The measured 10th percentile of downdraft inside the subsiding shells varies between 0 and  $-5 \text{ m s}^{-1}$  (Fig. 4a). Figure 5.8b shows the PDF of  $B_{10\%}$ , where most of the values lie in the range from 0 to  $-0.02 \text{ m s}^{-2}$ . Additionally, clouds

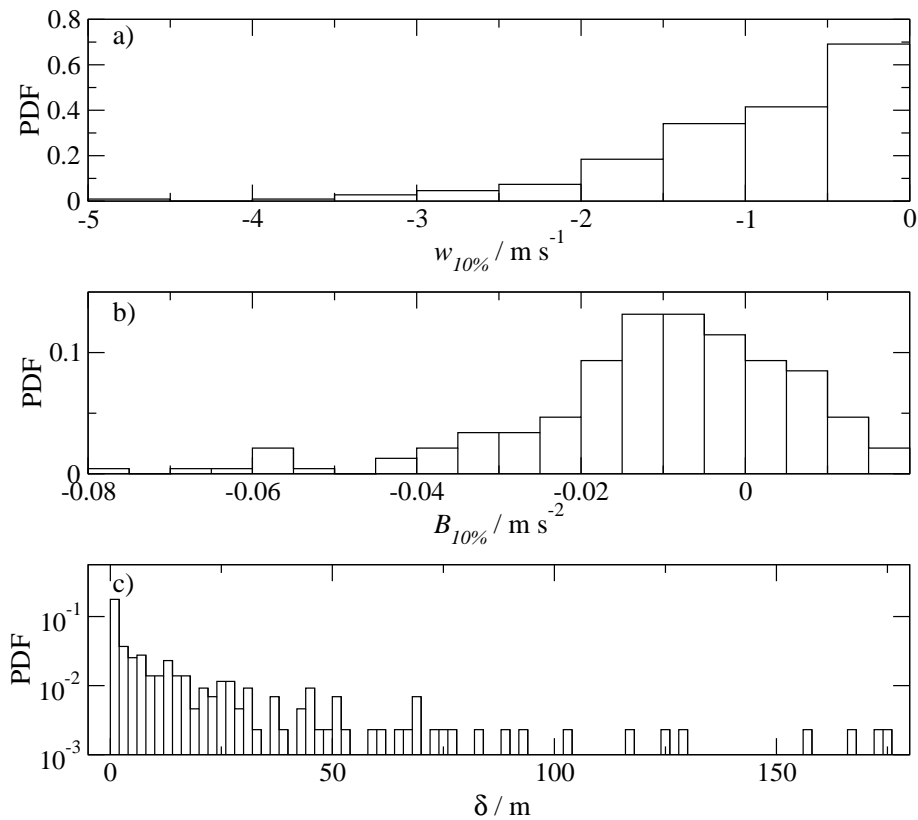


Figure 5.8: Probability density functions of: a) minimum downdraft velocity ( $w_{10\%}$ ), b) minimum buoyancy inside the subsiding shell ( $B_{10\%}$ ), and c) the thickness of the subsiding shell ( $\delta$ ).



	actively growing	decelerated	dissolving
	$w_{90\%} > 0$	$w_{90\%} > 0$	$w_{90\%} < 0$
	$B_{90\%} > 0$	$B_{90\%} < 0$	$B_{90\%} < 0$
$n$	122	79	14
$w_{90\%} / \text{m s}^{-1}$	2.2	1.6	-0.8
$w_{10\%} / \text{m s}^{-1}$	-0.3	-1.0	-1.9
$B_{10\%} / \text{m s}^{-2}$	-0.002	-0.016	-0.033
$\Delta(X  _{w_0} - CE) / \text{m}$	6	12	76
$\delta / \text{m}$	2	16	82
$cd / \text{m}$	178	120	82
$\Delta(CM - X  _{B_0}) / \text{m}$	99	82	96
$f / \%$	82	70	45
$\delta_d / \text{m}$	68	47	6
$w_d / \text{m s}^{-1}$	-0.32	-0.25	-0.45

Table 5.1: The table summarises median properties of all selected clouds for each stage of evolution. These properties are: 90th percentile of  $w$  inside the cloud core region ( $w_{90\%}$ ), 10th percentile of the downdraft velocity ( $w_{10\%}$ ) and the buoyancy ( $B_{10\%}$ ) inside the subsiding shell, distance between the boundary of the subsiding shell close to the cloud core region  $X |_{w_0}$  and  $CE$  ( $\Delta(X |_{w_0} - CE)$ ), the thickness of the subsiding shell ( $\delta$ ), cloud diameter ( $cd$ ), distance between the cloud-free boundary of the subsiding shell ( $X |_{B_0}$ ) and the middle of the cloud core region ( $CM$ ) ( $\Delta(CM - X |_{B_0})$ ), the relative frequency of the secondary shell ( $f$ ), median thickness of the secondary shell ( $\delta_d$ ), and median downdraft velocity ( $w_d$ ) inside the secondary shell.

with a positive buoyancy are observed and also a few clouds show a very strong negative buoyancy as low as  $-0.08 \text{ m s}^{-2}$ . The PDF of  $\delta$  is shown in Fig. 5.8c, where the y-axis is logarithmic for better clarity. The values vary between below 1 m and up to 175 m with only a few values observed with  $\delta > 80 \text{ m}$ .

Table 5.1 summarises the median properties of cloud edge and cloud core region as a

function of the evolution stages. All parameters were first calculated for individual clouds and afterwards averaged giving one median value for each evolution stage. The number of clouds grouped in the different evolution stages is given by  $n$ . The majority of the observed clouds were actively growing, thus only a few dissolving clouds are considered. This is a result of the stringent criteria for cloud selection. Most of the dissolving clouds are rejected due to their low values of  $LWC$  or the narrow cloud diameter. With the evolution from an actively growing cloud to a dissolving one,  $w_{90\%}$  decreases from  $2.2 \text{ m s}^{-1}$  to a downdraft of  $-0.8 \text{ m s}^{-1}$ , while within the subsiding shell, an increase in the absolute values of  $w_{10\%}$  and  $B_{10\%}$  is observed. Furthermore, the cloud boundary of the subsiding shell shifts more and more into the cloud core region, which is indicated by an increasing distance between  $CE$  and  $X|_{w_0}$  ( $\Delta(X|_{w_0} - CE)$ ). The mixing process and evaporation of cloud droplets therefore leads to an increasing thickness of the subsiding shell  $\delta$ , while the cloud diameter decreases. A nearly constant distance between the cloud-free boundary ( $X|_{B_0}$ ) of the subsiding shell and the middle of the cloud core region ( $CM$ ) at around 90 m (marked with  $\Delta(CM - X|_{B_0})$ ) supports the results of Abma et al. (2013) that the subsiding shell expands primarily into the cloud core region. The next three parameters deal with the behavior of the secondary shell as a function of the evolution stages of the cumuli. The secondary shell is observed at the edge of actively growing clouds with a relative frequency of 82%, but also half of the dissolving clouds are surrounded by such a shell. With the evolution from an actively growing cloud to a dissolving one, the median thickness of the secondary shell  $\delta_d$  decreases, while the downdraft inside this shell fluctuates around  $w_d \sim -0.3 \text{ m s}^{-1}$  for all stages of evolution.

### 5.3.3 Comparison with model results

In this section, the consistency of our statistical results is explored with the direct numerical simulations (DNS) by Abma et al. (2013). A brief description of the model is given here, for further details the reader is referred to Abma et al. (2013). DNS fully resolves turbulence down to dissipation scales, sacrificing instead the large eddy structure through an idealised setup. Furthermore, approximations are made in the treatment of cloud microphysics. To simulate the lateral entrainment process at the side of a single shallow cumulus, the model is based on a two-layer system including an environmental and a cloud region that are well-separated. Both regions are characterised by zero vertical wind velocity and zero buoyancy. Therefore, in

contrast to our measurements no compensation flow exists at cloud edge. A broadband perturbation initiates the mixing between the sub-saturated environmental air and the cloudy air. The subsequent evaporation of droplets leads to a cooling effect resulting in negatively buoyant air at cloud edge. This initiates the development of the subsiding shell. With increasing time the simulated subsiding shell grows due to further turbulent mixing between the environmental and cloudy air. The DNS results show a quadratic growth in thickness of the subsiding shell and a linear increase of the downdraft velocity. Based on self-similarity arguments these findings can be described by the following equations (Abma et al., 2013):

$$\delta_m(t_m) = (c_1 c_2 \frac{B_m}{2})(t_m - t_{m1})^2 + \sqrt{2c_1 c_2 B_m \delta_{m1}}(t_m - t_{m1}) + \delta_{m1}, \quad (5.3)$$

$$w_m = \sqrt{2 \frac{c_1}{c_2} B_m \delta_m}. \quad (5.4)$$

Here,  $\delta_m$  is the thickness of the simulated subsiding shell and  $B_m$  and  $w_m$  denote the minimum values of buoyancy and vertical wind velocity within the simulated subsiding shell. According to the simulation of Abma et al. (2013), the initial condition  $t_{m1}$  and  $\delta_{m1}$  are set to 5 s and 0.054 m, respectively, and the constants  $c_1$  and  $c_2$  are determined to be 0.24 and 0.1.

The basis for the comparison of measurements and the simulation is given by the main properties of the subsiding shell:  $\delta$ ,  $w_{10\%}$  and  $B_{10\%}$  for measurements and  $\delta_m$ ,  $w_m$  and  $B_m$  for the simulated subsiding shell. While the measurements are performed at the edges of numerous clouds in different stages of evolution, the simulation considers one single cloud edge and the evolution of the corresponding subsiding shell. This evolution is calculated every 10 s according to Eq. 4 and 5, and it was observed that the value of  $B_m$  increases linearly until reaching a typical value of  $0.02 \text{ m}^2 \text{ s}^{-1}$  during the first 30 s, and remains constant afterwards. Consistent with the latter stages of the simulation,  $B_m$  is taken as a constant for the subsequent comparison with data.

Figure 5.9 shows the correlation between downdraft intensity and thickness of the subsiding shell (Fig. 5.9a) and between downdraft intensity and buoyancy (Fig. 5.9b).

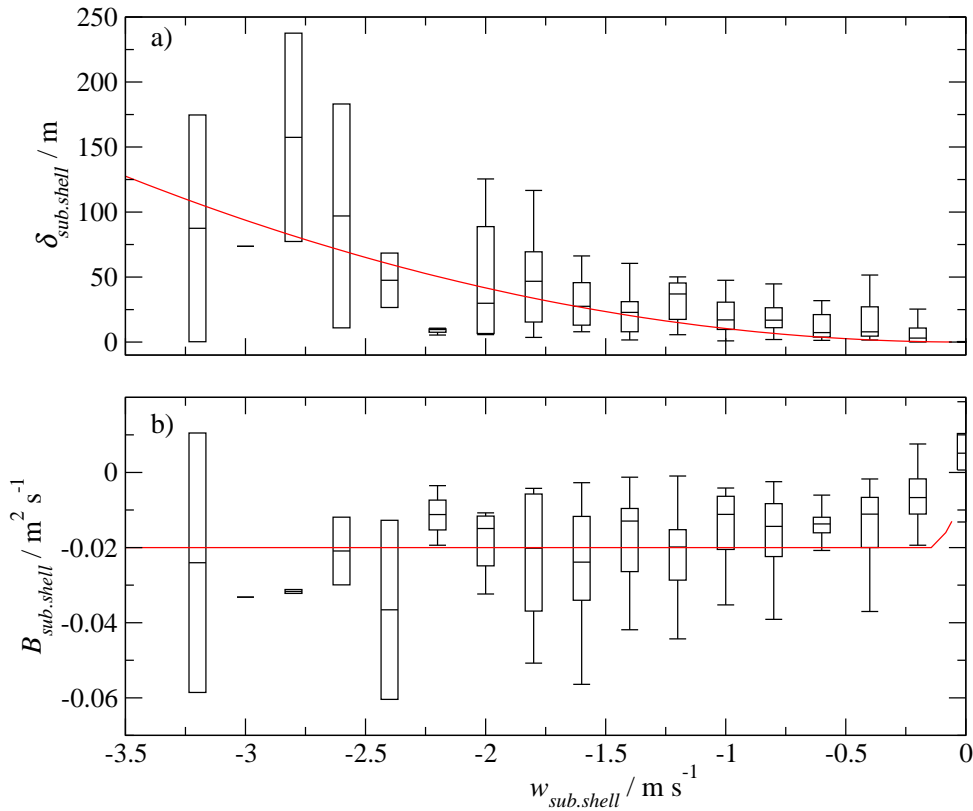


Figure 5.9: Comparison of the measured ( $\delta$ ,  $w_{10\%}$ ,  $B_{10\%}$ ) and simulated ( $\delta_m$ ,  $w_m$ ,  $B_m$ ) properties of the subsiding shell: a) thickness of the subsiding shell is plotted versus the downdraft velocity in the subsiding shell and b) buoyancy is plotted versus the downdraft velocity in the subsiding shell. The red lines represent the model values and the measurements are shown by the boxes.

All correlations are plotted for the simulated subsiding shell (red lines) and for the measured values (boxes). The horizontal line in the middle of the boxes denote the respective median value, the upper and lower boundaries of the boxes mark the 75th and 25th percentile, respectively and the error bars denote the 95th and 5th percentile. In Figure 5.9a, the simulation shows a quadratic dependence of  $\delta_m$  on  $w_m$ . The measured  $\delta$  also increase with decreasing  $w_{10\%}$ , but the measurement uncertainty does not allow for a definitive statement about linear, quadratic, or any other behaviour. The decreasing number of measured values with increasing downdraft intensity leads to an increasing statistical uncertainty that makes rigorous conclusions difficult. Nevertheless, the measurements are in the range of the model prediction and a similar tendency and absolute values are observed. A similar behaviour is seen for the correlations shown in Fig. 5.9b. After the first seconds, the simulated

value  $B_m$  remains constant with increasing downdraft intensity. The same tendency is evident in the measurements despite their relatively large spread.

## 5.4 Summary and Discussion

The ACTOS observations over Barbados provide a detailed insight into the edges of trade wind cumuli. The cloud edges were characterised by highly increased turbulence compared to the cloud-free environment but also compared to the cloud core region which is an indication for strong mixing. The key finding was a well-pronounced subsiding shell which was observed in all of the 217 analyzed clouds. The width and the downdraft velocity of these shells were found to depend on the evolution stage of the clouds, which was defined by cloud core region parameters such as buoyancy and updraft velocity. The findings are illustrated in Fig. 5.10 for three typical cloud evolution stages defined as (from left to right): i) an actively growing cloud defined by positive buoyancy resulting in updrafts ( $B > 0$  and  $w > 0$ ) in the cloud core region, ii) a decelerated cloud type with negative buoyancy ( $B < 0$ ) but still updrafts with reduced magnitude ( $w > 0$ ), and finally iii) a dissolving cloud with negative buoyancy resulting in downdrafts ( $B < 0$  and  $w < 0$ ). Due to flight restrictions the helicopter had to remain above the clouds, therefore, all measurements were performed within 100 m of cloud top as illustrated by the red horizontal line (see Fig. 5.10). Therefore, the measured cloud diameter (80–100 m) is probably smaller compared to a typical cloud diameter as observed in the middle part of a cloud, but the LES results of Heus and Jonker (2008) indicate that our results can be probably extended to lower regions of the cloud.

The measured actively growing clouds (Fig. 5.10-i) are characterised by a comparably broad cloud core region ( $cd$ ) with strong updrafts and are surrounded by a thin subsiding shell ( $\delta$ ). With the evolution to decelerated clouds (Fig. 5.10-ii), the sub-saturated environmental air is mixed deeper into the cloud core region and the subsiding shell grows at the expense of the cloud core region. The width of the entire cloud including shells and cloud core region ( $sb$ ) was observed to remain nearly constant. Evaporative cooling due to lateral entrainment enhances the downdrafts inside the subsiding shell, while the updrafts inside the cloud core region are decelerated due to negative buoyancy. In the dissolving stage of the cloud lifetime (Fig. 5.10-iii), the width and the downdraft velocity of the subsiding shell increase further while the cloud core region is shrinking.

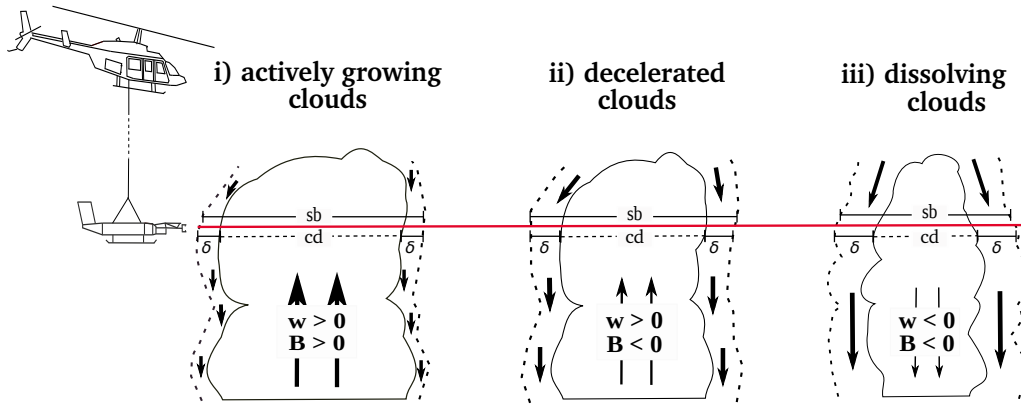


Figure 5.10: Schematic picture of the evolution of a cumulus cloud from actively growing to dissolving, where the growth of the subsiding shell at the expense of the cloud core region is illustrated. Here,  $\delta$  marks the distance from beginning of the subsiding shell to the entrance of the cloud core region, the thickness of the cloud core region is marked with  $cd$  and  $sb$  marks the thickness of the whole system.

The qualitative agreement of the observed correlations between downdraft intensity, width, and buoyancy of the subsiding shell with results gained from DNS by Abma et al. (2013) help to corroborate the existence of a functional relationship between shell properties and cloud evolution stage. The time evolution of  $\delta_m$  in the DNS (cf. Eq. 4) allows an estimate of the evolution time of the measured subsiding shell. For example, if one considers an observed downdraft velocity of  $w_{10\%} = -3.2 \text{ m s}^{-1}$  and the corresponding shell thickness of  $\delta = 100 \text{ m}$  (cf. Fig. 5a), with the help of Eq. 4 and 5 this data point can be related to a model evolution time of  $t = 670 \text{ s}$ . But one must keep in mind that this model evolution time starts after the duration of the spin-up phase (see paper reference) and so does not represent a real cloud age. Additionally, the model ignores any large-scale cloud dynamics, making an interpretation of this time even more difficult. However, this rough estimate provides some idea for future research as how to estimate lifetime of an observed cloud as a function of shell width.

The presented observations of the subsiding shell are also in good agreement with results derived from LES of an unsaturated convective mixed region around a liquid water cloud (Zhao and Austin, 2005a,b). The dimensions of their modeled trade wind cumuli are comparable to the presented observations. The unsaturated convective mixed region in the LES is first smaller than the liquid water cloud and grows in thickness with the evolution of the cloud. It contains roughly half of the

liquid water cloud volume when the cloud top reaches its maximum height. This is of the same magnitude as the relation between the measured cloud core region and the subsiding shell thickness. The unsaturated convective mixed region reaches its maximum thickness shortly before the liquid water cloud is completely evaporated.

In addition to the subsiding shell, the presented observations show also a non-turbulent and neutrally-buoyant shell, here called a secondary shell. This secondary shell connects the laminar environment with the subsiding shell and is observed for every cloud evolution stage (active, decelerated and dissolving). With the evolution of the clouds, the minimum downdraft velocity (10th percentile) remains almost constant inside the secondary shell while the width of this shell decreases.

In the case of an actively growing cloud, the air flow inside this secondary shell might be explained as a compensating flow due to the strong updrafts inside the cloud core region. This picture is supported by the analysis of Heus and Jonker (2008), who pointed out that 10% of the upward mass flux in the cloud core region is compensated in the region with  $B < 0$  while another 13% is compensated by being dragged along downward with the subsiding shell. A more detailed analysis of the mass-flux compensation by Jonker et al. (2008) leads to the conclusion that "... the compensating downward mass-flux takes place in the immediate proximity of clouds and not in the form of a weak uniformly subsiding motion".

The subsiding and secondary shells are also observed in the stage of dissolving clouds, so it follows that there must be a mechanism that still results in downward motion although the upward mass-flux in the cloud core region is reduced. The details of the driving forces of the secondary shell are not fully understood yet, but the observations provide the basis for some further speculations. One possibility for the driving force of the secondary flow is that the air adjacent to the subsiding shell could be dragged along with the downdrafts inside the subsiding shell through lateral turbulent transport of vertical momentum. Another idea is based on observations by Abma et al. (2013), who showed that the minima of the buoyancy and of the vertical velocity fields in the subsiding shell move towards the cloud core region with different speed: the buoyancy minimum moves faster toward the cloud core region compared with the velocity minimum. However, neither explanation is easily reconciled with the observation that the secondary shell is nearly non-turbulent. Finally, one might also speculate that the secondary shell could be the very diluted remnants of a previous subsiding shell that is so diluted that the properties are close

to the environment and the turbulent kinetic energy has almost dissipated, but in which the air is still subsiding due to inertia. The current measurements do not necessarily favor any of these possible mechanisms, so further investigations of the secondary shell are needed.



## 6 Summary

Within the scope of this thesis one of the most important small-scale processes at cloud edge is studied, the entrainment process. The transport of sub-saturated environmental air into the cloud region followed by subsequent mixing with cloudy air leads to negatively buoyant air at cloud edge (buoyancy reversal). The resulting impact on the cloud structure and dynamics is analysed for two different types of the entrainment process: i) cloud-top entrainment at top of a stratocumulus cloud layer and, ii) lateral entrainment at the edges of shallow trade wind cumuli. The underlying measurements were performed with the helicopter-borne measurement payload ACTOS. Its low true airspeed of  $20 \text{ m s}^{-1}$  combined with a high sampling frequency of 100 Hz enables a spatial resolution down to decimeter scale and allows a detailed analysis of the edges of both cloud types. In both cases, the cloud edge is characterised by a strong wind shear driving the turbulent entrainment process and initiating the development of a turbulent mixing region at cloud edge. The main results and conclusions for both cloud types are summarised and the two turbulent mixing regions are compared in the following.

Based on the observations of a stratocumulus layer, the shear-induced entrainment process and subsequent mixing with cloudy air initiates the development of a turbulent inversion layer (TIL) at cloud top. This region connects the turbulent cloud layer with the non-turbulent free troposphere and shows a nearly linear transition from in-cloud values to free-tropospheric values in terms of potential temperature, absolute humidity, horizontal wind velocity, and number concentration of interstitial aerosol particles. The TIL is turbulent, with an energy dissipation rate similar to the observed value of the lower cloud region indicating a coupling between these two layers. However, the two layers differ concerning local isotropy, whereby the TIL shows increasingly two-dimensional turbulence.

The characterisation of the TIL has been observed using a porpoise-dive sampling strategy, whereby ACTOS performed several subsequent profiles around cloud top.

In that way, the upper cloud layer, TIL, and free troposphere are traversed six times. Thereby, the thickness of the TIL has been observed to vary between 37 and 85 m, whereas the potential temperature and horizontal wind speed differences at the top and bottom of the layer remain essentially constant. The Richardson number therefore increases with increasing layer thickness, from approximately 0.2 to 0.7, suggesting that the layer develops to the point where the stable stratification dominates over the turbulence production due to shear and, therefore, turbulence decreases. This indication of a maximum thickness of the turbulent inversion layer is supported by two estimations using on the one hand the critical Richardson number of unity and on the other hand the balance equation for turbulent kinetic energy. In both cases, the estimated thickness is on the order of the measured maximum thickness of  $\approx 90$  m. It is further observed that the large eddy scale is limited by this stable stratification and is on the order of the Ozmidov scale, much less than the thickness of the turbulent inversion layer. Therefore, direct mixing between the cloud top and the free troposphere is inhibited, and the entrainment velocity tends to decrease with increasing TIL thickness. Qualitatively, the TIL likely grows through nibbling rather than engulfment.

Large-scale convective eddies are assumed to be important in driving the vertical undulations that lead to variations in the thickness of the TIL. For example, one might envisage pulsating bursts of turbulence and entrainment as the boundary layer “squeezes” the TIL and, therefore, sharpens the wind-shear gradient. Hence, the local thickness of the TIL itself is still coupled to boundary-layer dynamics, as is the local entrainment rate through its dependence on TIL thickness.

Shear-induced lateral entrainment at the edges of trade wind cumuli is caused by strong updrafts inside the cloud core region and mass-compensating downdrafts at cloud edge. Subsequent mixing between sub-saturated environmental and cloudy air leads to the evaporation of cloud droplets and the following cooling effect initiates an additional buoyant downdraft at cloud edge. So, the already existing mass-compensating downdrafts are intensified and the development of the turbulent, buoyant subsiding shell at cloud edge is initiated. Adjacent to the subsiding shell, a non-buoyant and non-turbulent secondary shell with a slight downdraft is observed which connects the quiescent environment with the turbulent subsiding shell. The analysis of both shells is based on horizontal flight legs performed  $\approx 100$  m below cloud top due to the visual flight regulations valid for the helicopter. The flight legs performed within the upper part of the cloud region may result in a reduced

---

observed cloud diameter (80 – 100 m) compared to a cloud diameter as observed in the middle part of a cumulus cloud.

The nearly steady-state conditions within the trade wind region allows for measurements of 217 trade wind cumuli of different lifetimes and enables the analysis of both shells depending on different cloud evolution stages (actively growing, decelerated and dissolving clouds). Within this thesis, the cloud stages are defined using the sign of mean vertical wind velocity and buoyancy in the cloud core region. The observed actively growing clouds are characterised by a broad cloud core region with positive buoyancy and updrafts and are surrounded by a small subsiding shell. Within the observed evolution from an actively growing to a dissolving cloud, the sub-saturated environmental air is mixed increasingly deeper into the cloud core region and the subsiding shell grows at the expense of the cloud core region. Hence, the observed dissolving clouds, characterised by a negative buoyancy and weak downdrafts within the small cloud core region, are surrounded by a relative broad subsiding shell with comparable strong downdrafts. The qualitative agreement of the measurement results with results gained from direct numerical simulation for the temporal evolution of one single subsiding shell corroborates the assumption of a functional relationship between shell properties and cloud evolution stage. This relationship might be the basis for further research on the question of how to estimate the life time of an observed cloud as a function of shell width.

The laminar secondary shell might be explained as a mass-compensational flow for actively growing clouds. With evolution of the cumuli, the secondary shell shows a decrease in size, while the intensity of the downdraft is nearly constant. This indicates, that beside the mass-compensation additional mechanisms are present that still result in downward motion although the upward mass-flux in the cloud core region is reduced. The discussion in section 5 offers different possible explanations for the downdrafts within this shell: i) the air inside the secondary shell could be dragged along with the downdraft of the subsiding shell, ii) the secondary shell could be caused due to a shift between buoyancy and downdraft region, or iii) the secondary shell is a strongly diluted remnant of a previous subsiding shell. Neither of the first two explanations is easily reconciled with the observation that the secondary shell is nearly laminar. Nevertheless, the results presented in this thesis do not support any of the hypothesised mechanisms and further work is needed to understand the details of this phenomenon.

Both layers, the turbulent inversion layer at top of a stratocumulus cloud and the

subsiding shell at the edges of shallow trade wind cumuli are highly relevant for the evolution of the respective cloud type through the entrainment process. Shear-induced entrainment of sub-saturated environmental air initiates the development of these turbulent layers and with increasing thickness of both layers the air adjacent to the cloud region is getting colder and moister. Therefore, the region around the clouds is pre-conditioned and the entrained air might be almost saturated. This means that turbulent mixing can be considered as a dilution process because droplets do not evaporate in the mixed air (Gerber et al., 2008b) and only the number concentration is reduced.

In spite of the similarities, both layers differ concerning their turbulent structure and the way turbulent kinetic energy is produced. In the case of the stratocumulus layer, the turbulent inversion layer resembles the picture of a classical shear layer (e.g., Smyth and Moum, 2000). As the mixing between the two fluid regions develops, the mixed region becomes thicker and the reduced gradients result in a monotonic decrease of turbulence intensity. In contrast, in the case of the subsiding shell, the initial shear is caused by strong updrafts in the cloud core with mass-compensating downdrafts at cloud edge as observed in actively growing clouds. This strong shear initiates lateral entrainment and subsequent mixing of sub-saturated environmental with cloudy air leading to negatively buoyant air at cloud edge. The latter increases the downdrafts, which in turn leads to an increase of shear and a resulting amplification of turbulent mixing. A possible result could be an even stronger entrainment, so at least for a time, there is a positive feedback with mixing inducing further mixing. Here, only speculations about the mechanism are possible but this seems to be a fascinating twist on the well-studied problem of turbulent shear layers which hamper the determination of cause and effect.

# List of Figures

1.1	Overview of physical processes occurring within and at the edge of a stratocumulus cloud. Thereby, $SW$ and $LW$ denote the short- and longwave radiation fluxes. . . . .	6
1.2	Overview of physical processes occurring within and at the edge of a cumulus cloud. . . . .	9
2.1	Example of a turbulent flow behind two identical cylinders. The picture is taken from Frisch and Kolmogorov (1995). . . . .	12
2.2	Energy cascade with the largest and smallest scales of eddies $l_o$ and $\eta$ modified picture based on Frisch, 1995 . . . . .	14
2.3	The picture shows the turbulent structure at cloud edge, whereby the white arrows illustrate eddies of different size. . . . .	23
2.4	Stratification of a cloud-topped well-mixed boundary layer and the overlying free troposphere: vertical profiles of total water mixing ratio $q_t$ , liquid water mixing ratio $q_l$ , liquid potential temperature $\Theta_l$ , virtual potential temperature $\Theta_v$ , horizontal wind velocity $U$ , number concentration of interstitial aerosol $N$ , energy dissipation rate $\varepsilon$ , net shortwave $SW$ and net longwave $LW$ radiation fluxes. . . . .	24
2.5	Schematic picture of a few aspects of cumulus dynamics and a horizontal cross section of mean parameters such as total water mixing ratio $q_t$ , liquid-water potential temperature $\Theta_l$ , vertical wind velocity $w$ and buoyancy $B$ within the environmental and cloudy region. . . .	27
3.1	General overview of the current version of ACTOS with its instrumentation. . . . .	30
3.2	A schematic picture of helicopter and ACTOS during a flight situation. The rotor downwash is deflected backwards by a true air speed of $15 - 20 \text{ m s}^{-1}$ . The figure is taken from Siebert et al. (2006a) . . .	31
3.3	Calibration of the hot wire data using the sonic data. The black dots denote the measured values and the red line marks the fitted curve. . .	37

- 
- 4.1 Measurement site: a) Location of Kiel in the north of Germany and b) detailed view of Kiel with the airport and the measurement site above the Baltic Sea. . . . . 40
- 4.2 Stratification of the atmospheric boundary layer and the lowest free troposphere above the Baltic Sea near Kiel in the north of Germany on October 8th, 2007. . . . . 41
- 4.3 Photograph of the stratocumulus layer above the Baltic Sea on 8th October, 2007. . . . . 42
- 4.4 Time series of six subsequent profiles at the top of a marine stratocumulus layer. The following data are shown: a) height ( $z$ ), b) liquid water content ( $LWC$ ), c) liquid water potential temperature ( $\Theta_l$ ) in black and absolute humidity ( $a$ ) in red, d) horizontal wind velocity ( $U$ ) in black and number concentration of interstitial aerosol ( $N$ ) in red. The mean true airspeed of ACTOS was  $14 \text{ m s}^{-1}$ . The grey boxes mark the respective turbulent inversion layer (TIL) of each profile. . . 43
- 4.5 Vertical profiles of: a) liquid water content ( $LWC$ ), b) liquid water potential temperature ( $\Theta_l$ ), c) absolute humidity ( $a$ ) in black and horizontal wind velocity ( $U$ ) in red, d) number concentration of interstitial aerosol ( $N$ ), e) gradient Richardson number ( $Ri$ ), with  $Ri = 1$  marked with the vertical black line, f) local energy dissipation rate ( $\varepsilon_\tau$ ) and g) local isotropy ( $\sigma_w^2/\sigma_u^2$ ), with  $\sigma_w^2/\sigma_u^2 = 4/3$  marked with the vertical dotted line. The horizontal blue lines denote the turbulent inversion layer (TIL), as defined by the level at which  $Ri = 1$ . For this example the inversion layer extends somewhat higher than the interfacial layer. The profile corresponds to transit IV in Fig. 4.4. . . 44
- 4.6 Mean profiles averaged over six individual soundings. Before averaging, the height was normalised with  $z_{norm} = 0$  denotes the height of cloud top and  $z_{norm} = 1$  marks the height of disappearance of the horizontal wind shear. The black lines represent the averaged values and the dotted lines mark the minimum and maximum values for the six profiles. Displayed are: a) liquid water content ( $LWC$ ), b) liquid water potential temperature ( $\Theta_l$ ), c) absolute humidity ( $a$ ), d) number concentration of interstitial aerosol ( $N$ ), e) horizontal wind velocity ( $U$ ), f) gradient Richardson number ( $Ri$ ), g) local energy dissipation rate ( $\bar{\varepsilon}_\tau$ ) and h) local isotropy, with  $\sigma_w^2/\sigma_u^2 = 4/3$  marked with the vertical dotted line. . . . . 46

- 
- 4.7 Impact of thickness ( $\Delta z_{sub}$ ) of the turbulent inversion layer on its turbulent properties. Dependencies are calculated for: a) horizontal wind shear ( $\frac{dU}{dz}$ ), b) atmospheric stability ( $\frac{d\Theta}{dz}$ ), c) gradient Richardson number ( $Ri$ ), d) averaged local energy dissipation rate ( $\bar{\varepsilon}_\tau$ ) and e) entrainment velocity ( $w_e$ ). . . . . 48
- 4.8 Schematic illustration of the development of the cloud top due to entrainment. a) Initial situation: between cloud layer (characterised by  $U_{cloud}$  and  $\Theta_{l,cloud}$ ) and free troposphere (characterised by  $U_{top}$  and  $\Theta_{l,top}$ ) an infinite inversion is located at *Sc top*. b) Entrainment processes lead to the generation of a turbulent inversion layer within the inversion layer with a maximal thickness of  $\Delta z_{max}$ , which is determined by  $\Delta\Theta_l$ ,  $\Delta U$ , and the gradient Richardson number (see text for more details). . . . . 49
- 4.9 Different terms of the turbulent kinetic energy balance equation. P is the production due to shear, B is the buoyancy term, and  $\varepsilon$  are observed energy dissipation rates as a function of TIL thickness  $\Delta z_{sub}$ . The values  $K_m$ ,  $\Delta U$ ,  $\Delta\Theta$ , and mean  $\Theta$  are taken from observations and Prandtl number  $Pr \approx 1$  is assumed. . . . . 50
- 5.1 The figure shows the location of Barbados. Picture is taken from Google Earth. . . . . 56
- 5.2 Mean meteorological parameters of the marine sub-cloud layer shown for all flights performed during both campaigns. The vertical lines denote the 25th percentile of the data. . . . . 57
- 5.3 Profiles of potential temperature ( $\Theta$ ), absolute humidity ( $a$ ), horizontal wind speed ( $U$ ) and wind direction ( $dd$ ) obtained during the ascent of ACTOS performed on November 20, 2010 starting at 1650 UTC. . . . . 58
- 5.4 Example of the shallow trade wind cumuli over Barbados. Picture is taken during a research flight along the east coast of Barbados on November 21, 2010. . . . . 59

- 5.5 A single cloud penetration: a)  $LWC$ , b) temperature ( $T$ ) and absolute humidity ( $a$ ) (whereby the red line denotes measurements with the infrared-absorption hygrometer LiCor and the broken red line marks measurements performed with the dew point hygrometer), c) vertical wind velocity ( $w$ ), d) buoyancy ( $B$ ), e) energy dissipation rate ( $\bar{\epsilon}_\tau$ ) where the black line denotes the direct method and the crosses mark the absolute values calculated based on  $S^{(2)}(t')$  and f) liquid-water potential temperature ( $\Theta_l$ ) and mixing fraction ( $\chi$ ). The white region between the two grey regions marks the cloud core and the two grey regions denote the edges of the cloud. The vertical black dashed line divides the cloud edge into part I, the subsiding shell and part II, the secondary shell. . . . . 61
- 5.6 The variability of all 217 selected clouds is represented by the probability density functions (PDFs) of the 90th percentile of: a) normalised liquid water content ( $LWC_{norm,90\%}$ ), b) buoyancy ( $B_{90\%}$ ), and c) vertical wind velocity ( $w_{90\%}$ ) inside the cloud core region. . . . . 63
- 5.7 Examples of cloud edges for each of the three stages of evolution of the trade wind cumuli: a) actively growing cloud with  $w_{90\%} > 0$  and  $B_{90\%} > 0$ , b) decelerated cloud with  $w_{90\%} > 0$  and  $B_{90\%} < 0$ , and c) dissolving cloud with  $w_{90\%} < 0$  and  $B_{90\%} < 0$ . In all plots, the color code is the same: blue regions mark the liquid water content ( $LWC$ ), black lines denote the vertical wind velocity ( $w$ ), green and red lines mark the energy dissipation rate ( $\bar{\epsilon}_\tau$ ) and the buoyancy ( $B$ ), respectively. The entrance of the cloud core region ( $CE$ ) is denoted by  $x = 0$  m, indicated by  $LWC > 0.2 \text{ g m}^{-3}$ . . . . . 65
- 5.8 Probability density functions of: a) minimum downdraft velocity ( $w_{10\%}$ ), b) minimum buoyancy inside the subsiding shell ( $B_{10\%}$ ), and c) the thickness of the subsiding shell ( $\delta$ ). . . . . 66
- 5.9 Comparison of the measured ( $\delta$ ,  $w_{10\%}$ ,  $B_{10\%}$ ) and simulated ( $\delta_m$ ,  $w_m$ ,  $B_m$ ) properties of the subsiding shell: a) thickness of the subsiding shell is plotted versus the downdraft velocity in the subsiding shell and b) buoyancy is plotted versus the downdraft velocity in the subsiding shell. The red lines represent the model values and the measurements are shown by the boxes. . . . . 70



- 
- 5.10 Schematic picture of the evolution of a cumulus cloud from actively growing to dissolving, where the growth of the subsiding shell at the expense of the cloud core region is illustrated. Here,  $\delta$  marks the distance from beginning of the subsiding shell to the entrance of the cloud core region, the thickness of the cloud core region is marked with  $cd$  and  $sb$  marks the thickness of the whole system. . . . . 71



# List of Tables

3.1	Summary of the instruments included in the following analysis. . . . .	32
5.1	The table summarises median properties of all selected clouds for each stage of evolution. These properties are: 90th percentile of $w$ inside the cloud core region ( $w_{90\%}$ ), 10th percentile of the downdraft velocity ( $w_{10\%}$ ) and the buoyancy ( $B_{10\%}$ ) inside the subsiding shell, distance between the boundary of the subsiding shell close to the cloud core region $X _{w_0}$ and $CE$ ( $\Delta(X _{w_0} - CE)$ ), the thickness of the subsiding shell ( $\delta$ ), cloud diameter ( $cd$ ), distance between the cloud-free boundary of the subsiding shell ( $X _{B_0}$ ) and the middle of the cloud core region ( $CM$ ) ( $\Delta(CM - X _{B_0})$ ), the relative frequency of the secondary shell ( $f$ ), median thickness of the secondary shell ( $\delta_d$ ), and median downdraft velocity ( $w_d$ ) inside the secondary shell. . . . .	67



# Bibliography

## References from peer-reviewed articles and books

- Abma, D., Heus, T., and Mellado, J. P. (2013). Direct numerical simulation of evaporative cooling at the lateral boundary of shallow cumulus clouds. *J. Atmos. Sci.*, 70(7):2088–2102.
- Batchelor, G. K. (1953). *The Theory of Homogeneous Turbulence*. Cambridge Science Classics. Cambridge University Press.
- Bennetts, D. A., McCallum, E., Nicholls, S., and Grant, J. R. (1986). Stratocumulus: an introductory account. *Meteorological Magazine*, 115(1364):50.
- Betts, A. (1973). Non-precipitating cumulus convection and its parameterization. *Q. J. R. Meteorol. Soc.*, 99(419):178–196.
- Biltoft, C. A. (2001). Some thoughts on local isotropy and the 4/3 lateral to longitudinal velocity spectrum ratio. *Boundary-Layer Meteorol.*, 100(3):393–404.
- Brucker, K. A. and Sarkar, S. (2007). Evolution of an initially turbulent stratified shear layer. *Physics of Fluids*, 19:105105.
- Chuang, P. Y., Saw, E. W., Small, J. D., Shaw, R. A., Sipperley, C. M., Payne, G. A., and Bachalo, W. D. (2008). Airborne phase doppler interferometry for cloud microphysical measurements. *Aerosol Sci. and Technol.*, 42(8):685–703.
- Davidson, P. A. (2004). *Turbulence : An Introduction for Scientists and Engineers*. OUP Oxford.
- de Roode, S. R. and Wang, Q. (2007). Do stratocumulus clouds detrain? FIRE I data revisited. *Boundary-Layer Meteorol.*, 122(2):479–491.

- Deardorff, J. W. (1980). Cloud top entrainment instability. *J. Atmos. Sci.*, 37:131–147.
- Driedonks, A. G. M. and Duynkerke, P. G. (1989). Current problems in the stratocumulus-topped atmospheric boundary layer. *Boundary-Layer Meteorol.*, 46(3):275–303.
- Edson, J. B., Hinton, A. A., Prada, K. E., Hare, J. E., and Fairall, C. W. (1998). Direct covariance flux estimates from mobile platforms at sea. *J. Atmos. Oceanic Technol.*, 15:547–562.
- Etling, D. (2008). *Theoretische Meteorologie – Eine Einführung*. Springer.
- Faloona, I., Lenschow, D. H., Campos, T., Stevens, B., van Zanten, M., Blomquist, B., Thornton, D., Brandy, A., and Gerber, H. (2005). Observations of entrainment in Eastern Pacific marine stratocumulus using three conserved scalars. *J. Atmos. Sci.*, 62:3268 – 3285.
- Feistel, R., Nausch, G., and Wasmund, N. (2008). *State and Evolution of the Baltic Sea, 1952–2005: A Detailed 50-year Survey of Meteorology and Climate, Physics, Chemistry, Biology, and Marine Environment*. Wiley-Interscience.
- Frisch, U. and Kolmogorov, A. A. N. (1995). *Turbulence: The Legacy of A. N. Kolmogorov*. Cambridge University Press.
- Garratt, J. R. (1994). *The Atmospheric Boundary Layer*. Cambridge Atmospheric and Space Science Series. Cambridge University Press.
- Gerber, H., Arends, B. G., and Ackerman, A. S. (1994). New microphysics sensor for aircraft use. *Atmos. Res.*, 31:235–252.
- Gerber, H., Frick, G., Malinowski, S. P., Brenguier, J. L., and Burnet, F. (2005). Holes and entrainment in stratocumulus. *J. Atmos. Sci.*, 62(2):443–459.
- Gerber, H. E., Frick, G. M., Jensen, J. B., and Hudson, J. G. (2008a). Entrainment, mixing and microphysics in trade-wind cumulus. *J. Meteorol. Soc. Japan*, 86A:89 – 106.
- Gerber, H. E., Frick, G. M., Jensen, J. B., and Hudson, J. G. (2008b). Entrainment, mixing, and microphysics in trade-wind cumulus. *J. Meteorol. Soc. Japan*, 86(0):87–106.

- 
- Haman, K. E., Makulski, A., Malinowski, S. P., and Busen, R. (1997). A new ultrafast thermometer for airborne measurements in clouds. *J. Atmos. Oceanic Technol.*, 14(2):217–227.
- Haman, K. E., Malinowski, S. P., Kurowski, M. J., Gerber, H., and Brenguier, J. L. (2007). Small scale mixing processes at the top of a marine stratocumulus – a case study. *Q. J. R. Meteorol. Soc.*, 133(622):213–226.
- Hanna, S. R. (1968). A method of estimating vertical eddy transport in the planetary boundary layer using characteristics of the vertical velocity spectrum. *J. Atmos. Sci.*, 25:1026–1033.
- Heintzenberg, J. and Charlson, R. J. (2009). *Clouds in the Perturbed Climate System: Their Relationship to Energy Balance, Atmospheric Dynamics, and Precipitation*. Strüngmann Forum reports. MIT Press.
- Heus, T. and Jonker, H. J. J. (2008). Subsiding shells around shallow cumulus clouds. *J. Atmos. Sci.*, 65:1003–1018.
- Heus, T., Pols, J., Freek, C., Jonker, J., Harm, J., den Akker, A. V., Harry, E., and Lenschow, D. H. (2009). Observational validation of the compensating mass flux through the shell around cumulus clouds. *Q. J. R. Meteorol. Soc.*, 135(638):101–112.
- Holle, R. L. and MacKay, S. A. (1975). Tropical cloudiness from all-sky cameras on Barbados and adjacent atlantic ocean. *J. Appl. Meteor.*, 14:1437–1450.
- Howard, L. (1803). I. On the modifications of clouds, and on the principles of their production, suspension, and destruction; being the substance of an essay read before the Askesian Society in the session 1802–3. *The Philosophical Magazine: Comprehending the Various Branches of Science, the Liberal and Fine Arts, Agriculture, Manufactures, and Commerce*, 17(65):5–11.
- Jonas, P. R. (1990). Observations of cumulus cloud entrainment. *Atmos. Res.*, 25(1):105–127.
- Jonker, H. J. J., Heus, T., and Sullivan, P. P. (2008). A refined view of vertical mass transport by cumulus convection. *Geophys. Res. Lett.*, 35:L07810.
- Katzwinkel, J., Siebert, H., and Shaw, R. A. (2012). Observation of a self-limiting,

- shear-induced turbulent inversion layer above marine stratocumulus. *Boundary-Layer Meteorol.*, 145:131–143.
- Katzwinkel, J., Heus, T., Shaw, R. A., and Siebert, S. (2013). Measurements of turbulent mixing and subsiding shells in trade wind cumuli. *J. Atmos. Sci.*, in review.
- Knight, C. A. and Miller, L. J. (1998). Early radar echoes from small, warm cumulus: Bragg and hydrometeor scattering. *J. Atmos. Sci.*, 55(18):2974–2992.
- Kolmogorov, A. N. (1941). The local structure of turbulence in incompressible viscous fluid for very large Reynolds numbers. *Doklady ANSSSR*, 30:301–304.
- Kondo, J., Kanechika, O., and Yasuda, N. (1978). Heat and Momentum Transfers under Strong Stability in the Atmospheric Surface Layer. *J. Atmos. Sci.*, 35:1012–1021.
- Koren, I., Oreopoulos, L., Feingold, G., Remer, L. A., and Altaratz, O. (2008). How small is a small cloud? *Atmos. Chem. Phys.*, 8(14):3855–3864.
- Kurowski, M. J., Malinowski, S. P., and Grabowski, W. W. (2009). A numerical investigation of entrainment and transport within a stratocumulus-topped boundary layer. *Q. J. R. Meteorol. Soc.*, 135(638):77–92.
- Langmuir, I. (1948). The production of rain by a chain reaction in cumulus clouds at temperature above freezing. *J. Meteorol.*, 5:175 – 192.
- Lawrence, M. G. (2005). The relationship between relative humidity and the dew-point temperature in moist air: A simple conversion and applications. *Bull. Am. Meteorol. Soc.*, 86(2):225–233.
- Lehmann, K., Siebert, H., and Shaw, R. A. (2009). Homogeneous and Inhomogeneous Mixing in Cumulus Clouds: Dependence on Local Turbulence Structure. *J. Atmos. Sci.*, 66(12):3641–3659.
- Lenschow, D. H., Paluch, I. R., Bandy, A. R., Pearson Jr, R., Kawa, S. R., Weaver, C. J., Huebert, B. J., Kay, J. G., Thornton, D. C., Driedger III, A. R. (1988). Dynamics and Chemistry of Marine Stratocumulus (DYCOMS) Experiment. *Bull. Am. Meteorol. Soc.*, 69:1058–1067.
- Lenschow, D. H., Zhou, M., Zeng, X., Chen, L., and Xu, X. (2000). Measurements of



- 
- fine-scale structure at the top of marine stratocumulus. *Boundary-Layer Meteorol.*, 97(2):331–357.
- Mauritsen, T., Svensson, G., Zilitinkevich, S. S., Esau, I., Enger, L., and Grisogono, B. (2007). A total turbulent energy closure model for neutrally and stably stratified atmospheric boundary layers. *J. Atmos. Sci.*, 64:4113–4126.
- Mellado, J. P. (2010). The evaporatively driven cloud-top mixing layer. *J. Fluid Mech.*, 660:5–36.
- Moeng, C. H., Stevens, B., and Sullivan, P. P. (2005). Where is the Interface of the Stratocumulus-Topped PBL? *J. Atmos. Sci.*, 62(7):2626–2631.
- Oncley, S. P., Friehe, C. A., Larue, J. C., Businger, J. A., Itsweire, E. C., and Chang, S. S. (1996). Surface-layer fluxes, profiles, and turbulence measurements over uniform terrain under near-neutral conditions. *J. Atmos. Sci.*, 53(7):1029–1044.
- Peltier, W. R. and Caulfield, C. P. (2003). Mixing efficiency in stratified shear flows. *Annu. Rev. Fluid Mech.*, 35(1):135–167.
- Pope, S. B. (2000). *Turbulent Flows*. Cambridge University Press.
- Rheinheimer, G. and Nehring, D. (1996). *Meereskunde der Ostsee*. Springer.
- Reynolds, O. (1883). An experimental investigation of the circumstances which determine whether the motion of water shall be direct or sinuous, and of the law of resistance in parallel channels. *Proceedings of the Royal Society of London*, 35(224–226):84–99.
- Rodts, S. M. A., Dnyrkerke, P. G., and Jonker, H. J. J. (2003). Size distributions and dynamical properties of shallow cumulus clouds from aircraft observations and satellite data. *J. Atmos. Sci.*, 60:1895 – 1912.
- Rogers, D. P. and Telford, J. W. (1986). Metastable stratus tops. *Q. J. R. Meteorol. Soc.*, 112(472):481–500.
- Siebert, H. and Muschinski, A. (2001). Relevance of a tuning-fork effect for temperature measurements with the Gill Solent HS ultrasonic anemometer-thermometer. *J. Atmos. Oceanic Technol.*, 18:1367–1376.

- Siebert, H., Wendisch, M., Conrath, T., Teichmann, U., and Heintzenberg, J. (2003). A new tethered balloon-borne payload for fine-scale observations in the cloudy boundary layer. *Boundary-Layer Meteorol.*, 106(3):461–482.
- Siebert, H., Franke, H., Lehmann, K., Maser, R., Saw, E. W., Schell, D., Shaw, R. A., and Wendisch, M. (2006a). Probing fine-scale dynamics and microphysics of clouds with helicopter-borne measurements. *Bull. Am. Meteorol. Soc.*, 87:1727 – 1738.
- Siebert, H., Lehmann, K., and Wendisch, M. (2006b). Observations of small scale turbulence and energy dissipation rates in the cloudy boundary layer. *J. Atmos. Sci.*, 63:1451 – 1466.
- Siebert, H., Lehmann, K., and Shaw, R. A. (2007). On the use of hot-wire anemometers for turbulence measurements in clouds. *J. Atmos. Oceanic Technol.*, 24(6):980–993.
- Siebert, H., Shaw, R. A., and Warhaft, Z. (2010). Statistics of small-scale velocity fluctuations and internal intermittency in marine stratocumulus clouds. *J. Atmos. Sci.*, 67:262 – 273.
- Siebert, H., Beals, M., Bethke, J., Bierwirth, E., Conrath, T., Dieckmann, K., Ditas, F., Ehrlich, A., Farrell, D., Hartmann, S., Izaguirre, M. A., Katzwinkel, J., Nuijens, L., Roberts, G., Schäfer, M., Shaw, R. A., Schmeissner, T., Serikov, I., Stevens, B., Stratmann, F., Wehner, B., Wendisch, M., Werner, F., and Wex, H. (2013). The fine-scale structure of the trade wind cumuli over Barbados - an introduction to the CARRIBA project. *Atmos. Chem. Phys.*, 13(19):10061–10077.
- Siebesma, A. P., Bretherton, C. S., Brown, A., Chlond, A., Cuxart, J., Duynkerke, P. G., Jiang, H., Khairoutdinov, M., Lewellen, D., Moeng, C.-H., Sanchez, E., Stevens, B., Stevens, D. E. (2003). A large eddy simulation intercomparison study of shallow cumulus convection. *J. Atmos. Sci.*, 60:1201 – 1219.
- Slingo, A. (1990). Sensitivity of the earth’s radiation budget to changes in low clouds. *Nature*, 343(6253):49–51.
- Small, J. D., Chuang, P. Y., Feingold, G., and Jiang, H. (2009). Can aerosol decrease cloud lifetime? *Geophys. Res. Lett.*, 36:L16806.
- Smyth, W. D. and Moum, J. N. (2000). Length scales of turbulence in stably

- 
- stratified mixing layers. *Physics of Fluids*, 12:1327–1342.
- Solomon, S., Qin, D., Manning, M., Chen, Z., Marquis, M., Averyt, K. B., Tignor, M., and Miller, H. L. (2007). *Contribution of Working Group I to the Fourth Assessment Report of the Intergovernmental Panel on Climate Change*. Cambridge University Press
- Squires, P. and Warner, J. (1957). Some measurement in the orographic cloud of the island of Hawaii and of trade wind cumuli. *Tellus*, 9:475–494.
- Stevens, B. (2002). Entrainment in stratocumulus-topped mixed layers. *Q. J. R. Meteorol. Soc.*, 128(586):2663–2690.
- Stevens, B., Lenschow, D. H., Vali, G., Gerber, H., Bandy, A., Blomquist, B., Brenguier, J., Bretherton, C., Burnet, F., Campos, T., et al. (2003). Dynamics and chemistry of marine stratocumulus-DYCOMS-II. *Bull. Am. Meteorol. Soc.*, 84(5):579–594.
- Stith, J. L. (1992). Observations of cloud-top entrainment in cumuli. *J. Atmos. Sci.*, 49:1334–1347.
- Stommel, H. (1947). Entrainment of air into a cumulus cloud. *J. Meteorol.*, 4:91–94.
- Sullivan, P. P. et al. (1998). Structure of the entrainment zone capping the convective atmospheric boundary layer. *J. Atmos. Sci.*, 55:3042–3064.
- Tennekes, H. and Lumley, J. L. (1972). *A First course in turbulence*. MIT Press.
- Wang, S., Golaz, J. C., and Wang, Q. (2008). Effect of intense wind shear across the inversion on stratocumulus clouds. *Geophys. Res. Lett.*, 35:L15814.
- Wang, S., Zheng, X., and Jiang, Q. (2012). Strongly sheared stratocumulus convection: an observationally based large-eddy simulation study. *Atmos. Chem. Phys.*, 12(11):5223–5235.
- Wang, Y., Geerts, B., and French, J. (2009). Dynamics of the cumulus cloud margin: An observational study. *J. Atmos. Sci.*, 66(12):3660–3677.
- Wang, Y. and Geerts, B. (2010). Humidity variations across the edge of trade wind cumuli: Observations and dynamical implications. *Atmos. Res.*, 97(1):144–156.

- Wendisch, M. and Brenguier, J. L. (2013). *Airborne Measurements for Environmental Research: Methods and Instruments*. Wiley Series in Atmospheric Physics and Remote Sensing. Wiley.
- Wood, R. (2012). Stratocumulus clouds. *Mon. Wea. Rev.*, 140(8):2373–2423.
- Woodward, B. (1959). The motion in and around isolated thermals. *Q. J. R. Meteorol. Soc.*, 85(364):144–151.
- World Meteorological Organization (1975). *International cloud atlas*. Secretariat of the World Meteorological Organization.
- Wyngaard, J. C. (2010). *Turbulence in the Atmosphere*. Cambridge University Press.
- Zhao, M. and Austin, P. H. (2005a). Life cycle of numerically simulated shallow cumulus clouds. Part I: Transport. *J. Atmos. Sci.*, 62(5):1269–1290.
- Zhao, M. and Austin, P. H. (2005b). Life cycle of numerically simulated shallow cumulus clouds. Part II: Mixing dynamics. *J. Atmos. Sci.*, 62(5):1291–1310.
- Zuber, A. and Witt, G. (1987). Optical hygrometer using differential absorption of hydrogen Lyman- $\alpha$  radiation. *Applied Optics*, 26:3083–3089.

## Manuals

- Dantec Dynamics A/S (2012). *Probes for Hot-wire Anemometry*. Dantec Dynamics A/S, Skovlunde, Denmark.
- GILL Instruments (2004). *Horizontally Symmetrical Research Ultrasonic Anemometer*. GILL Instruments, Lymington, UK.
- LI-COR, Inc. (2009). *LICOR 7500A, Open Path CO<sub>2</sub>/H<sub>2</sub>O Gas Analyzer*. LI-COR, Inc., Lincoln, Nebraska, USA.
- Meteolabor AG (2010). *Dew point hygrometer TP3-S*. Meteolabor AG, Wetzikon, Switzerland.
- TSI Inc. (2000). *Model 3760A/3762 Condensation Particle Counter – Instruction Manual*. TSI Inc., St. Paul, MN, USA.

Vaisala (1999). *PTB220 Series Digital Barometers, User's Guide*. P.O. Box 26,  
FIN-00421 Helsinki, Finland.



# Acknowledgements

I would like to thank all people who encouraged and supported me during the time doing my PhD:

- First of all, my thanks go to Holger Siebert as my supervisor. Thanks to him for his advices and critical and constructive debates.
- I would like to thank Prof. Andreas Macke for the opportunity to do my PhD at the Leibniz Institute for Tropospheric Research.
- I gratefully acknowledge Deutsche Forschungsgemeinschaft (DFG) for funding this work within the priority program Metström (SI 1534/2-2) and the DFG-project (SI 1534/3-1).
- I thank the two pilots Alwin Vollmer and Milos Kapetanovic for the great helicopter flights during the CARRIBA campaign. Furthermore, I thank the whole CARRIBA crew for a great time on Barbados. At last but not least my thanks go to Enviscope for technical support during the measurement campaign.
- I acknowledge Raymond Shaw and Thijs Heus for their contribution to our work. It was a pleasure to work with them.
- I thank my colleges, especially Tina Schmeißner for intensive discussion and funny moments inside and outside of office.
- I thank Dr. Rainer Tiesel for his useful informations concerning the Baltic Sea weather conditions and especially the cloudiness in this region.
- Special thanks go to Florian Ditas for enlightening discussion, his advices and for his love and patience.
- Many thanks go to my family and friends. They encouraged me all the time.